UNIVERSITY OF OKLAHOMA

GRADUATE COLLEGE

Dioxygen Evolution from Oxo-Ruthenium Complexes

A THESIS

SUBMITTED TO THE GRADUATE FACULTY

in partial fulfillment of the requirements for the

Degree of

Master of Science

By

Matthew T. Swann

Norman, Oklahoma

2020

Dioxygen Evolution from Oxo-Ruthenium Complexes

A THESIS APRROVED FOR
THE DEPARTMENT OF CHEMISTRY
AND BIOCHEMISTRY

BY THE COMMITTEE CONSISTING OF

Dr. George Richter-Addo, Chair
Dr. Kenneth Nicholas
Dr. Yihan Shao

ACKNOWLEDGEMENTS

I would like to thank Dr. Kenneth Nicholas for his support, insight, and patience over the course of my tenure in the Nicholas research group. Your guidance has helped develop me into the scientist I knew I could be. I would also like to extend thanks to Dr. Yihan Shao, who has provided crucial counseling and guidance on my computational work. Last, but not least, I would like to Dr. George Richter-Addo, for his support and knowledge, providing critical feedback that helped shape the direction of my research.

I would like to thank Theo Rusmore, Chandu Bandari, and the remaining members and alumni of the Nicholas group for their mentorship, knowledge, and friendship, without which the research lab would have been a cold environment. In addition, I would like to thank the members of the Inorganic Division, who fostered a critical environment by which I was able to further hone my abilities and satisfy my curiosity in chemistry.

I would like to thank the Department of Chemistry and Biochemistry at the University of Oklahoma for providing the opportunities and resources necessary for me to actively pursue my goals and research.

I would also like to thank the National Science Foundation, who partially funded this project.

TABLE OF CONTENTS

LIST OF TABLES

LIST OF FIGURES

ABSTRACT

Divestment from fossil fuels is necessary in order to lessen the impacts of climate change across the planet. One alternative to fossil fuels is hydrogen gas, which is utilized in syn gas and hydrogen fuel cells. However, the production of hydrogen gas is often extremely costly. One of the primary ways by which hydrogen gas is produced is by water splitting/water oxidation catalysts. Recent work on water oxidation catalysts have demonstrated Ru(V) oxo complexes to be high performance, eclipsing the activity of natural water oxidation systems, such as the oxygen-evolving complex that splits water in photosynthesis. Water oxidation occurs in two distinct steps, the hydrogen reduction reaction and the oxygen evolution reaction (OER). The OER is usually the rate limiting portion of the reaction for WOCs. One of the mechanisms by which the OER occurs, is the intermolecular bimolecular (I2M) mechanism.

The I2M mechanism does not require water to evolve oxygen, unlike other WOCs. Thus, the I2M mechanism can be applied to a wider array of catalytic reactions, such as oxygen-atom transfer reactions (OAT) and small molecule splitting (CO_2 splitting, N_2O splitting). Optimizing catalysts for the I2M mechanism then provides a general method for increasing catalytic efficiency. To this end, we have selected a series of ruthenium (V) oxo coordination compounds to evaluate their ability to undergo the OER by a slightly modified I2M mechanism. The coordination compounds selected contain the ligands: nitrilotriacetate (NTA), bipyridine dicarboxylate, porphyrin, dimethyl glyoxime, and α-hydroxyacid (AHA). The aim of this work is to computationally determine the gas phase ground-state thermodynamics and transition states involved in this reaction and to determine the effect charge, coordination number, and solvation have on reactivity. We have also sought to synthesize a few of these oxo-ruthenium complexes in order to experimentally evaluate their OER reactivity.

Computational analysis of the complexes showed exceedingly large free energies of O-O radical coupling for anionic complexes, suggesting that anionic complexes would not be OER catalysts. Comparing the activation barriers for radical coupling of our neutral complexes with those found in the literature suggests that neutral complexes may experience the lowest barrier, and thus make faster OER catalysts. Examining the coordination number of the ruthenium atoms in these complexes suggests that sterically crowded complexes feature extremely downhill total free energies, providing a large driving force so that the reaction proceeds in the forward direction. Complexes that yield low coordinate numbers upon O_2 evolution on the other hand feature large uphill total free energies. For favorable OER thermodynamics oxo complexes should have a coordination number of 6 or 7, otherwise large thermodynamic barriers may prohibit reactivity. Solvation of the NTA complexes by water showed that high polarity solvents may inhibit the O-O coupling step, but overall drive more favorable overall OER thermodynamics.

Experimentally, we synthesized the $(C_3H_7)_4N[(AHA)_2Ru^VO]$ complex to satisfactory purity. The AHA complex was then utilized in photolysis and thermolysis experiments, to determine the stability and reactivity of the species. These experiments seemed to indicate to that the complex undergoes decomposition under both conditions, indicating that this complex may not be able to catalyze the OER reaction under anything other than milquetoast conditions, if at all. A number of synthetic methods were employed to synthesize an NTARuO(L) complex, with varying results. While none of the methods produced an easily characterizable and isolable complex, they did highlight the need for acidic and oxidizing conditions in order to bind NTA to Ru, lest it be out competed by softer bases such as pyridine.

Understanding the ability of Ru(V) Oxo complexes to undergo the OER carries widespread implications on not just water splitting, but to a number of other chemical processes. The results herein lay out a number of important aspects that should be considered when designing OER catalysts.

I. Introduction

The existential threat of climate change is one that requires the expeditious development of new technologies to curb CO_2 emissions.[1–5] One potential solution to this is the utilization of H_2 gas rather than fossil fuels, thereby producing water instead of CO_2. Hydrogen gas can be produced via the splitting of water into hydrogen gas and oxygen gas. This process is very energetically demanding, requiring temperatures greater than 2200°C for the uncatalyzed reaction to proceed in any meaningful way.[6] The water splitting reaction itself can be split into its respective half reactions: the Oxygen Evolution Reaction (OER, oxidation) and the Hydrogen Reduction Reaction (HRR, reduction). At STP the unfavorable cell potential can be attributed to the OER, which is a multistep reaction that features the breaking of 4 O-H bonds and the formation of a single O-O bond. The energy required to break a single O-H bond is 117.6 kcal/mol.[7] The total free energy for this process is 517.2 kcal/mol (based on $E°_{cell}$). This does not account for the activation energies for each of the individual steps.

		E°(V)
OER:	$2H_2O \longrightarrow O_2 + 4H^+ + 4e^-$	-1.34
HRR:	$4H^+ + 4e^- \longrightarrow 2H_2$	0.00
Total:	$2H_2O \longrightarrow 2H_2 + O_2$	-1.34

Figure 1: Water Splitting half reactions.

In order to accommodate these large energetic demands, efficient catalysts are necessary to make water oxidation financially and commercially viable. In nature, water oxidation occurs in photosynthesis, via photosystem II (PSII). In particular, the active component of PSII is the oxygen-evolving complex (OEC), which contains a Mn_4O_5Ca cluster.[8] The Mn cluster is able to

convert two water molecules into two molecules of hydrogen gas and one molecule of oxygen gas every 1.6 ms. Taking into account the oxidative damage that occurs due to the formation of singlet oxygen, the OEC has a turnover number (TON) on the order 10^6, which is incredibly efficient.[9]

Attempts to replicate the efficiency of PSII have been made with both heterogeneous and homogeneous catalysts. In terms of heterogeneous catalysts, several studies have demonstrated the efficacy of various transition metal systems. Electrochemically, a number of abundant transition metals like Fe and Ni have been utilized to achieve fairly low overpotentials.[10] Noble metal systems such as RuO_2 and IrO_2, in addition to mixed systems like Co-Ir, have exhibited good performance overall.[11] However, these systems are prone to dissolution into the electrolyte solution due to relatively large overpotentials and have poor long-term stability.[11] Photochemical methods are promising, but still underdeveloped and have problems regarding photodegradation.[12] Not only that, but many of these complexes experience fairly slow OER at the anode, limiting the overall speed of these systems.[13,14] In heterogeneous catalysis, often structure-activity relationships are difficult to establish, and mechanisms are hard to prove. These same problems are present for water oxidation catalysts, providing little insight on how to rationally and systematically improve the deficiencies present.[15,16] In this regard, homogeneous catalysts offer a significant advantage in that the active sites are well-defined and more analytical techniques exist by which to analyze them.

The viability of homogeneous catalysis came into its own in 2012, with the report of a cerium (IV)-driven ruthenium bipyridine dicarboxylate catalyst $[BDA]Ru(Isq)_2$ by Duan, et al. that exhibited a turnover frequency (TOF) of 300 s^{-1} (TOF ranges from 100-400 s^{-1} for OEC).[17] Mechanistic studies have highlighted two distinct mechanisms for water oxidation by these

(BDA)RuL_2 complexes.[18] While both mechanisms feature the same HRR, each undergoes a unique process for OER. The first is the Water Nucleophilic Attack (WNA) mechanism. After the initial oxidation of water to a Ru(V) oxo species, water attacks the oxo, forming a Ru(IV) hydroperoxide. Subsequent oxidations convert the hydroperoxide group into a peroxide, which is eventually evolved as dioxygen gas, allowing another water ligand to bind and restart the cycle. The Intermolecular Bimolecular (I2M) mechanism relies on radical coupling of two Ru(V) oxo species to form a bimetallic bridged peroxide. Oxidation leads to the eventual evolution of dioxygen. Both systems have their deficiencies. WNA catalysts require the ruthenium (V) oxo to be sufficiently electron withdrawing so as to form an electrophilic oxo that can be attacked by water. This causes them to in general be slower than I2M catalysts, although this can be remedied by using increasingly basic conditions. I2M, as the name suggests, features a bimolecular coupling of two ruthenium (V) oxo units, making this step second order with respect to catalyst concentration. This means that increased catalyst loading can be used to achieve higher reaction rates. Alternatively, this can be remedied by utilizing bimetallic catalysts, where the two ruthenium (V) oxos are held in close proximity, though this can be synthetically challenging. The HRR portion of this reaction is not considered to be rate limiting, thus the bottleneck for these complexes is the OER.

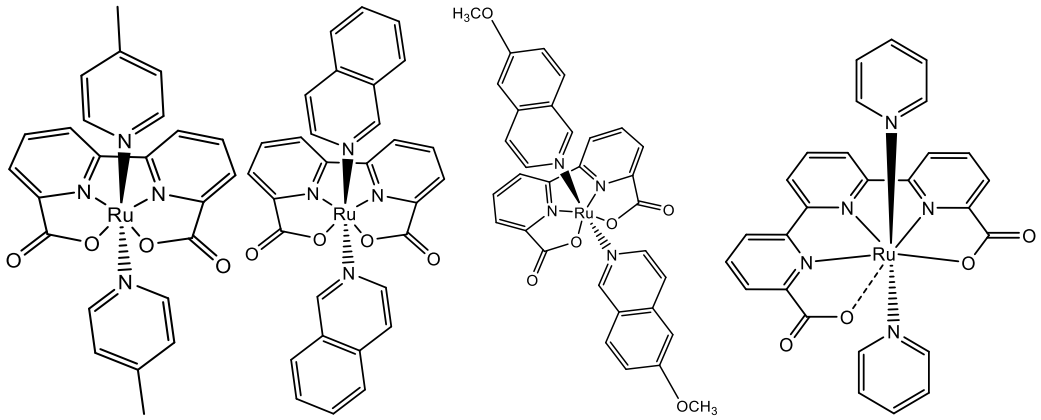

Figure 2: Water oxidation catalysts reported by Duan, et al.[17] *(far left and center left), Xie, et al.*[19] *(center right), and Matheu, et al.*[20] *(far right).*

Further work on complexes that follow the WNA mechanism culminated with the report of a complex by Matheu, et al. that yielded a maximum TOF of 50,000 s^{-1}, 125x faster than the maximum TOF for the OEC in vivo.[9,20] Optimizations of the I2M complexes involve replacing the isoquinoline axial ligands with 6-methoxy isoquinoline, achieving a TOF of 1274 s^{-1}, more than three times greater than the OEC.[9,19] In this regard, WNA complexes have left I2M behind with respect to water oxidation and oxygen evolution. However, I2M has the advantage that it does not necessarily require an aqueous solvent system. Once the Ru(V) oxo species has been generated, water is not needed to evolve oxygen. To this end, the lessons learned from I2M complexes can be applied to other important processes, such as oxygen atom transfer (OAT) reactions, or CO_2 and N_2O splitting. Thus, further optimizing and expanding the library of I2M catalysts has an important bearing on not only water oxidation but on many other different systems as well.

One of the key components that help drive the high TOFs for BDA complexes is the excess cerium ammonium nitrate (CAN), which is used as a potent oxidizing agent. The mechanism for Ce(IV)-driven water oxidation features the oxidation of the ruthenium (III) aqua

complex to a ruthenium (V) oxo and hydrogen evolution. This oxidation is considered rate-limiting in a number of older generation water catalysts, but is not in the BDA systems.[21] After the initial oxidation, two ruthenium (V) oxos then undergo O-O radical coupling to form a bimetallic ruthenium (IV,IV) bridged peroxide complex. This bridged peroxide is then oxidized, yielding a bimetallic ruthenium (V,IV) complex. Nucleophilic water and an additional oxidation liberate dioxygen and reform the catalyst. Experimentally, the oxidations required to evolve oxygen from the bridged peroxide are much faster than the O-O radical coupling step, thus this radical coupling step is often found to be the rate-limiting step in this process.[18]

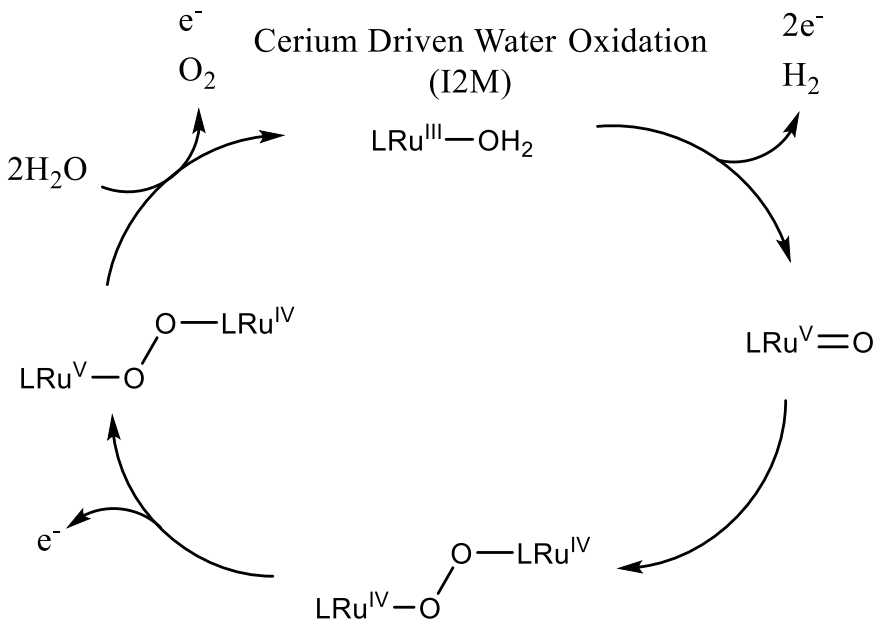

Figure 3: Mechanism for cerium driven water oxidation.[9]

Work done by Fan, et al. suggests that the barrier for radical coupling is due to distortion of the Ru(V) oxo complex and intermolecular interactions.[22] However, the activation barriers reported by Fan fail to correlate with the observed reaction rates, indicating that the methods employed may be insufficient to describe the interactions occurring. Additional work by Xie, et al. corroborate the importance of intermolecular interactions, in that stronger attractive forces

bring down the activation barrier.[19] The pi-stacking ability of axial isoquinolines provides a significant improvement over the smaller pyridine ligands. Electron-donating substituents on isoquinolines improve the TOF, due in part to the increased Van der Waals interactions between the axial ligands. This effect is not seen in the pyridine-ligated complexes due to the limited pi stacking interactions between the more compact pi systems of the pyridine ligands. It has also been demonstrated that increasing the charge of the complex through modification of the equatorial ligand increases coulombic repulsion, and thus raises the activation barrier for coupling as well.[23]

These factors can be used to increase the efficiency of the oxygen evolution reaction, and in turn the efficiency of water oxidation as a whole. However, the need for excess oxidizing agent limits the ability for these sorts of reactions to be scaled up and applied in industrial settings. To this end, it is valuable to explore the ability of Ru(V) oxo complexes to undergo the oxygen evolution reaction without external oxidations (other than those required to form the oxo in the first place). This alternative mechanism can be imagined proceeding through 4 unique steps. This begins with step (0): the oxidation and formation of the Ru(V) oxo by some external oxidant or substrate. Next, step (1): two Ru(V)-oxo complexes engage in radical coupling, forming the bridged peroxide (Ru(IV,IV)). This is followed by step (2): the dissociation of a reduced ruthenium (III) complex, forming the monometallic ruthenium (IV) dioxygen complex. This process closes with step (3): oxygen evolution from the dioxygen complex, forming an additional reduced ruthenium (III) complex.

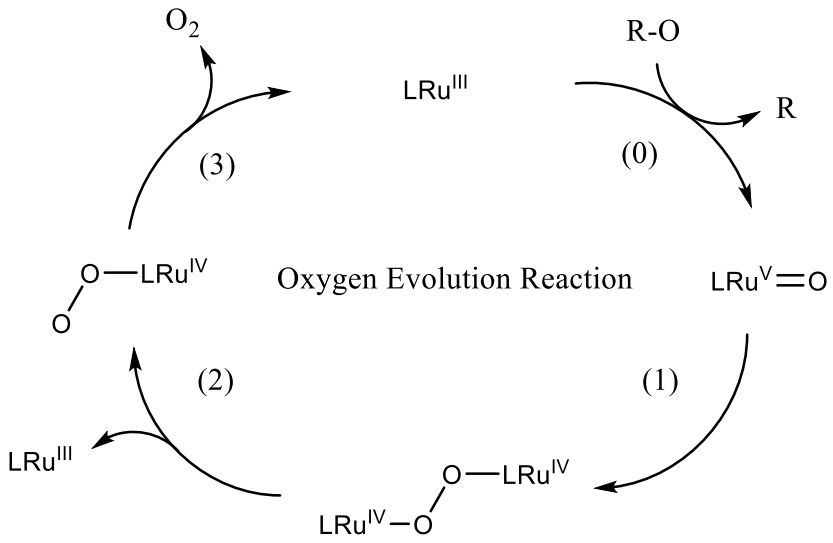

Figure 4: Oxygen evolution mechanism without cerium-driven oxidation.

Because cerium is not driving this reaction, it is entirely possible that reaction (0), the oxidation of the ruthenium (III) complex to the ruthenium (V) oxo, is rate-limiting. However, this depends on the identity of the oxidant/substrate utilized. To this end, we decline to speculate on the relative efficiency of this step as it is surely unique to the system considered. Reactions (1)-(3) only rely on the presence of the reactive Ru(V) intermediate, and in this scheme are considered to be independent of the substrate/oxidizing agent used. For this reason, we have chosen to focus on these three steps for this study. Disregarding reaction (0), reaction (1) is often considered to be the rate-limiting step for the oxygen evolution reaction. Thus, by optimizing the radical coupling step, the rate of oxygen evolution should increase. Understanding the reaction energetics for this step, along with steps (2) and (3), could provide valuable insight for designing ruthenium-based catalysts for a large array of oxygen-transfer chemical processes. Our goals for this body of work are two-fold. First, to computationally evaluate the ability of a number of Ru(V) oxo complexes to undergo the oxygen evolution reaction. Second, to synthesize and experimentally validate the ability of these complexes to perform these reactions.

Primer: Density Functional Theory[24]

The goal of computational chemistry is to completely describe the physical and chemical properties of molecular structures so that they may be applied to real systems. The electronic structure of a many-body system composed of atoms is described by the Schrödinger equation. The Schrödinger equation for such a system is split into five distinct terms. The first is the kinetic energy operator for each electron, followed by the electrostatic attraction between each electron and the nuclei in the system. The third term is the electrostatic repulsion between electrons. The final two terms are the kinetic energy operator for the nuclei, followed by the nuclear repulsion. By invoking the Born-Oppenheimer approximation, we can separate the many-body Schrödinger equation into an electronic contribution (left) and a nuclear contribution (right). This separation greatly simplifies the calculations required to describe molecular systems, without which solutions would be incredibly difficult, if not impossible.

$$\widehat{H} = \left[-\frac{\hbar^2}{2m_e} \sum_i \nabla_i^2 - \sum_i \sum_k \frac{e^2 Z_k}{r_{ik}} + \sum_{i<j} \frac{e^2}{r_{ij}} \right] + \left[-\frac{\hbar^2}{2M_k} \sum_k \nabla_k^2 + \sum_{k<l} \frac{e^2 Z_k Z_l}{r_{kl}} \right]$$

$$\widehat{H} = H_{elec.} + V_{Nuc.}$$

The purely electronic Hamiltonian has no closed form solution, due to the electrostatic repulsion between electrons. This can be remedied by utilizing Density Functional Theory, where the energy is optimized with respect to the electron density ρ(r), rather than the wave function. This, like the Schrödinger equation, is exact, no additional approximations are immediately necessary. The resulting one-electron Kohn-Sham equation (contains similar terms for the kinetic energy, electron-nuclear attraction, and electron repulsion. It also contains a new term, V_{xc}, which is the exchange-correlation interaction. While the other energetic contributions

from the first three terms are explicit, the exact form of the exchange-correlation functional is unknown. One of the primary goals of computational chemistry with respect to DFT is to establish increasingly accurate approximations for the exchange-correlation functional.

$$\hat{h} = -\frac{1}{2}\nabla_i^2 - \frac{Z_k}{r_{ik}} + \frac{1}{2}\int \frac{\rho(r')}{|r - r'|} dr' + V_{xc}$$

$$V_{xc} = \frac{\delta E_{xc}}{\delta \rho}$$

Originally, functionals were exclusively dependent on the electron density ρ via the local density approximation (LDA). This was eventually improved upon by the addition of dependence on the gradient, ∇ρ, a method known as the generalized gradient approximation (GGA). These functionals were further improved upon by the addition of Hartree-Fock exchange energy, creating so-called hybrid functionals. Hybrid functionals have shown remarkable performance on a wide array of systems and are in general the functionals of choice for chemists. However, there is no recipe for determining the 'correct' amount of HF exchange that should be included. Hybrid functionals can sometimes exhibit significant systematic error by including too much HF exchange (favoring high spin states), or too little (favoring low spin states). For this reason, care must be taken when applying hybrid functionals to systems that may have more than one spin state, such as transition metal compounds.

$$E_{xc} = (1 - a)E_{xc}^{DFT} + aE_x^{HF}$$

Electron spin treated in a few different ways. For closed shell systems that have no unpaired electrons, only a single set of orbitals is optimized for both spin up and spin down orbitals, effectively making two identical copies of the optimized orbitals. This approach is sufficient for closed-shell systems but cannot be used to describe open-shell systems. For open-

shell systems there are two solutions to this problem. The first is the restricted open shell method. The system is essentially treated as though it were a closed-shell system, with the orbital of the unpaired electron not being multiplied by a factor of two. This approach results in a solution that is an eigenstate of the S^2 operator. However, this method fails to account for any additional spin polarization that may come from the doubly occupied orbitals. This problem is remedied by utilizing an unrestricted method, where the spin-up and spin-down orbitals are optimized separately. This method accounts for spin polarization and gives a more complete picture of the spin density in the system in question. However, solutions for unrestricted DFT are generally not eigenstates of S^2, due to spin contamination from higher spin states. Such contamination, when it is present, can lead to incorrect energies for higher spin states. This is only a problem in cases where the expectation value $<S^2>$ deviates significantly from the assigned spin state of the system. Little to no difference between the expectation value and the assigned spin state indicates that there is little to no spin contamination.

II. Results and Discussion

Preview of Results

The oxygen evolution reaction can be envisioned to occur by a 3-step mechanism. The process begins with an initial coupling of two odd electron Ru(V) oxo complexes to form a bridged, bimetallic Ru(IV) peroxide. Once coupled, one of the ruthenium-oxygen bonds cleaves from the peroxo dimer to form a Ru(IV) dioxygen complex and a reduced Ru(III) species. The final step of the process is dioxygen evolution from the Ru-dioxygen complex to another reduced Ru(III) species and $^3O_2$.

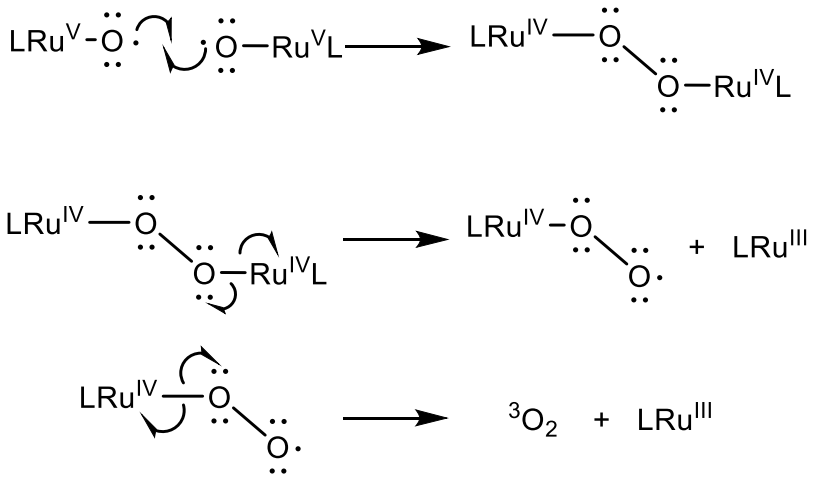

Figure 5: Proposed Oxygen-Evolution Mechanism.

Very few Ru(V)-oxo complexes have been isolated and completely characterized, suggesting that these species may be inherently unstable and reactive. For the few that have been characterized, the most important features to consider are their molecular structure and the magnetic moment, as they can be used to evaluate the validity and accuracy of computational models. The ground state spin multiplicity can be determined from the magnetic moment and should agree with the lowest energy spin state determined by DFT (density functional theory). A

good DFT model will yield a geometry that is very similar to the x-ray structure. In particular, the bond lengths associated with ruthenium's coordination environment are the most indicative of reactivity and the ones most liable for error. A survey of reported crystal structures for 3d, 4d, and 4f metal complexes demonstrates an experimental standard deviation of metal-ligand bond lengths of 0.01-0.02 Å, and a standard deviation of 1-2° for bond angles, although these can deviate by up to 3.6° for labile bonds such as metal phosphine bonds.[25] The study also states that dihedral angles have a significantly larger standard deviation of 47°, which Martín attributes to crystal packing effects.[25] A few studies have also evaluated the deviation of DFT-determined geometries from x-ray structures, in particular the coordination center bond distances. Work done by Jiménez-Hoyos, et al. on a set of 4d metal complexes (including RuO_4, $Ru(CO)_5$, and $RuCp_2$) show an average maximum deviation of 0.0185 Å with B3LYP.[26] Additional work done by Minenkov, et al. on 18 ruthenium olefin metathesis catalysts shows a maximum deviation of 0.044 Å in the coordination center bond distances for B3LYP.[27] This demonstrates that DFT methods (B3LYP in particular) can be used to approach and even surpass the precision of standard crystallographic techniques. However, Minenkov's work, which surveys a larger variety of ruthenium coordination complexes, shows that they may deviate by more than double the standard deviation. We should consider bond lengths that approach 0.02 Å to show excellent agreement, while bond lengths within 0.044 Å to be less good, but still acceptable.

Some of the complexes for this study were chosen in part based on their appearance in the literature, so as to correlate theory and experiment where possible. Crystallographic data and magnetic moment data on oxo-Ru(V) complexes are still sparse. It was also important to have a variety in charge, geometry, coordination number, etc. to establish how these

structural/electronic variables could affect the energetics of the Ru=O coupling/O_2 evolution process.

A total of 5 different ligand types were selected, with some of these complexes having additional ligand variation. The tetradentate bipyridine dicarboxylate ligand (BDA, complexes **1a** and **1b**) was selected from the initial report by Duan, et al.[17] From this backbone, we've selected the putative hepta-coordinate Ru-oxo species, as well as an octahedral variation of this complex with the oxo group replacing one of the axial pyridine ligands. The isoquinoline ligated complex was not chosen to eliminate the effect of pi-stacking, so as to isolate the effect of the backbone. Nitrilotriacetate (NTA, complexes **2a**, **2b**, and **2Cl**) is a common trianionic tetradentate chelating agent. It was chosen in part due to its ability to neutralize the Ru^{III} ion and Ru^{V}=O positive ions to form a neutral complex. The NTA ruthenium oxo complex could have a variety of configurations: trigonal bipyramidal or octahedral, neutral or anionic. Complex **3** (α-hydroxy acid, AHA) is one of the few examples of a reported stable, isolable Ru(V)-oxo complex reported in the literature.[28,29] This compound exhibits a trigonal bipyramidal geometry and experimental data by which to verify our computational results. The porphyrin ligand produces a neutral ruthenium (V) oxo complex **4** and is a common motif in bioinorganic chemistry. The dimethylglyyoximate complex (DMG, complex **5**) has also been reported and characterized spectroscopically, but an x-ray structure of it has not been.[30] Both complexes **4** and **5** are octahedral, neutral (uncharged), and contain the oxo-group in the axial position.

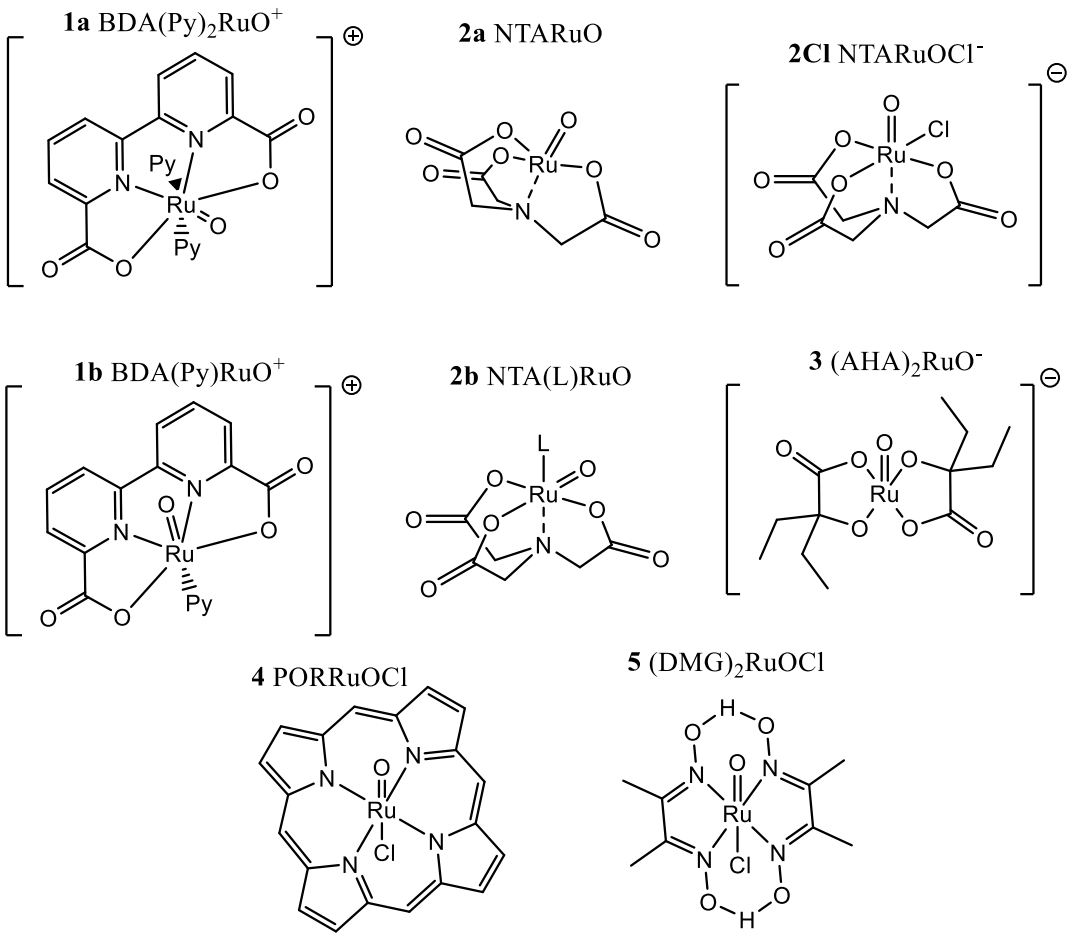

Figure 6: Selected ruthenium(V)-oxo complexes.

a. Computational Analysis

To evaluate the structural and electronic effects on the OER, ground state geometries for the $LRu^{V}O$, $(LRu^{IV}O)_2$, $LRu^{V}O_2$ and LRu^{III} intermediates were initially optimized by DFT, utilizing B3LYP[31–33] or OPBE[34–37]. The basis sets used for this were 6-31G(d)[38–42] for H, C, N, and O, 6-311++G(d,p)[43,44] for Cl, and LANL2DZ[45–47] for Ru. From the B3LYP optimized geometries, single point M06[48] calculations were performed utilizing 6-311++G(d,p) for H, C, N, O and Cl, and SDD (Stuttgart-Dresden)[49] for Ru. The SDD effective core potential (ECP) was used for Ru. These were all done in the gas-phase, without a solvent model. The Conductor-like

Polarizable Continuum Model (CPCM)[50] solvent model was used with water to determine the effect of a polar solvent on the **2b** complexes. All calculations done on complexes **1b**, **4**, and **5**, including the B3LYP and OPBE optimizations and M06 single point calculations were done by Dr. Kenneth Nicholas. All calculations done on complexes **1a**, **2b**, **2Cl**, and **3**, including B3LYP and OPBE optimizations, and M06 single point calculations were carried out by Matthew Swann.

The geometries obtained from these calculations were used to generate frontier orbitals and calculate the electrostatic potential. This same analysis was done with optimized transition states. From these calculations, frontier orbitals and electrostatic potentials, can be calculated to rationalize the effect structure has on reactivity.

Ruthenium (V) Oxo Complexes

Of the complexes selected, only the AHA derivative, complex **3**, has a reported x-ray structure. A direct comparison of the x-ray crystal structure to the geometries predicted by B3LYP and OPBE shows a maximum deviation of the bond lengths between Ru and the coordinating atoms of 0.049 Å and 0.043 Å respectively. The bond angles deviated by 1.7° and 2.8° for B3LYP and OPBE. These deviations are greater than those observed in crystallographic methods[25]. They are also greater than the deviations observed by Jiménez-Hoyos.[26] However, they are comparable to the overestimation in bond length and bond angle associated with B3LYP identified by Minenkov, with OPBE performing slightly better with respect to bond length, and B3LYP performing slightly better with respect to bond angle.[27]

No other crystal structures could be found for any of the other ruthenium (V) oxo complexes. However, there exists a crystal structure for a bridged μ-oxo porphyrin ruthenium

chloride $O[(Por)RuCl]_2$, whose bond lengths and bond angles with respect to the equatorial coordination sphere should be comparable absent severe distortion of the porphyrin ring.[51] In this regard, for B3LYP there is a maximum deviation from the reported μ-oxo complex of 0.041 Å and 3.5°. In spite of the uncertainty of the axial components of the coordination sphere, the agreement along the equatorial plane gives us some confidence in the accuracy of the geometries obtained by DFT for complex **4**. This alongside the data for complex **3** suggests that both B3LYP and OPBE are slightly overestimating the bond lengths in the coordination sphere. However, this overestimation is similar to that predicted by Minenkov, et al.[27] This tells us that both B3LYP and OPBE are well-behaved and are performing characteristically for this set of Ru-oxo compounds.

Of the $LRu^{V}O$ complexes, only **3** and **5** have reported magnetic moment data. The reported magnetic moment of **5** is 3.90 μ_B, which agrees well with the spin only magnetic moment of 3.87 μ_B expected for a d^3 high spin metal.[30] This suggests a ground state spin of 3/2 (quartet), in agreement with the predictions made by both B3LYP and M06. OPBE on the other hand predicts a low spin of 1/2 (doublet). The failure of OPBE to correctly predict the ground state spin state can be partially ascribed to the lack of HF-exchange that is normally included in hybrid functionals. The inclusion of HF-exchange in hybrid functionals tends to stabilize high spin states. The lack thereof in OPBE suggests that the OPBE does not adequately treat the exchange interaction in this case. Complex **3** has a magnetic moment of 1.70 μ_B, close to the spin only moment for a d^1 metal of 1.73 μ_B. This corresponds to a spin of 1/2, with a little contamination from the angular magnetic moment. This is in agreement with the low spin state predicted by all three functionals.

Without experimental data for the magnetic moments of the remaining complexes, we can look for general agreement amongst the three functionals to give some measure of certainty of the ground state spin state. Figure (7) shows the free energy difference between the quartet and doublet states with the 3 functionals, excluding complex **4** and the B3LYP difference for complex **5**. A positive energy difference (bar above 0) corresponds to a favored doublet ground state, and a negative energy difference (bar below 0) corresponds to a quartet ground state. For the NTA complexes (**2a**, **2bH$_2$O**, **2bNH$_3$**, **2bPyr**) all functionals predict a doublet ground state. All functionals predict complex **1b** ([BDA(Py)RuO]$^+$) to have a quartet ground state. A ground state geometry could not be optimized for complex **1a** ([BDA(Py)$_2$RuO]$^+$) with OPBE, but both B3LYP and M06 predict the ground state to be a doublet.

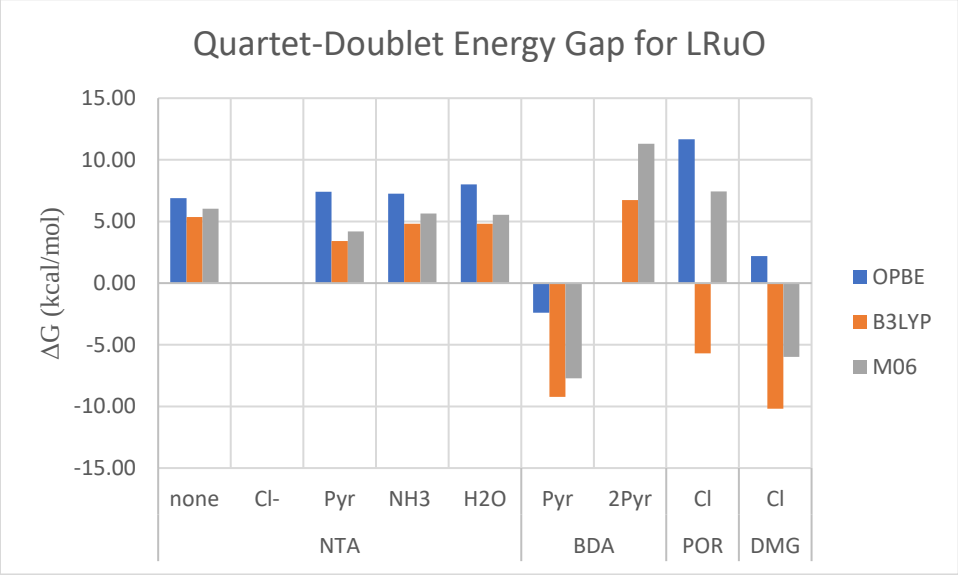

Figure 7: Free energy difference between quartet and doublet states for LRuO complexes.

In spite of the general agreement amongst functionals, the likely ground state multiplicity of complex **4** is unclear. Both OPBE and M06 predict complex **4** to be a doublet, while B3LYP predicts it to be a quartet. The disagreement between the two hybrid functionals and the

agreement between M06 and OPBE offers no clear explanation for which functional is more reliable. The lack of experimental data leaves this issue somewhat unresolved, requiring an in-depth analysis of the formulation of each of these functionals, which is outside the scope of this work. To this end, precedence from the literature must be used to inform what significance we assign to each functional. Work by Hughes highlights the tendency of B3LYP to stabilize low spin states, noting that B3LYP can overestimate the pairing energy of t_{2g} and e_g electrons in 3d metal complexes by anywhere from 1.77-11.95 kcal/mol.[52] This means that B3LYP is biased towards low spin states, so a prediction of a high spin ground state should be reliable. In terms of x-ray structures, OPBE shows a slightly smaller deviation on bond lengths for available geometries, but it shows a higher deviation in bond angles and fails to predict the ground state spin state of complex **5**. For this reason, B3LYP should be considered the better option for predicting ground state geometries and spin states among ruthenium(V)-oxo complexes.

Most of the compounds surveyed have a somewhat distorted octahedral geometry, the exceptions being complex **3** and **2a**, which both have distorted trigonal bipyramidal geometries. The hepta-coordinate complex **1a** has a severely distorted pentagonal bipyramidal geometry. Of these complexes, **1a**, **1b**, **4**, and **5** all feature extended pi-bonding ligand networks. There is also some parallel between the BDA and NTA complexes with respect to the placement of the reactive oxygen atom. On the ligated NTA complexes (**2b**) we can define the z-axis as being the one connecting the NTA nitrogen to Ru then to the ligand as pictured below. For complex 1a this is the axis running from pyridine to Ru to pyridine. The equatorial plane is then considered the plane that contains the oxo group, the oxygens from the ligating carboxylates from NTA and the bipyridine backbone for the BDA complex.

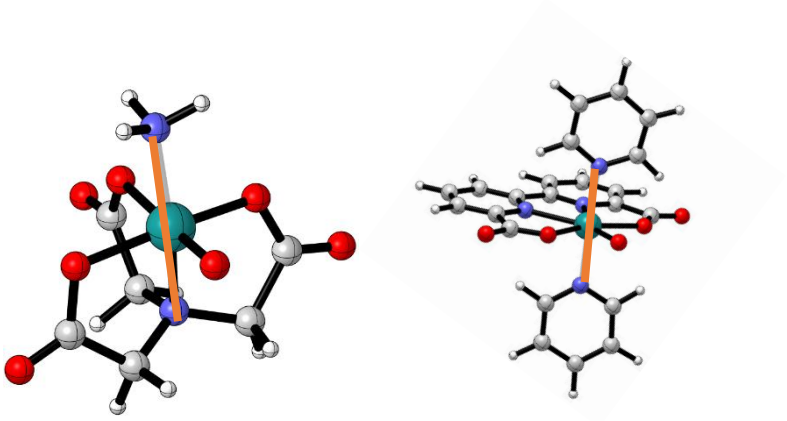

*Figure 8: Structures of complexes **1a** (right) and **2bNH$_3$** (left) with the z axis in orange.*

In complex **1b** the Ru-oxo group lies along the z-axis, rather than the equatorial plane, similar to complex **2a**. In the case of complexes **1a** and **1b**, the dissociation of pyridine and movement of the oxo group is uphill by 9.9 kcal/mol as determined by B3LYP. With this in mind an equilibrium mixture of the two would be expected to contain an overwhelming amount of **1a** vs **1b**, as judged by $\Delta G° = -RTln(K_{eq})$. We were unable to optimize a non-ligated NTA species with an equatorial oxo, but the species ligated with water, ammonia and pyridine exhibit the same preference for the equatorial oxo by an average 5 kcal/mol. We should expect the reactivity of these complexes to be modulated by the location of the reactive oxo-group and in fact the computations show this below.

Table 1: Ruthenium oxo spin multiplicities and bond lengths (quartet complexes highlighted in orange).

Complex	Formal Charge	Spin Multiplicity	Ru-Oxo Bond Length (Å)
4	0	q	1.79
5		q	1.80
2a		d	1.72
2b L = H_2O		d	1.74
2b L = NH_3		d	1.74
2b L = Pyr		d	1.74
2b L = Cl^-	-1	d	1.71*
3		d	1.72
1a	1	d	1.77
1b		q	1.79

The ruthenium-oxo bond lengths all lie between 1.71 and 1.80 Å. The electronic structure of metal-oxo species as rationalized by Winkler suggests that these moieties typically have multiple bond character, ranging from a bond order of 1.5 to 3.[53] The frontier orbitals for these species include a non-bonding metal centered orbital, and a pair of degenerate pi antibonding orbitals. Three lower energy bonding orbitals give low spin d^0, d^1, and d^2 complexes a bond order of 3 with respect to the Ru-O bond. The occupation of the metal centered orbital does not affect the M-O bond order, but occupation of the antibonding orbitals reduces the bond order. The ruthenium (V) oxo complexes are considered to be d^3 metals. For these d^3 complexes, high spin quartet species are expected to have a bond order of 2, while low spin doublet species have a slightly higher bond order of 2.5. Thus, high spin metal-oxo complexes should have longer M-O bond lengths than low spin complexes. This observation is borne out in the bond lengths of the three quartet species, which have the longest Ru-oxo bond lengths of the set. With the exception of **1a**, whose increased bond length can be in part attributed to the strained pentagonal bipyramidal geometry, there exists a minimum difference of 0.05 Å between the quartet and doublet species, reflecting the difference of bond order between these species. This model for the

electronic structure of these complexes is further confirmed by a small set of d^4 Ru-oxo complexes reported by Mayer, which have an average bond length of 1.784 Å and a bond order of 2, matching the quartet species which have a bond order of 2, and whose Ru-oxo bond lengths range from 1.79-1.80 Å.[54]

Table 2: Non-bonding and anti-bonding frontier orbitals of general metal-oxo species from Winkler, et al.[53]

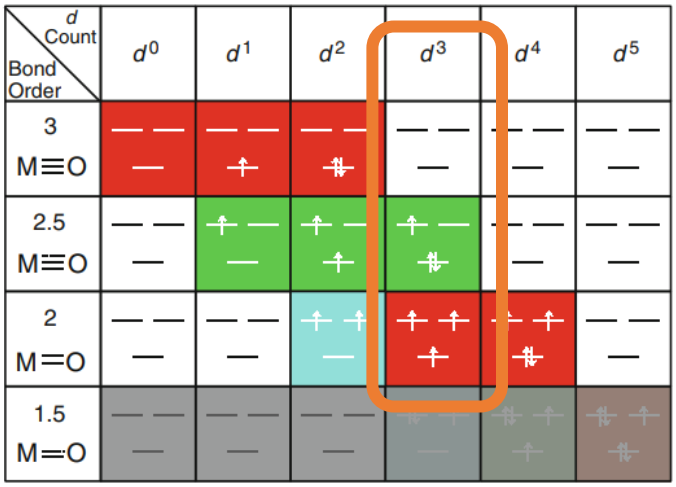

In this bonding scheme, the highest energy unpaired electron(s) in both the low spin doublet and high spin quartet species should be localized in a Ru-oxo pi anti-bonding orbital. This is reflected in both the Mulliken spin density and SOMOs of the complexes selected. The Mulliken spin density shows that the predominant location of the spin density is on the ruthenium-oxo group, with the relative density on Ru and O varying. This is reflected in the SOMO(HOMO)s of all of the complexes except for **1a**. For the majority of the complexes, the HOMOs can be characterized as pi anti-bonding with respect to the Ru-oxo bond, as shown below. The main differences amongst these complexes are the metal orbital character and the extent of delocalization throughout the auxiliary ligands. Complex **1a** on the other hand contains

no electron density on Ru in the HOMO. In this case, the HOMO appears to only contain electron density on oxygen and delocalized through the carboxylates in a pi anti-bonding fashion.

*Table 3: B3LYP derived Mulliken spin density. *denotes spin density determined by OPBE*

Complex	Formal Charge	Spin Multiplicity	Mulliken Spin Density	
			Ru	O
4	0	q	0.93	0.98
5		q	0.86	1.04
2a		d	0.47	0.75
2b L = H_2O		d	0.46	0.59
2b L = NH_3		d	0.46	0.57
2b L = Pyr		d	0.45	0.57
2b L = Cl^-	-1	d	0.37*	0.84*
3		d	0.63	0.32
1a	1	d	0.35	0.73
1b		q	1.48	1.14

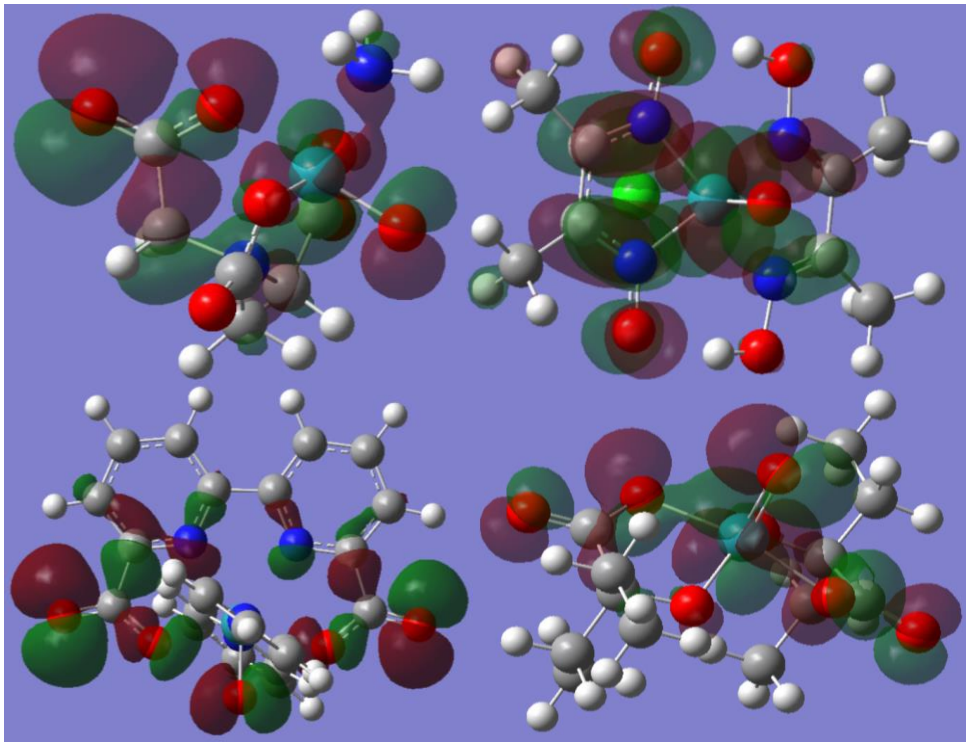

*Figure 9: HOMO(SOMO) for complexes **2bNH$_3$** (top left), **4** (top right), **1a** (bottom left), and **3** (bottom right). Nitrogen is blue, oxygen is red, ruthenium is cyan, chlorine is green.*

For the coupling reaction to occur and for O-O bond formation to take place, we should expect oxygen-centered orbitals to constructively overlap. When the LRuO species begin to approach each other, we expect their molecular frontier orbitals to begin to overlap and form new molecular orbitals. In this case, these orbitals are the Ru-oxo pi antibonding orbitals. Constructive overlap of the two antibonding orbitals is then at least partially responsible for coupling reaction to occur. To this end the HOMO of these species are critically important in bonding and should have a significant contribution to the coupling reaction.

The LUMOs are in general also pi anti-bonding (including for **1a**), but usually have different metal orbital character from that in the HOMO (i.e. HOMO is d_{xz}/d_{yz} and LUMO is d_{xy}/d_{x2-y2}). This reflects the Ru-oxo electronic structure presented above, with some degeneracy breaking due a Jahn-Teller-esque distortion. The exception to this is complex **4**, which contains lone pair density on the oxygen and pi density along the dmg ligand with imine character. Outside of any external reductions, we should not expect the LUMOs to be important in the coupling reaction. However, their pi anti-bonding characteristics suggest that a reduction may in fact facilitate bond formation by further weakening the Ru-oxo bond.

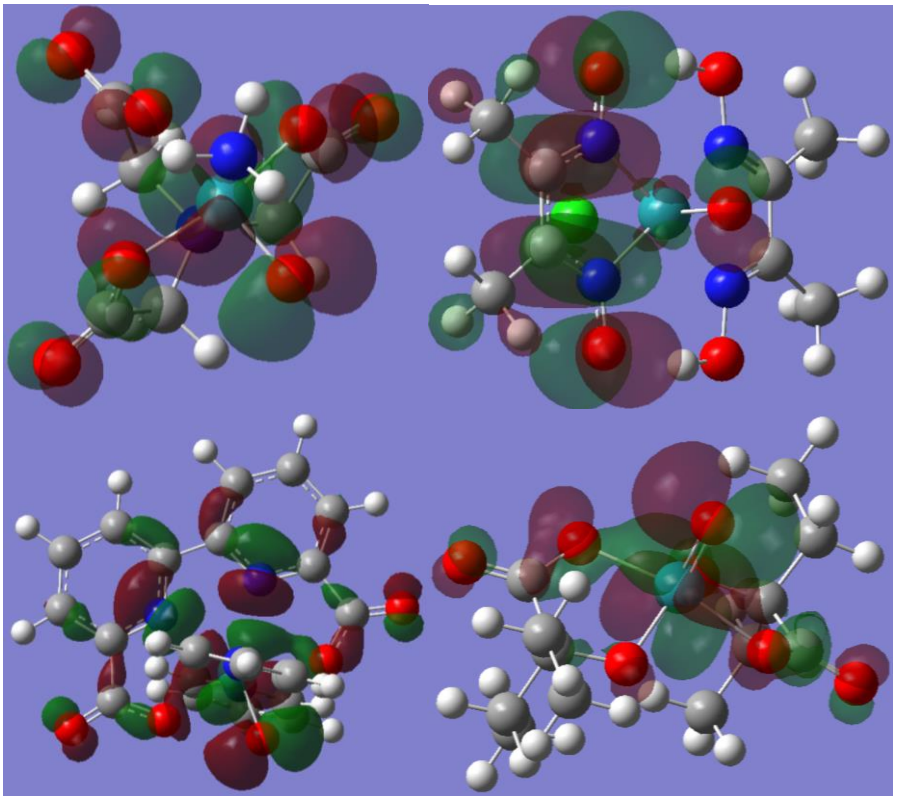

Figure 10: LUMO for complexes ***2bNH₃*** *(top left),* ***4*** *(top right),* ***1a*** *(bottom left), and* ***3*** *(bottom right).*

Peroxide-Bridged Complexes and O-O Coupling

Upon optimization, the bridged peroxides formed from Ru-oxo coupling show a lengthening of the Ru-O bond relative to the $LRu^{V}O$ monomers by 0.2 Å on average. The difference between Ru-O bond distance in the dimer vs. the monomer ranges from 0.12 Å for complex **8** to 0.28 Å for complex **7bNH₃**. The series of **7b** complexes are amongst the complexes that show the greatest change in Ru-O length, alongside complex **9**. The resulting O-O bond lengths range from 1.32 Å for complex **9** to 1.49 Å for complex **8**.

Table 4: Relevant bond distances in LRuO and $(LRuO)_2$ species.

Complex	Formal Charge	Monomer Ru-O Distance (Å)	Dimer			Dimer and Monomer Ru-O Diff. (Å)
			Ru(1)-O(1) Distance (Å)	Ru(2)-O(2) Distance (Å)	O(1)-O(2) Distance (Å)	
9	0	1.79	2.01	2.01	1.32	0.22
10		1.80	1.95	1.95	1.39	0.15
7a		1.72	1.92	1.92	1.41	0.20
7b L = H_2O		1.74	1.91	2.00	1.38	0.22
7b L = NH_3		1.74	2.00(9)	2.01(6)	1.35	0.28
7b L = Pyr		1.74	2.02	2.00	1.34	0.27
7Cl	-1	1.71*	1.95*	1.95*	1.31*	0.24
8		1.72	1.84	1.84	1.49	0.12
6a	1	1.77	1.93	1.93	1.38	0.16
6b		1.79	1.99	1.97	1.34	0.19

All complexes have O-O lengths between 1.32-1.49 Å. This places them close to the range between the superoxide (BO = 1.5) and the peroxide (BO = 1) as shown below.[55] The mid-point of this range is 1.41 Å, so O-O bond lengths above this have a weaker O-O bond and more peroxide character, whereas O-O bond lengths between 1.32 and 1.41 Å have a slightly stronger O-O bond and more superoxide character.

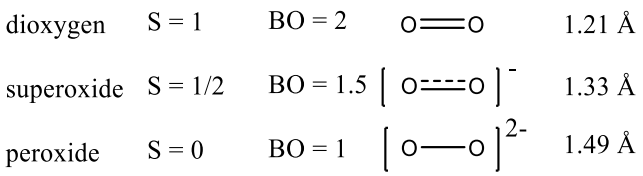

Figure 11: Bonding parameters for various oxidation states of dioxygen species.

The O-O bond length can then be used to rationalize the electronic structure of the bridging oxygen atoms, and by proxy infer the electronic environment of the Ru metal center. The Ru-O bond length on average increases by 0.21 Å from the monomer to the dimer, reflecting a decrease in bond order for the Ru-oxo bond. This decrease in bond order, is accompanied by the formation of the O-O bond. Of the complexes selected, there is a clear correlation between the O-O bond length and the Ru-oxo length in the coupled product, as shown below. As the O-O

bond becomes stronger and shorter, the Ru-oxo bond becomes longer and weaker. This corresponds to an increased donation of electrons from the Ru-oxo bond to the O-O bond, changing the O-O character from a peroxide to the shorter superoxide.

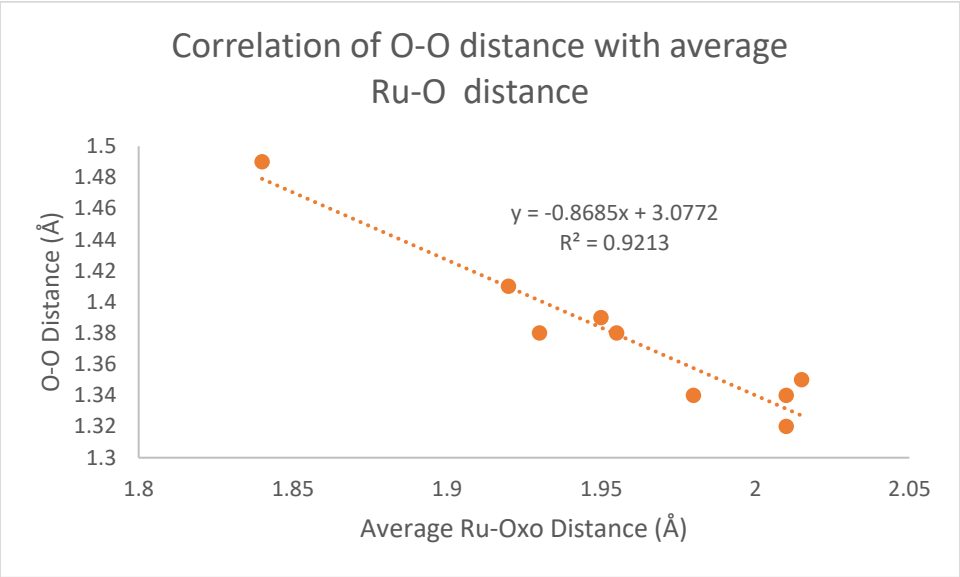

Figure 12: Relationship between O-O bond and Ru-O bond lengths in bridged peroxide complexes.

The only complex above the 1.41 Å threshold is the AHA dimer, complex **8**, whose O-O bond is precisely the length of the peroxide ion. The electronic structure of the doublet Ru-oxo monomer includes an occupied non-bonding metal-based orbital, a partially occupied pi anti-bonding orbital and another destabilized pi anti-bonding orbital of a different symmetry. It stands to reason that overlap of the partially occupied pi anti-bonding orbitals form the O-O bonding orbital. This is confirmed by the frontier orbitals of the complex **8**, whose HOMO shows the pi anti-bonding character on each Ru-oxo group and the subsequent overlap of these orbitals forming the O-O bond. In the same vein the LUMO here corresponds to the destabilized Ru-oxo pi anti-bonding orbitals overlapping and forming another O-O bonding orbital. The O-O distances for the remaining complexes all fall between 1.32 and 1.41 Å, with varying superoxide

and peroxide character. The frontier orbitals for these complexes do not appear to follow the same rationale as presented for complex 8, suggesting a more drastic electronic rearrangement.

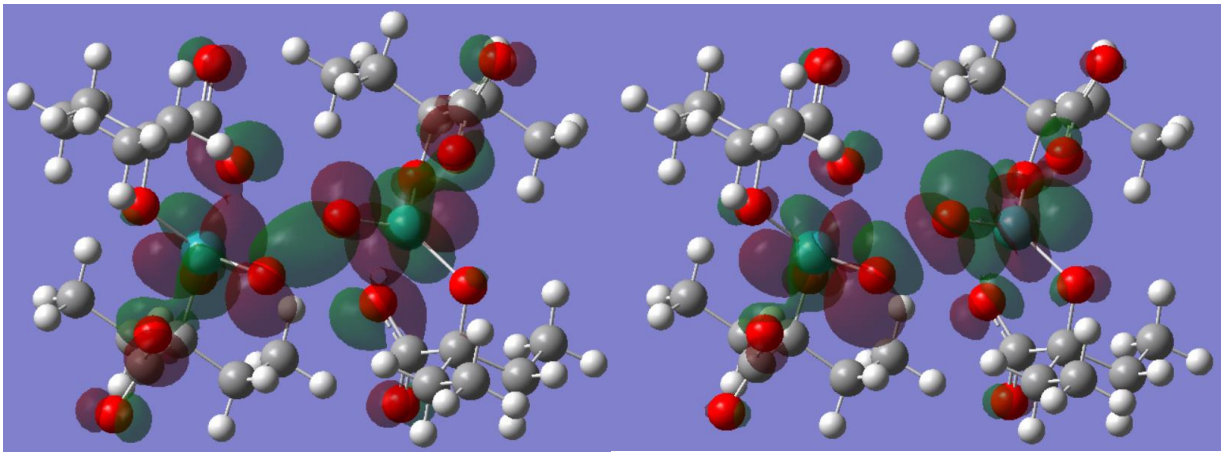

*Figure 13: HOMO (left) and LUMO (right) of complex **8**. O is red, Ru is cyan.*

A majority of the bridged peroxide complexes show a significant favoring of a triplet ground state, with the primary exception being complex **7a**. Triplet states for the bridged peroxides of complex **6a** (BDA), **7Cl** (NTACl$^-$), and **8** (AHA) were unable to be optimized with any functional. With complexes **6a**, **7Cl**, and **8** excluded, all functionals qualitatively make the prediction that the triplet is more stable, although the triplet-singlet gap is typically 5 kcal/mol smaller for OPBE than it is for B3LYP and M06.

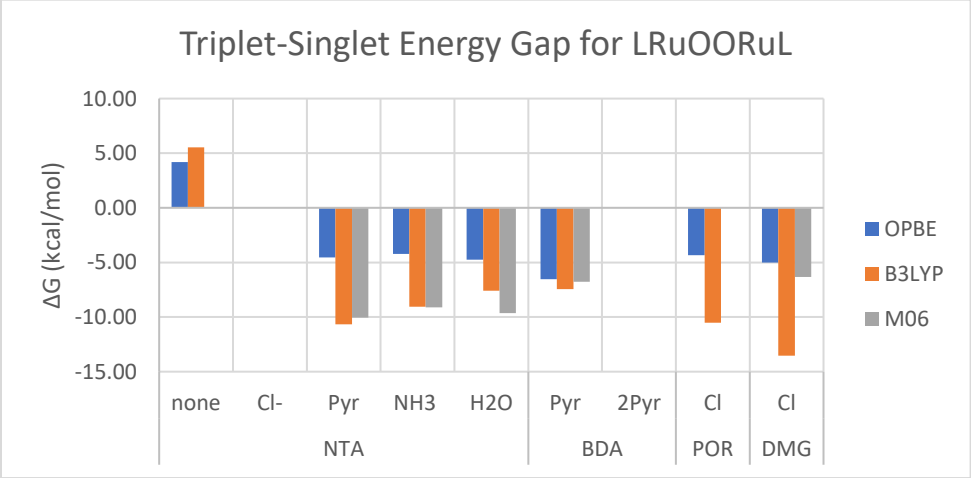

Figure 14: Free energy difference between triplet and singlet states for $(LRuO)_2$ species.

Table 5: Mulliken spin density on Ru-O groups in bridged peroxide complexes.

Complex	Formal Charge	Spin Multiplicity	Mulliken Spin Density			
			Ru1	O1	O2	Ru2
9	0	t	1.01	-0.40	-0.40	1.01
10		t	-0.00(4)	0.13	0.10	-0.06
7a		s	0.00	0.00	0.00	0.00
7b L = H_2O		t	0.20	-0.16	0.03	1.44
7b L = NH_3		t	0.47	-0.36	-0.15	1.40
7b L = Pyr		t	0.51	-0.40	-0.18	1.39
7Cl	-2	s	0*	0*	0*	0*
8		s	0	0	0	0
6a	2	s	0	0	0	0
6b		t	0.25	0.43	0.32	0.77

If the remaining complexes do in fact have superoxide character, we should expect asymmetry in the electronic and molecular structure, due its monoanionic and monoradical character. For complexes that have singlet ground states there is no net spin density. For the triplet complexes, there is a calculated asymmetry in the spin density for all of the complexes except for **9** (POR) and **10** (DMG). For the remaining triplet complexes (**6b** and **7b**) we also observe asymmetry in the Ru-oxo bond lengths and the Mulliken spin density. The HOMOs for these complexes are primarily localized on the moiety that contains the longer Ru-O bond with the exception of **7bNH$_3$** which is localized on the moiety with the shorter Ru-O bond. These orbitals are mainly localized on Ru and on the ligand backbone (BDA, NTA), with some weak pi anti-bonding character on the O-O group. With the exception of complex **7bH$_2$O**, the asymmetry in the Ru-oxo bond distance from the low spin moiety to the high spin moiety is 0.02 Å at the most. For complexes **7bH$_2$O** and **7bNH$_3$** the slightly shorter Ru-O bond is found on the low spin moiety, while on complex **6b** and **7bPyr**, it is found on the high spin moiety. The significance of this pairing between bond length and high/low spin moiety is not clear.

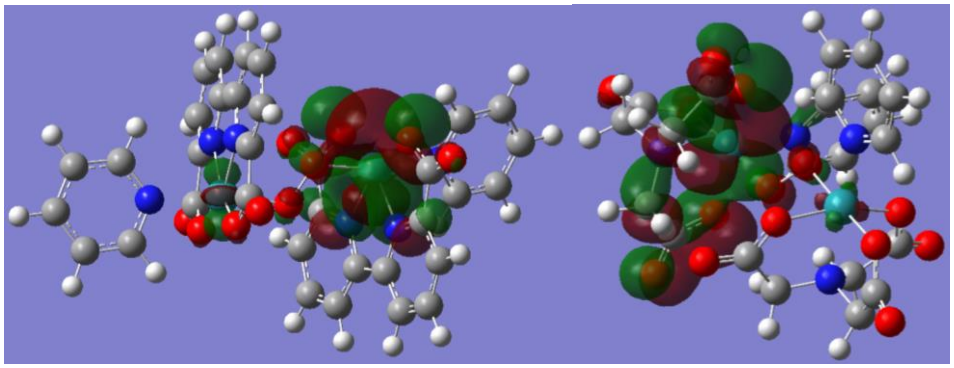

*Figure 15: HOMOs of bridged peroxides for complexes **6b** (left) and **7bPyr** (right).*

Complex **9** (POR) contains a completely symmetrical Mulliken spin density, localizing primarily on the Ru atoms and on the pi-system of the porphyrin ligand. Complex **10** (DMG) on the other hand contains very little spin density localized on either atom of the Ru-O group. For this complex most of the Mulliken spin density is found around the DMG ligands. HOMOs of bridged peroxides of complexes **9** and **10** resemble their respective LRuO HOMOs, showing antibonding character with respect to Ru-oxo bond. This is also the case for complex **6a** (BDA). Complexes **6a** and **9** shows a pi bonding interaction between the bridging oxygens, similar to complex **8** (AHA). Complex **10** shows a very weak interaction between Ru and the bridging oxygens, and a weak antibonding interaction between the bridging oxygens. This suggests that oxidation of complex **10** may promote the strengthening of the O-O bond, possibly promoting the metal dissociation step.

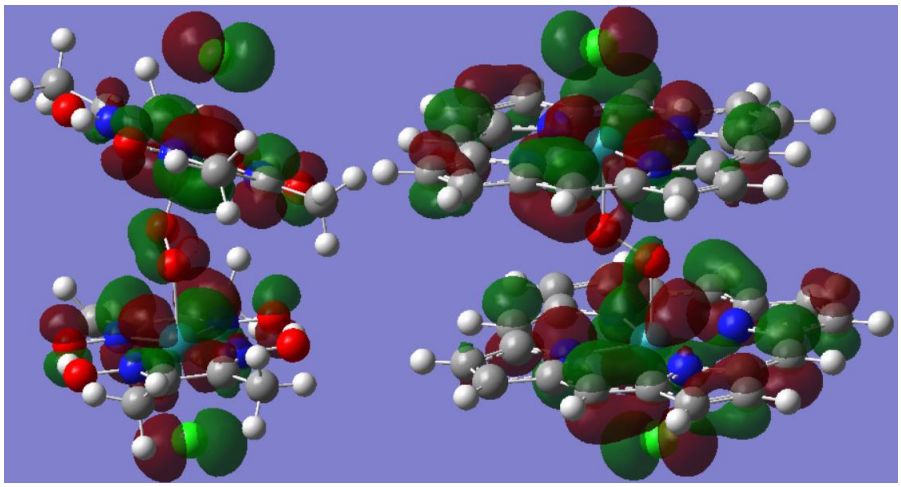

*Figure 16: HOMOs of the bridged peroxides of complexes **10** (left) and **9** (right).*

The LUMOs for the **6b** and **7b** complexes are essentially the same as the HOMOs. They predominately feature substantial coefficients on ruthenium and along the ligand, with weak pi antibonding character on the O-O and Ru-O bonds. However, the metal and ligand electron density is localized on the moiety opposite of the one where it was localized in the HOMO.

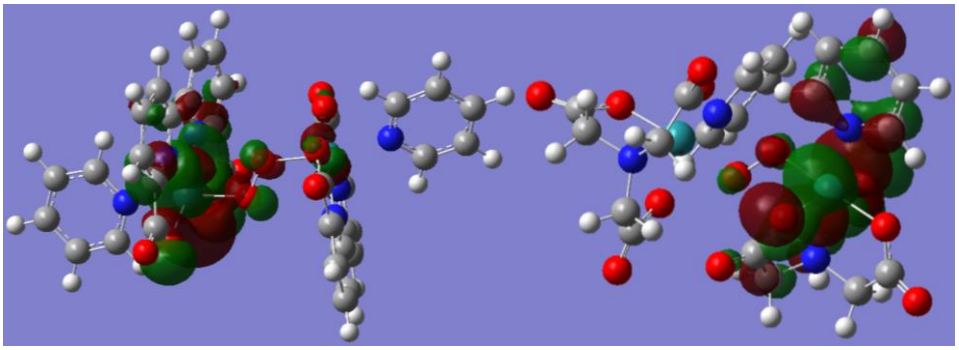

*Figure 17: LUMOs for complex **6b** (left) and **7bPyr** (right).*

The LUMOs for complexes **7a**, **9**, and **10** are anti-bonding with respect to the Ru-O bonds. Both **7a** and **10** feature pi bonding interactions in the O-O bond, while complex **9** exhibits sigma bonding interactions. The LUMO for **6a** is pi antibonding with respect to both the Ru-O

bond and the O-O bond. The location of the electron density on complexes **7a**, **9**, and **10** suggest that reduction, rather than oxidation, may be able to drive the metal dissociation reaction.

With the exception of complex **7a**, the RuOO bond angles all fall within a range of 6°, from 114.8° for complex **10** to 120.6° for complex **7bCl**. The electronic structure of the Ru-O-O-Ru group suggests that the bond order for the O-O bond ranges from 1.5-1, so the bond itself is likely fairly flexible. This is reflected in the larger variation of the dihedral angles θRuOORu, which ranges from 98.9° to 179.2°. Complexes **7a**, **7bNH$_3$**, **7bH$_2$O**, and **8** have the smallest dihedral angles.

Table 6: Bonding lengths and dihedral angles for bridged peroxide complexes.

Complex	Formal Charge	Ru(1)O(1)O(2)°	Ru(2)O(2)O(1)°	Dihedral θRuOORu°
9	0	116.4	116.4	177.4
10		114.8	116.3	155.7
7a		104.8	108.8	132.8
7b L = H$_2$O		115.7	116.2	108.8
7b L = NH$_3$		116.5	116.5	145.5
7b L = Pyr		116.9	115.2	175.6
7b L = Cl$^-$	-2	119.2*	120.6*	179.2*
8		119.5	119.5	98.9
6a	2	116.0	116.0	177.8
6b		119.0	117.9	164.7

Complexes **7bNH$_3$** and **7bH$_2$O** (NTA) both feature hydrogen bonding between the axial NH$_3$/H$_2$O and a carboxylate on the adjacent NTA ligand, as pictured below. Their relatively small dihedral angles can be attributed in part due to this hydrogen bonding. In general, the best hydrogen bonding ligand is H$_2$O, followed by NH$_3$ then pyridine, which does not typically engage in C-H hydrogen bonding. Complex **7bH$_2$O** has the shortest and strongest hydrogen bond at 1.74 Å, yielding the smallest dihedral angle at 108.8° for the **7a** and **7b** complexes. Complex **7bNH$_3$** has a weaker hydrogen bond at 2.42 Å and an expanded dihedral angle of 145.5°.

Complex **7bPyr** contains one very weak hydrogen bond at a length of 2.58 Å and has one of the greatest dihedral angles of the complexes surveyed.

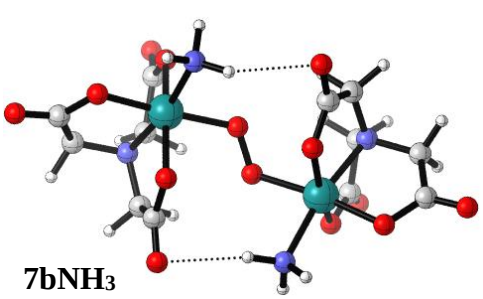

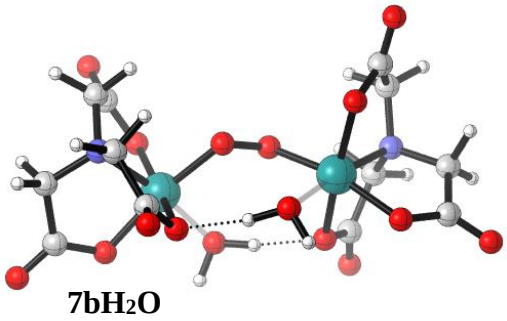

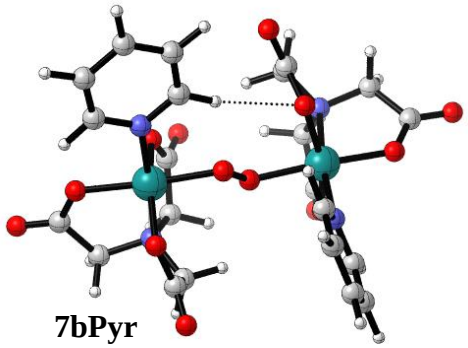

Complex	Dihedral θRuOORu°	Hydrogen Bonding Distance (Å)
7a	132.8	-
7b L = H_2O	108.8	1.75
7b L = NH_3	145.5	2.42
7b L = Pyr	175.6	2.58
8	98.9	-

*Figure 18: Structures of **7b** complexes, highlighting hydrogen bonding and dihedral angles.*

No hydrogen bonding interactions can be identified for complexes **7a** (NTA) and **8** (AHA). However, the electrostatic potential can be used to rationalize the small dihedral angle. In complex **7a**, the smaller dihedral angle brings one of the coordinating carboxylates of NTA closer to the opposite ruthenium center, screening some of the partial negative and positive charges on the carboxylate and on the ruthenium. This screening is more evident in complex **8**, where the small dihedral angle brings one of the ethyl groups on the AHA ligand in close proximity to a carboxylate on the AHA ligand on the opposite monomer.

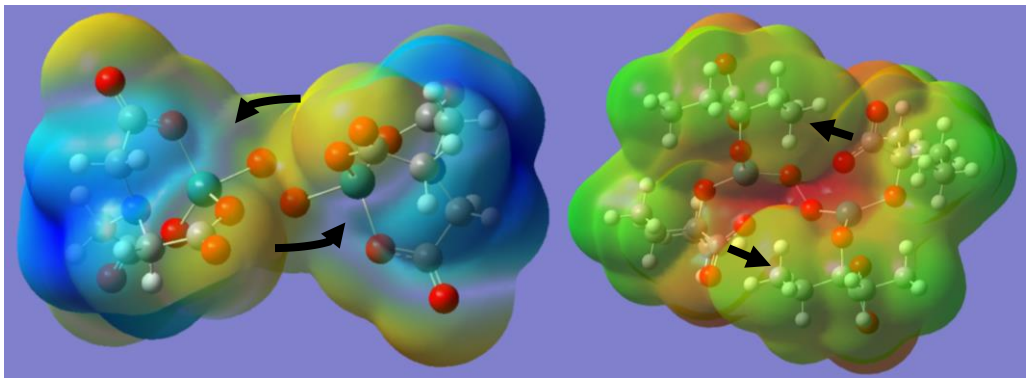

*Figure 19: Electrostatic potential (ESP) for complex **7a** (left|NTA) and **8** (right|AHA), illustrating the partial screening of charge. Left: Blue is partial positive, yellow is partial negative. Right: Green is small partial negative, red is large partial negative.*

The asymmetry found in these complexes is fairly small, with bond lengths and bond angles across the low and high spin monomers only differing by a maximum of 0.02 Å and 1.7°. These small differences in bond lengths and bond angles likely cannot be resolved in any meaningful way by x-ray crystallography, because they are very close in magnitude to the experimental deviation. In addition, there does not at present seem to be any meaningful distinction that explains the tendency for which monomer will have a bigger or smaller bond length or angle. With that being said, complex **7bH$_2$O** has a much large difference between Ru-oxo bond lengths (1.91 Å vs 2.00 Å), albeit the second smallest discrepancy of bond angle (115.7° vs. 116.2°). It is possible that this difference could be identified by x-ray crystallography.

The difference in spin density could also be accounted for by careful EPR studies. The EPR spectrum is sensitive to the location of electron density due to spin-orbit and hyperfine coupling. Unpaired electrons on organic substrates typically exhibit a g-factor fairly close to the free electron value of 2.0023. Transition metals can vary considerably from the free electron g-factor due to a large non-zero orbital angular momentum, therefore unpaired electrons localized on the metal centers should be fairly easy to identify. In terms of hyperfine coupling both Ru and O have isotopes with a spin of 5/2, predicting each to give a sextet splitting (if we consider an

isotropic system). However, the abundance of these spin-active isotopes is considerably different. The spin-active isotopes ^{99}Ru and ^{101}Ru make-up 29.82% of naturally occurring ruthenium, while the spin-active ^{17}O makes up just 0.04% of naturally occurring oxygen. All other naturally occurring isotopes for Ru and O have a spin of 0. Any hyperfine splitting that may be observed may be attributed to ruthenium due to its higher abundance. The localization of the unpaired electron density on either ruthenium, oxygen, or combination of the four would show different spectra. If the spin for a triplet complex is localized on a single ruthenium species then you might have a sextet of triplets, but if the density is evenly divided across both, then you could wind up with a much more complicated splitting (sextet of a sextet of triplets).

The thermodynamic free energy of coupling shows a large discrepancy for the **7a** and **7b** complexes, with OPBE predicting an endoergic coupling step, while B3LYP and M06 predict this step to be exoergic. As hybrid functionals, both B3LYP and M06 are known to stabilize higher spin states due to the explicit inclusion of HF-exchange. In this same vein, OPBE as a GGA could be expected to inadequately account for the exchange interaction and destabilize high spin states. In this sense, the difference in the energies is somewhat characteristic of the biases of these functionals. For complexes **6a** and **6b**, both M06 and B3LYP predict an endoergic coupling step, with complex **6a** being approximately 6 kcal/mol more favorable than complex **6b** for both functionals. OPBE predicts a similar energy to B3LYP for complex **6b**. All functionals predict the coupling step for complex **9** to be exoergic, with OPBE predicting this step to be 10 kcal/mol higher than what B3LYP and M06 predicted. The free energies for complex **10** are somewhat scattered, with M06 predicting a free energy of -4.30 kcal/mol, B3LYP predicting a free energy of 8.63 kcal/mol, and OPBE predicting a free energy of -0.64

kcal/mol. For complex **3** B3LYP and M06 predict similar free energies. OPBE and M06 predict similar free energies for complex **7Cl**.

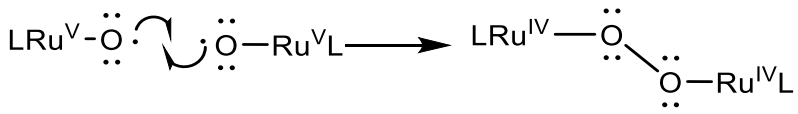

Figure 20: LRuO coupling reaction.

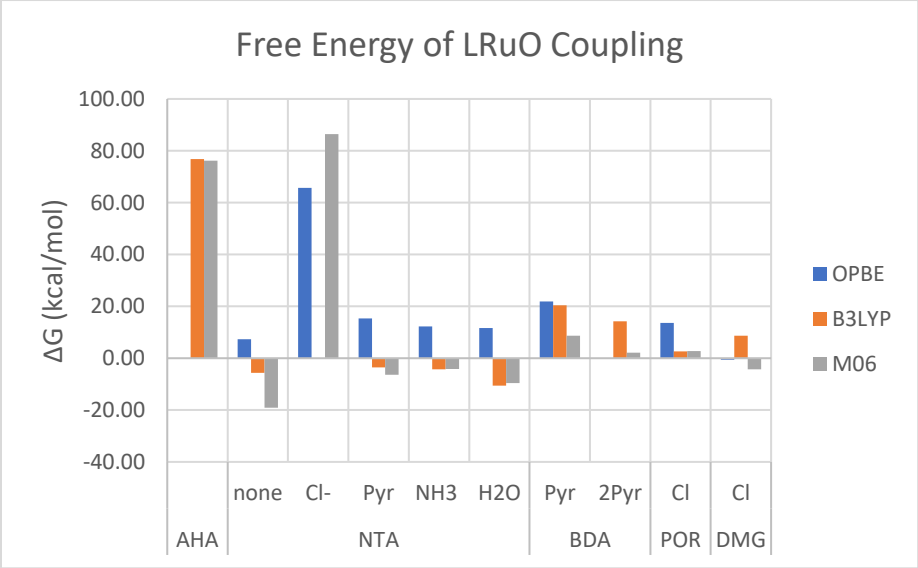

Figure 21: Free energy of coupling for LRuO complexes.

Comparing the free energy of coupling for all complexes, we can group the anionic complexes separately from the cationic and neutral complexes. Both anionic complexes have extremely large free energy barriers for coupling. Complex **8** has a free energy of 76.2 kcal/mol and complex **7Cl** has a free energy of 86.5 kcal/mol with M06. When comparing complex **7Cl** to complex **7a** and the **7b** complexes, the free energies of coupling are considerably different, ranging from -17.6 kcal/mol (**7a**) to -4.1 kcal/mol (**7bNH$_3$**). This suggests that in general, the coupling of the uncharged NTARuO(L) complexes is viable, but the addition of an anionic ligand increases electrostatic repulsion. Pairing this with the large barrier for complex **3** suggests that anionic complexes may in general be unable to readily undergo this O-O coupling reaction,

limiting the potential of anionic complexes for dioxygen evolution reactions. The O-O distances for these two complexes are on the opposite ends of the data set, with **8** (AHA) having the longest O-O distance at 1.49 and **7Cl** (NTA) having the shortest distance at 1.31 Å. This large difference suggests that the O-O bond distance may not be directly related to the coupling free energies. The remaining complexes **6a**, **6b**, **9**, and **10**, which have O-O bond distances between 1.41 Å and 1.33 Å all have modest free energies with respect to M06 (-4.30 kcal/mol to 8.70 kcal/mol).

Table 7: Free energies of LRuO coupling.

Complex	Formal Charge	ΔG (kcal/mol)		
		OPBE	B3LYP	M06
9	0	13.6	2.7	2.8
10		-0.6	8.6	-4.3
7a		7.3	-5.6	-17.6
7b L = H_2O		11.6	-10.6	-9.6
7b L = NH_3		12.2	-4.3	-4.1
7b L = Pyr		15.3	-3.6	-6.4
7b L = Cl^-	-2	65.8	~	86.5
8		~	76.8	76.2
6a	-2	~	14.2	2.1
6b		21.9	20.4	8.7

Transition states for the oxo-ruthenium coupling could be located for complexes **7a**, **7bPyr**, and **7bNH$_3$** with all 3 functionals, in addition to a transition state for complex **4** was found with OPBE. Free energies of activation for all complexes with respect to OPBE are all within a few kcal/mol of each other, ranging from 18.6-22.3 kcal/mol. For complexes **7a**, **7bNH$_3$**, and **7bPyr**, the height of the barriers are not consistent across the three functionals. Complex **7bPyr** has the highest activation energy for OPBE and M06, while **7a** has the largest activation energy for B3LYP. Complex **7bNH$_3$** has the lowest barrier for B3LYP and M06 but is higher than **7a** for OPBE.

Table 8: Transition state barrier heights for O-O coupling reaction.

	$\Delta G^{\ddagger}$ (kcal/mol)		
Complex	**OPBE**	**B3LYP**	**M06**
7a	18.6	20.7	12.8
7b L = NH_3	18.9	10.4	7.7
7b L = Pyr	22.3	16.2	21.3
9	19.4	~	~

For complex **7bNH3**, the transition state found using B3LYP shows an asymmetric stretching of both Ru-oxo bonds and an unsymmetrical spin density on the Ru-oxo unit, reminiscent of the asymmetry in the $(LRuO)_2$ ground state. Like the ground state, the higher spin monomer shows a greater bond length for the Ru-oxo bond, increasing from 1.74 to 1.85 Å (1.74 to1.77 Å for the low spin monomer). These distances are still close to the range of the d^4 complexes reported by Mayer.[54] The lengthening of the bonds here reflects the lowering of the Ru-oxo bond order, although the lengths are closer to the monomer Ru-oxo length than the dimer Ru-oxo lengths. In addition, the O-O bond distances are at least 0.22 Å (**9**) longer than the isolated peroxide bond length, suggesting at this point that there is no formal O-O bond, or if there is, it has a bond order of 0.5 or lower. The transition states themselves mainly illustrate the two monomers coming into close proximity to each other, with some slight Ru-oxo bond lengthening.

Table 9: Geometrical and electronic parameters for coupling transition states.

Complex	**Ru(1)-O(1) Distance (Å)**	**Mulliken Spin Density**		**Ru(2)-O(2) Distance (Å)**	**Mulliken Spin Density**		**O(1)-O(2) Distance (Å)**	**Dihedral θRuOORu°**
		Ru1	**O1**		**Ru2**	**O2**		
9*	1.79	0.68	0.08	1.79	0.68	0.08	1.71	179.6
7a	1.71	0	0	1.78	0	0	2.15	84.8
7b L = NH_3	1.77	0.29	0.26	1.85	1.27	-0.04	1.83	126.5
7b L = Pyr	1.81	-0.06	-0.66	1.85	1.49	0.69	1.87	167.6

The transition states of **7a**, **7bNH$_3$**, and **7bPyr** all show potential intramolecular interactions. Complexes **7bNH$_3$** and **7bPyr** appear to contain hydrogen bonding interactions, whereas complex **7a** appears to have dipole-dipole interactions. The hydrogen bonding distances for **7bNH$_3$** are shorter in the transition state than those apparent in the ground state, suggesting that intermolecular forces play a more significant role in the transition state for the coupling reaction. The transition state for complex **7a** shows a close contact between one of the coordinating carboxylates and the ruthenium atom on the opposite moiety, as well as contact between the same carboxylate and a methylene on the opposite moiety. The ground state for complex **7a** does not contain the short intermolecular distances present in the transition state. The long length of the O-O bonds and the presence of short intramolecular distances in the **7a** and **7b** transition state structures suggest that the transition state can be characterized as two monomers diffusing together and being attracted or held in place by intermolecular forces. These structures suggest that these intermolecular attractions help facilitate O-O bond formation.

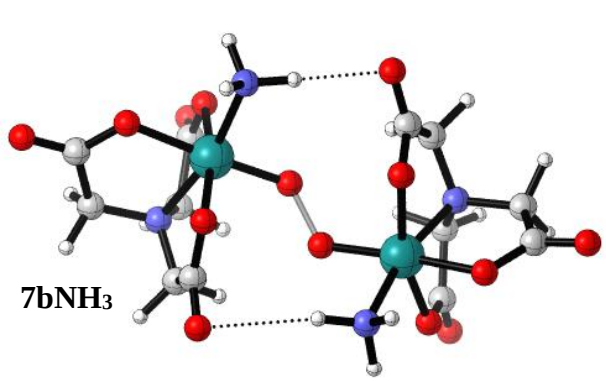

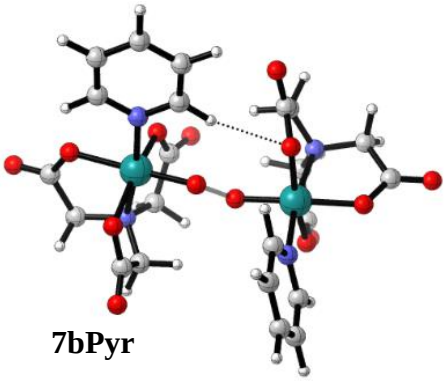

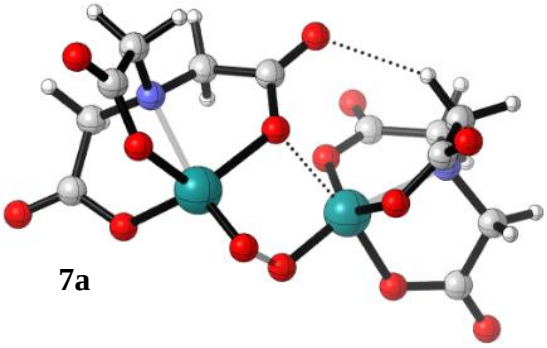

Complex	Interaction Type	Intermolecular Distances (Å)	
		$(LRuO)_2$	TS
7b L = NH_3	N-H---OCO	2.42	1.92/1.85
7b L = Pyr	C-H---OCO	2.58	2.59
7a	HC-H---OCO	~	2.42
	Ru---OCO	~	2.43

Figure 22: Intermolecular interactions for coupling transition states.

To understand the effect of solvation on the activation barrier for coupling, ground states for the LRuO and $(LRuO)_2$ were reoptimized for the **7b** complexes using the CPCM solvent model for water. The transition states for coupling were also found for complexes **7bNH$_3$** and **7bPyr** using the CPCM model for water. The lowest energy spin multiplicity remains the same in water. The mono-oxo species are doublets, and the bridged peroxides are triplets. Optimized structures show little to no deviation from the gas phase structures. The free energy of solvation for both mono-oxo species and bridged peroxides are fairly exergonic, with little variation based on the auxiliary ligand. The free energy of coupling becomes less exergonic in water, increasing by 8-9 kcal/mol, becoming endergonic in the cases of complexes **7bNH$_3$** and **7bPyr**. This increase can be accounted for by the difference in the free energy of solvation for LRuO and $(LRuO)_2$. The solvation energy for two isolated monomers is on average -42.6 kcal/mol. The free energy of solvation for the dimer is -34.0 kcal/mol on average. The difference between these two

is 8.6 kcal/mol, the same as the average difference between the aqueous and gas phase free energy of coupling. The difference between the aqueous and gas phase free energies suggests that the polar solvent is able to stabilize the mono-oxo species better than the bridged peroxide, driving up the free energy of coupling.

*Table 10: Solvation data for **2b** and **7b** complexes with B3LYP.*

Complex	ΔGsolv. LRuO	ΔGsolv. $(LRuO)_2$	$\Delta G_{coupling}$ (gas)	$\Delta G_{coupling}$ (H_2O)
7b L = Pyr	-20.7	-32.2	-3.6	5.6
7b L = NH_3	-21.8	-35.6	-4.3	3.7
7b L = H_2O	-21.4	-34.3	-10.6	-2.0

The same behavior can be seen in the transition states for **7bNH$_3$** and **7bPyr**. Comparing the free energy of solvation for the transition state to the solvation free energy of two monomers shows a discrepancy of 7.5 kcal/mol for **7bPyr** and 9.1 kcal/mol for complex **7bNH$_3$**. The average of these differences is 8.3 kcal/mol, fairly close to the difference found for the $(LRuO)_2$ ground states. The similarity here suggests that the same effect is in action here, namely the discrepancy between the ability of the solvent to stabilize the monomer vs. the dimer. The activation barriers for **7bNH$_3$** and **7bPyr** increase by 12.7 kcal/mol and 3.9 kcal/mol respectively. Despite the increase in the activation barrier for these two complexes, the barriers in water are still fairly modest at 23.1 and 20.1 kcal/mol respectively.

*Table 11: Solvation data for **7b** transition states.*

Complex	$\Delta G_{solv,TS}$ (kcal/mol)	$\Delta G^{\ddagger}$ (kcal/mol)		O-O Bond Distance		H-Bonding distance		Dihedral θRuOORu°	
		Gas	H_2O	Gas	H_2O	Gas	H_2O	Gas	H_2O
7b L = NH_3	-34.5	10.4	23.1	1.83	1.81	1.92/1.85	2.04/1.99	126.5	136.2
7b L = Pyr	-33.9	16.2	20.1	1.87	1.84	2.59	2.52 (alt.)	167.6	172.4

In terms of structural changes, there is a small contraction of the O-O bond, and a somewhat larger expansion of the intermolecular interaction distances for complex **7bNH$_3$**, likely due to the screening of the partial charges on the ammonia group. This leads to a slightly expanded Ru-O-O-Ru dihedral angle. For complex **7bPyr**, the addition of solvent leads to the pyridine that was in close contact with the opposing monomer is turned so that the plane of the ring is more perpendicular to the Ru-O bond, with a slightly closer contact between the pyridine and the carboxylate on the opposing NTA. A contracted O-O length and a somewhat expanded dihedral angle are also present here.

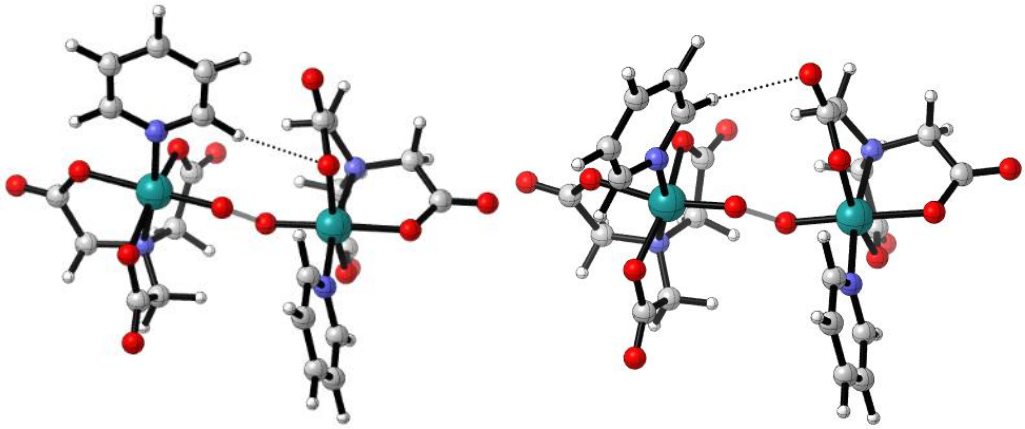

*Figure 23: Transition states for **7bNH$_3$** in gas (left) and in water (right).*

Activation barriers for the radical coupling reaction in water have been reported for a number of analogues of complex **1a**/**6a**, with variations on the BDA backbone[23] (done using M06 by Xie) and variations on the axial ligands via pyridine substitutions, and replacement of the axial ligand with isoquinoline[19] (electronic energies done using B3LYP by Kang). The activation free energies in M06 for complexes **7bNH$_3$** and **7bPyr** are 20.1 and 19.1 kcal/mol respectively. The work done by Xie yields an activation free energy of 19.8 kcal/mol for complex **6a**, with a majority of the other BDA complexes falling within a range between 11.2

and 17.2 kcal/mol (in blue below). This puts the NTA complexes fairly close to the barrier for **1a**, albeit at the upper range of the energies found by Xie. In this context the activation energies for **7bPyr** and **7bNH$_3$** are within 5-10 kcal/mol of the complexes with the lowest activation barriers, meaning they are fairly competitive with respect to the O-O coupling step.

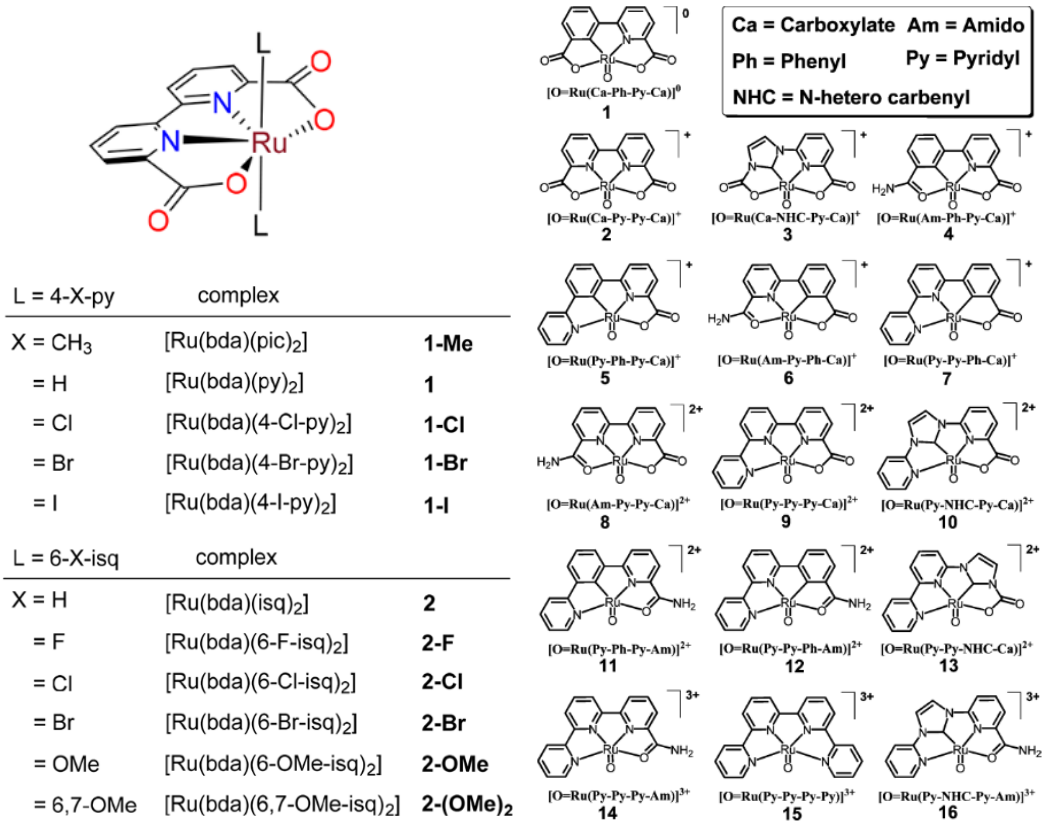

Figure 24: Complexes surveyed by Xie[19] *(left) and by Kang*[23] *(right). Figures were reproduced from their respective publications.*

Work done by Kang shows that a majority of the electronic activation energies for the variations of complex **6a** fall within the range of 10.9 to 26.9 kcal/mol. The electronic activation energies in B3LYP for **7bPyr** and **7bNH$_3$** are 7.3 and 4.7 kcal/mol respectively. This tells us two things. First, in comparing the electronic and free energy barriers for these two complexes the entropic and thermal corrections account for a significant portion of the barrier height, (-TΔS+ZPE = 15.8 and 15.4 kcal/mol). This suggests that the coupling reaction is resisted by

entropic factors. This is to be expected since the reaction itself is a diffusion of two monomers together to form a single bridged complex. This invariably leads to a decrease in entropy (and thus an increasingly positive contribution from -TΔS). In the same vein the actual energy requirements for the O-O bond formation (reflected in the electronic energy itself) are fairly small, meaning the main barrier for this reaction is entropic rather than enthalpic. Second, the electronic energies themselves are fairly small, smaller than the activation energies reported by Kang. To this end there doesn't seem to be a significant barrier to O-O bond formation from an enthalpy NTA complexes. With respect to the complexes reported by Kang, the NTA complexes perform better.

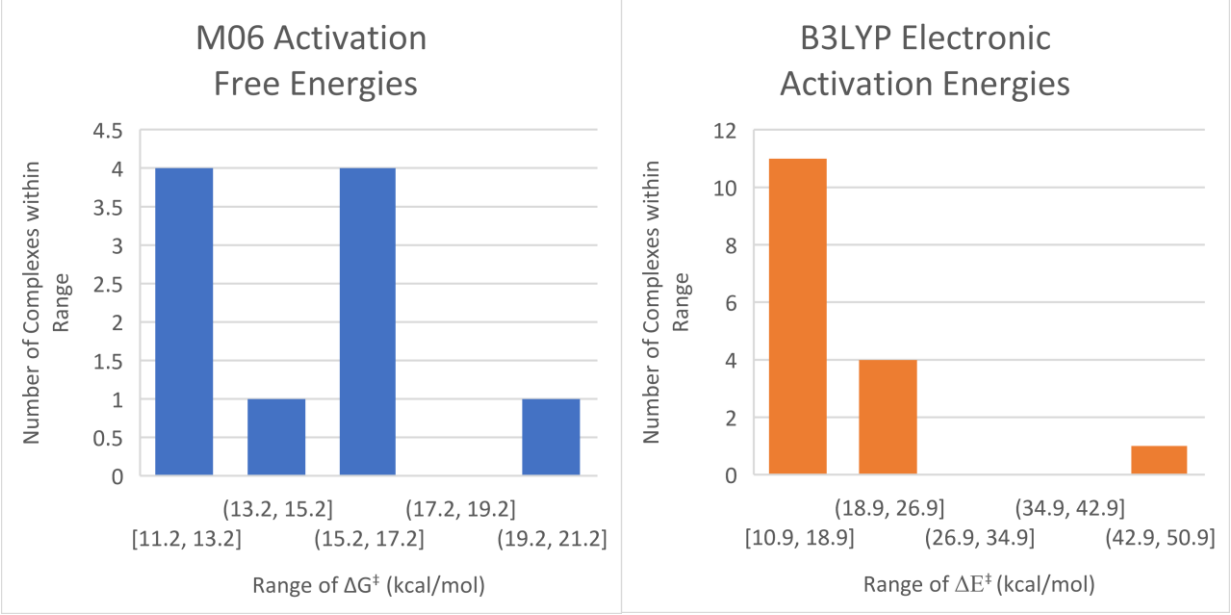

Figure 25: Activation barriers for the radical coupling reaction from Xie[19] *(left) and Kang*[23] *(right). Each entry on the x-axis represents a range of energies, the y-axis illustrates how many complexes fall within this range.*

Another aspect that was explored by Kang was the effect of the charge of the Ru-oxo complex on the activation barrier. Kang found that as the charge of the Ru-oxo increased from 0 to +3, the activation barrier increased due to electrostatic repulsion of the two Ru-oxo groups.

Adding the activation barriers for complexes **7bNH$_3$** and **7bPyr** follow this trend, having the lowest activation barriers of the set. Although activation barriers were not determined for complexes **7Cl** and **8**, there electronic reaction energies can provide us a lower limit on activation energy for O-O bond formation. If the effect of solvation is similar to that seen for the **7b** complexes, dissolving these complexes in water would likely increase the barrier and reaction energy. Qualitatively speaking, the activation barriers for these anionic complexes should be expected to be very large, in the ballpark of +50 kcal/mol or higher. In this context the neutral complexes have the lowest electronic barriers, occupying a minimum of sorts. This can still be rationalized on the basis of electrostatic repulsion. The anionic complexes feature significant repulsion due to the more diffuse nature of anions. At neutral, there is no significant repulsion, thus the activation barrier is directly related to formation of the O-O bond. As the cationic complexes increase in charge from +1 to +3, the activation barrier increases, with the tricationic complexes having the largest barriers on pair with the anionic complexes. To this end neutral and monocationic complexes are the best candidates for a low barrier to O-O bond formation.

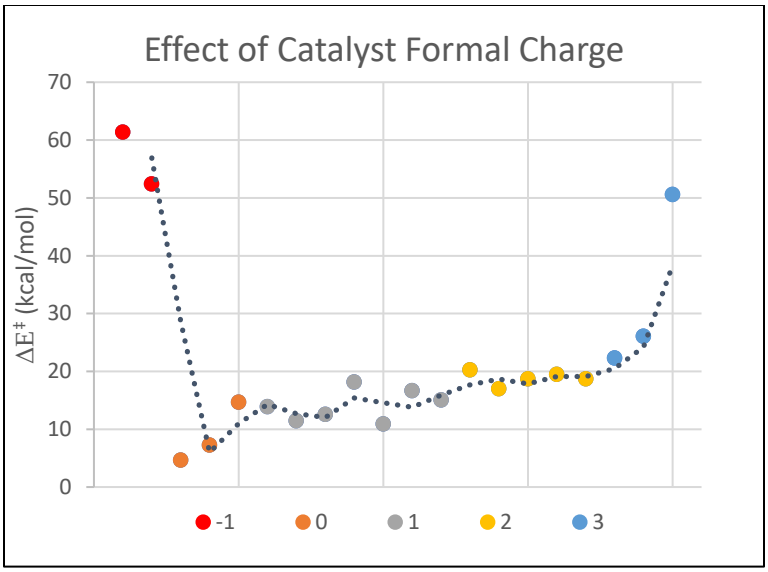

*Figure 26: Electronic activation energies for radical coupling step. Energies for anionic complexes **8** and **7Cl** are thermodynamic electronic energies of reaction in the gas phase. Reaction energy for complex **7Cl** was calculated with OPBE.*

Ruthenium Dioxygen Complexes and Metal Dissociation

The optimized structures of the ruthenium dioxygen complexes show lengthening of the Ru-O bond along with contraction of the O-O bond, in comparison to the bridged peroxide. Dioxygen complexes for complex **11b** or **12Cl** ($BDA(Py)_2$ and $NTACl^-$) could not be optimized. In every other case except for complex **12a** and **13**, dioxygen was found to bind in an η^1 fashion (end-on). In general Ru-O bond lengths increased by an amount that falls between 0.01 and 0.40 Å, with the exception of complex **14** (POR) which increased by 0.73 Å. All complexes surveyed showed a contraction of the O-O bond between 0.07-0.17 Å. The O-O bond lengths for these dioxygen complexes fall between 1.22-1.32 Å, making the character of the O_2 somewhere between dioxygen and superoxide (1.21-1.33 Å).[55]

Table 12: Bond lengths for ruthenium dioxygen complexes.

Complex	Formal Charge	Dimer		Dioxygen Complex		Dimer and Dioxygen Ru-O Diff. (Å)	Dimer and Dioxygen O-O Diff. (Å)
		Avg. Ru-O Distance (Å)	O(1)-O(2) Distance (Å)	Ru(1)-O(1) Distance (Å)	O(1)-O(2) Distance (Å)		
14	0	2.01	1.32	2.74	1.22	+0.73	-0.1
15		1.95	1.39	2.08	1.27	+0.13	-0.12
12a		1.92	1.41	2.04/2.23	1.29	+0.12	-0.12
12bH_2O		1.96	1.38	2.36	1.22	+0.40	-0.16
12bNH_3		2.01	1.35	2.29	1.22	+0.28	-0.13
12bPyr		2.01	1.34	2.33	1.22	+0.32	-0.12
13	-2/-1	1.84	1.49	2.04/2.04	1.32	+0.2	-0.17
11b	-2/-1	1.93	1.38	2.32	1.22	+0.39	-0.16

It can be shown that the O-O bond length in the monometallic dioxygen complex correlates to the average Ru-O distance in the LRu-O-O-RuL dimer. For bridged peroxo complexes with longer Ru-O bonds, the resulting O-O bond lengths in the monometallic dioxygen complexes are smaller. This suggests that bridged peroxide complexes with shorter and stronger Ru-O bonds feature a stronger interaction between the metal centers and the bridging dioxygen. Thus, the dissociation of one of the metal centers elicits a larger contraction of the O-O bond for bridged peroxides that exhibit stronger Ru-O bonds.

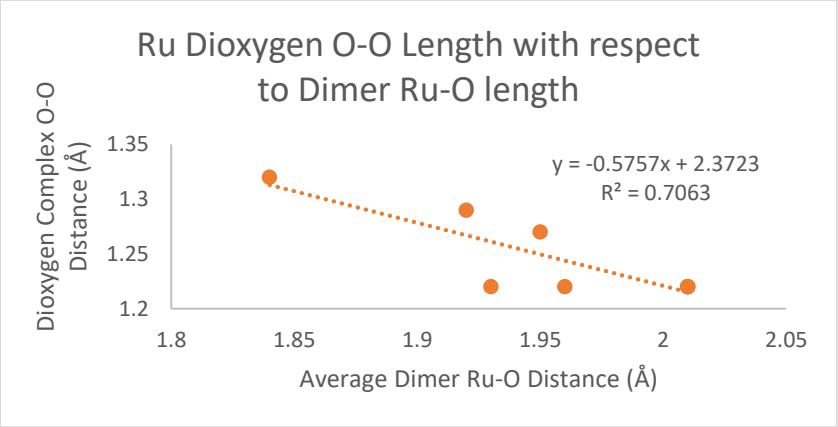

Figure 27: Contraction of O-O bonds in monometallic dioxygen complexes with respect to bimetallic bridged peroxide metal-oxygen bonds.

Comparison of the Ru-O-O bond angles between the dimer and the dioxygen complex show a somewhat modest expansion of the bonding angle, between 0.7° and 13.7°, the exception being complexes **12a** (NTA) and **13** which both exhibit a dramatic reduction in the Ru-O-O angle of 26.2° and 48.5° respectively. Both of these complexes also have the smallest Ru-O-O angles at 80.6° (with the vertex at the O atom closest to Ru) and 71.0° respectively.

Table 13: Bond angles for ruthenium dioxygen complexes.

Complex	Formal Charge	Dimer	Dioxygen Complex	Dimer and Dioxygen Angle Diff.
		RuOO°	RuOO°	
14	0	116.4	122.1	5.7
15		115.6	116.3	0.7
12a		106.8	80.6/64.4	-26.2
12b L = H_2O		116.0	127.5	11.5
12b L = NH_3		116.5	130.2	13.7
12b L = Pyr		116.1	128.2	12.1
13	-1	119.5	71.0/71.0	-48.5
11b	1	118.5	127.2	8.7

The equivalent Ru-O bond lengths and equivalent RuOO angles suggest that the dioxygen group in complex **13** is η^2 (side-on bound). The electronic structure for these side-bound metal dioxygen complexes are unique in that they feature delta-bonding interactions[56], which is explicitly present in the HOMO for complex **13**, further supporting this assignment.

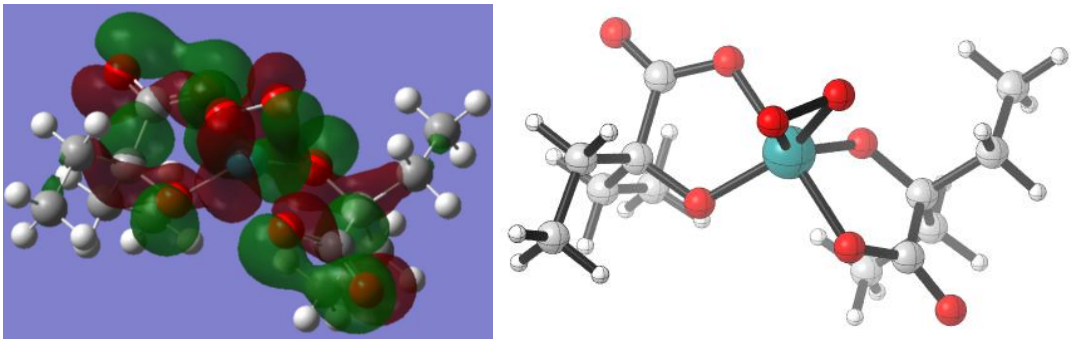

*Figure 28: HOMO (left) and molecular geometry of complex **13** (AHA).*

With that being said, the case of complex **12a** (NTA) is somewhat less clear. Both bond angles (Ru(1)O(1)O(2) and Ru(1)O(2)O(1)) are smaller than those found for end-bound dioxygen complexes, however there is a 16.2° difference between both angles. There is also a 0.19 Å difference between the two Ru-O bonds. If this were a true η^2 complex we should expect both angles and both bond distances to be identical. A number of η^2 and η^1 were reported by Gubelmann[56], showing that on average the O-O bond lengths for η^2 transition metal complexes are longer than those of η^1 complexes (1.44 Å vs. 1.24 Å). While the O-O bond lengths for both complexes **12a** and **13** fall within the standard deviation of the η^1 complexes, they also feature the longest bond lengths of the dioxygen complexes in this study. The HOMO for complex **12a** appears to be pi bonding with respect to the O-O pi antibonding orbital and the Ru d-orbital. The shape of this pi bonding orbital is similar to those seen in other η^2 in that pi antibonding lobes on both O atoms overlap with the metal orbital, rather than the single lobe overlap seen in η^1 complexes. However, a look at HOMO-1 through HOMO-9 show no evidence of any delta bonding interaction, nor do they show evidence of sigma bonding interactions, making a definitive assignment of η^2 or η^1 difficult.

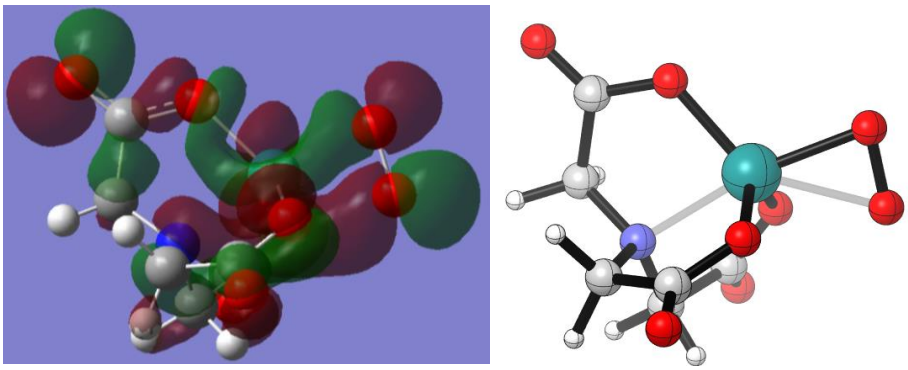

*Figure 29: HOMO and molecular geometry of complex **12a**.*

Part of the ambiguous binding may be due to the difference in structure between complex **13** (AHA) and **12a**. Because complex **13** features two AHA moieties, there is more flexibility, allowing dioxygen to bind in the equatorial area of the molecule. However, the tetradentate NTA ligand forces dioxygen to bind both axially and equatorially in order to achieve an η^2 binding mode. Such a binding would require severe distortion of the octahedral/trigonal bipyramidal geometry. The placement of the dioxygen ligand purely in an axial position on complex **12a** would lead to repulsion between the coordinating carboxylates and dioxygen, destabilizing the structure, leaving it attempting to bridge both axial and equatorial sites.

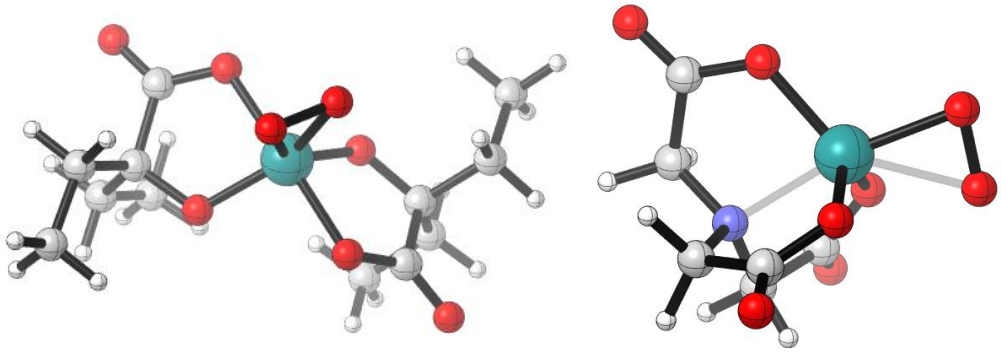

*Figure 30: Molecular structure of complex **13** (left) and **12a** (right).*

It should also be mentioned that of the complexes surveyed in this study, only complexes **12a** and **13** have a doublet ground state. whereas the rest are quartets (complex **15** is also predicted to be a doublet ground state, but its molecular and electronic structure clearly show an η^1 coordination mode). This leaves a sort of pseudo-η^2 geometry.

Only the non-ligated NTA complex **12a** and complex **15** show consistent spin state ground states across all 3 functionals. These two complexes also exhibit a doublet ground state. The remaining 1**2b** complexes exhibit a preference for the quartet spin state with B3LYP and

M06. The OPBE functional for these complexes predicts a very small non-zero preference for the quartet state for **12bNH$_3$** and **12bH$_2$O** and a preference for the doublet state for **12bPyr**. Complex **11b** (BDA(Pyr)) and **14** (POR) also show very small preferences for the doublet or quartet spin state, with the exception of M06 for complex **11b** which shows a clear preference for the quartet state.

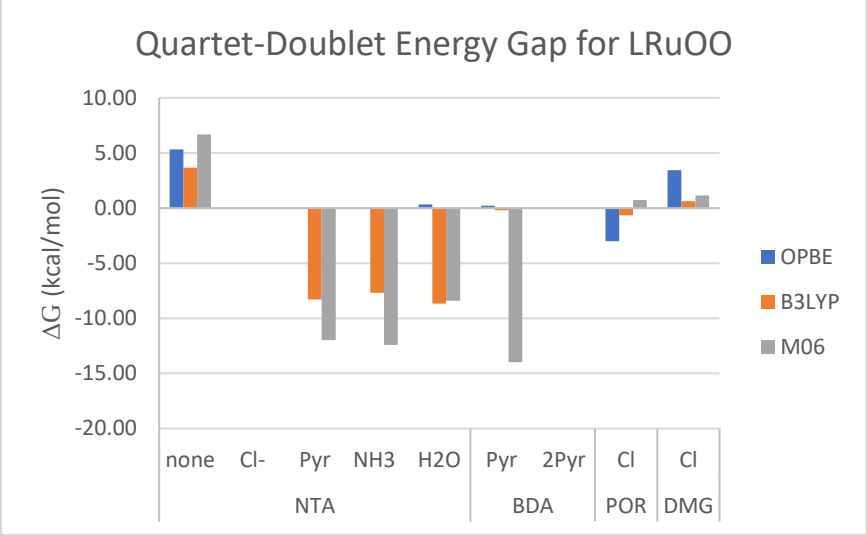

Figure 31: Free energy difference between quartet and doublet spin states for dioxygen complexes. A positive difference indicates a doublet ground state, a negative difference favors a quartet ground state.

The Mulliken spin density provides some insight into the electron spin distribution of the dioxygen moiety in the monometallic complexes. Quartet species all feature spin density on both oxygen atoms somewhere between 0.81 and 1.05. This implies that the dioxygen in the monometallic complex has a triplet structure. This is consistent across all of the quartet species. All of these complexes also contain a significant spin density on the Ru atom, ranging between 0.79 and 0.86, with the total spin density on these three atoms adding up to roughly 3 (S=3/2). The doublet species mirror the triplet structure of dioxygen, containing significant density on

both oxygen atoms. Complexes **15** and **12a** both result in symmetry broken solutions, containing negative spin density on the Ru atoms, although the spin density on the Ru on complex **12a** is only -0.07. This broken symmetry suggests a spin-paired bond for the Ru-O bond. Complex **13** similarly contains a small but positive spin density on Ru.

Table 14: Mulliken spin density for ruthenium dioxygen complexes.

Complex	Formal Charge	Spin Multiplicity	Mulliken Spin Density		
			Ru1	O1	O2
14	0	q	0.79	0.95	1.01
15		d	-0.67	0.54	0.81
12a		d	-0.07	0.48	0.60
12b L = H_2O		q	0.81	0.87	1.05
12b L = NH_3		q	0.86	0.85	1.02
12b L = Pyr		q	0.84	0.86	1.03
13	-1	d	0.10	0.46	0.46
11b	1	q	0.79	0.95	1.01

The electronic structure for the dioxygen complexes show a general agreement with the electronic structure suggested by Gubelmann; η^1 complexes exhibit sigma and pi overlap between the Ru d-orbitals and O-O pi antibonding orbitals (as shown for complex **11b** below), and η^2 complexes show pi (shown for **12a**) and delta overlap between the same orbitals.[56] The HOMOs of the **12b** (NTA) complexes all have a pi antibonding interaction between the carboxylates cis to dioxygen and a Ru d-orbital. These do not show significant density on dioxygen. However, all of the **12b** complexes show a pi bonding interaction between a Ru d-orbital and the pi antibonding orbital of dioxygen at slightly lower orbital energies (NH_3|HOMO-2, Pyr|HOMO-3, H_2O|HOMO-3). This is also the case for the HOMO of complex **15** (DMG) and **11b** (BDA). Complex **14** (POR) contains almost no electron density on dioxygen, instead containing pi antibonding interactions between Ru and the porphyrin, and in the Ru-Cl bond. The

HOMO for **12a** (NTA) has a somewhat anomalous HOMO, in that the bond lengths clearly show an η^1 coordination mode, but the HOMO shows a pi bonding interaction with the pi antibonding orbital overlapping with the Ru d-orbital in an η^2 fashion. The HOMOs for **11b**, **12a**, **14**, and **15** all contain bonding interactions between Ru and O_2, but antibonding interactions in the O-O bond. This suggests that oxidation of these dioxygen complexes may hasten the breaking of the Ru-O bond, helping to drive the following oxygen evolution step, much in the same way it occurs in the cerium-driven mechanism.

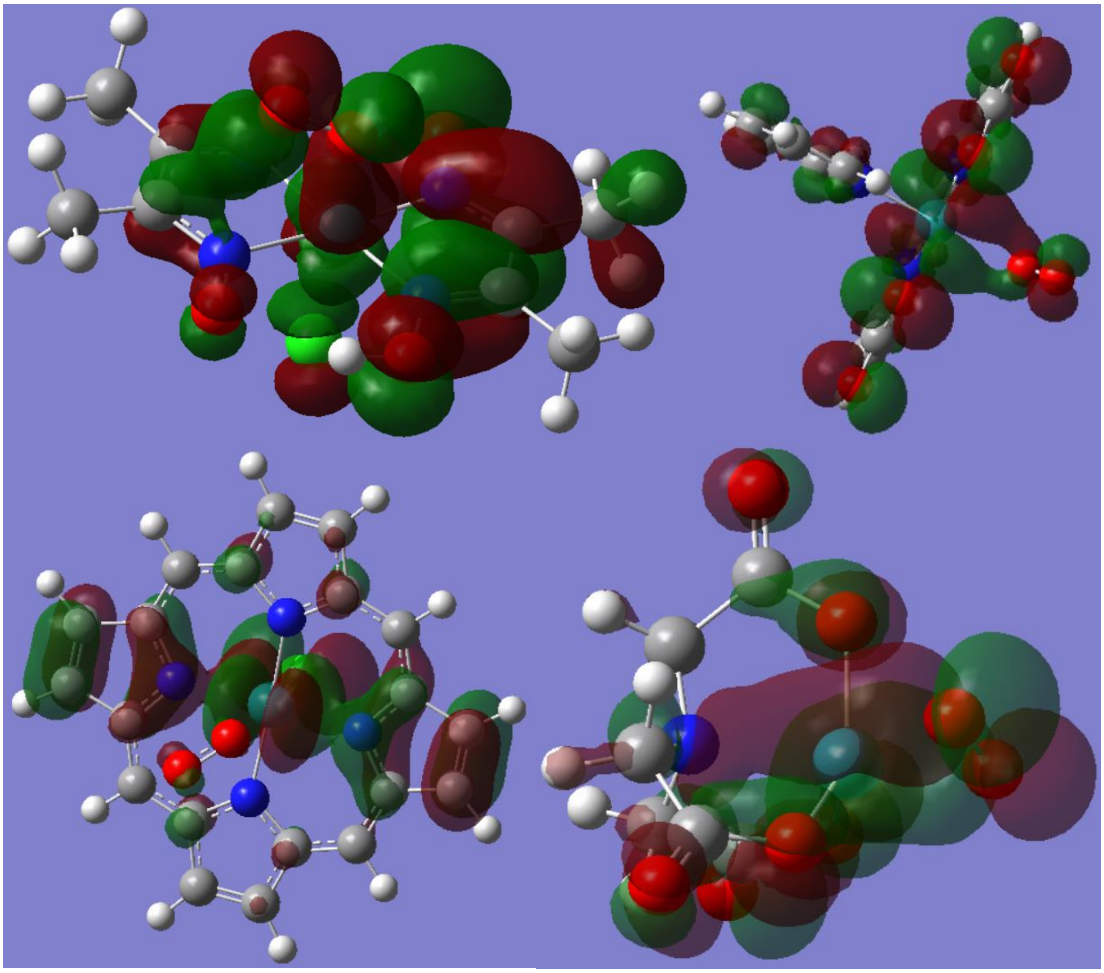

*Figure 32: HOMOs for complexes **15** (top left), **11b** (top right), **14** (bottom left), **12a** (bottom right).*

In fact, the LUMO for complex **12a** shows a delta bonding interaction between the O-O pi antibonding orbital and the Ru d-orbital, exhibiting more η^2 character. With the exception of complex **13** which has delta antibonding character, all of the other LUMOs are sigma bonding with respect to the Ru d-orbital and O-O pi antibonding orbital.

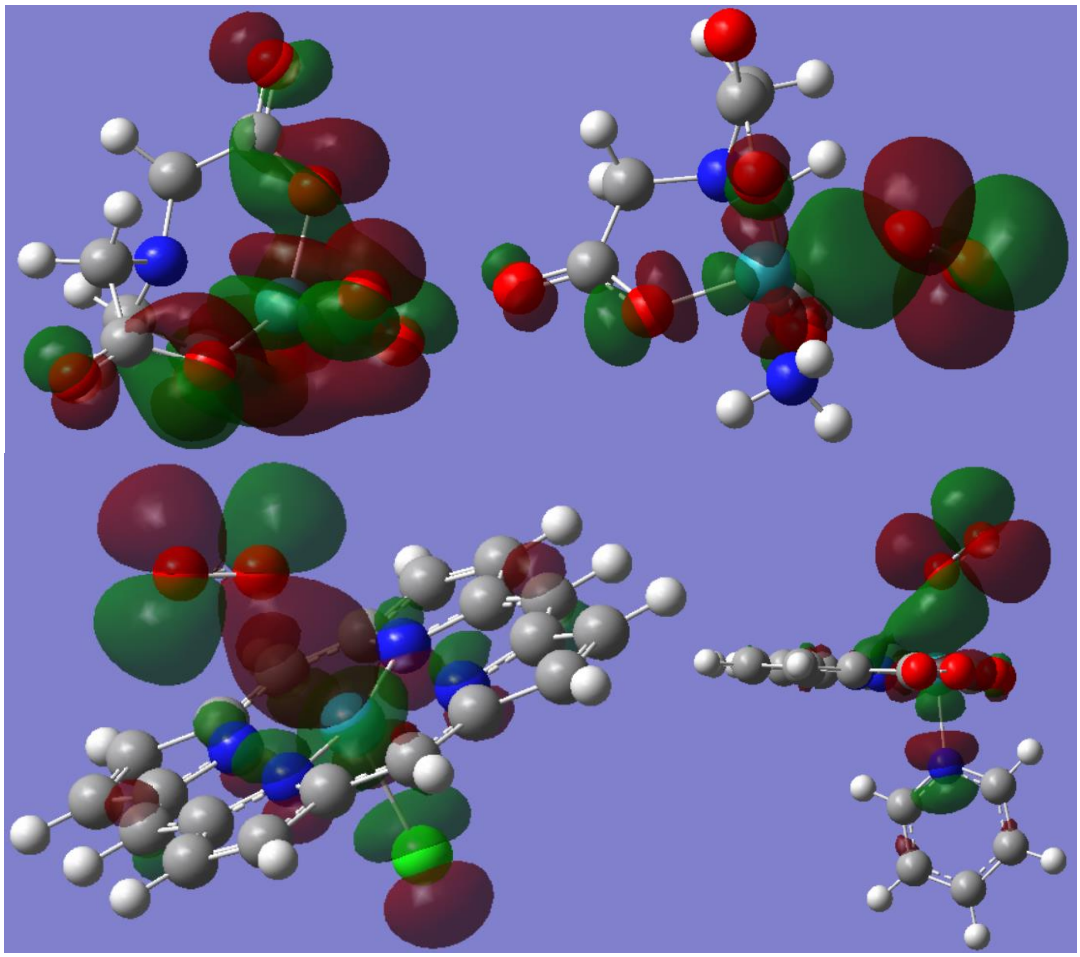

*Figure 33: LUMOs for complexes **12a** (top left), **12bNH₃** (top right), **14** (bottom left), and **11b** (bottom right).*

In general, there is agreement between all three functionals on the spontaneity of the metal dissociation reaction, with the reaction for complex **14** being the exception. The free energies for this reaction are very small, ranging from -3.0 to 0.8 kcal/mol (OPBE and M06 respectively). The small magnitude of the free energies give no clear guidance on which

functional is ‘correct’, although it does suggest that after the formation of the O-O bond, one of the Ru(POR) moieties is bound by a very weak Ru-O bond. Quantitatively, the different functionals can vary by up to 19.1 kcal/mol, with M06 predicting a more positive and less negative free energy, when compared with B3LYP. M06 in general also predicts a more unfavorable free energy than OPBE with the exception of complex **12a**.

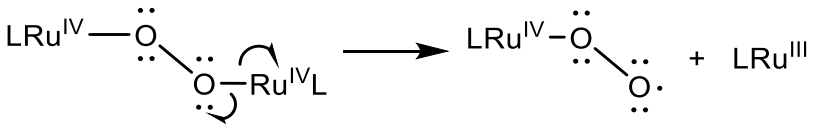

Figure 34: Metal dissociation reaction.

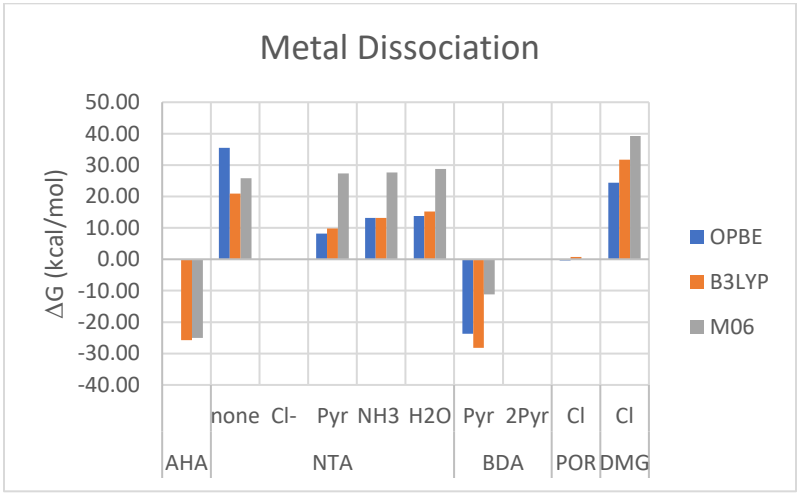

Figure 35: Free energy for the dissociation of LRu from $(LRuO)_2$ species.

With the exception of the Por system (**14)** the neutral complexes exhibit a modest to large thermodynamic uphill climb, ranging from 9.9 kcal/mol (**12bPyr**) to 31.7 kcal/mol (**15**) for the metal dissociation reaction. However, for charged complexes such as complex **12a** (AHA) and **11b** (BDA), the free energies are fairly exoergic (-25.7 and -28.1 kcal/mol respectively). This suggests that there may be some energetic relief in terms of charge stabilization.

Table 15: Free energies for metal dissociation.

Complex	Formal Charge	ΔG (kcal/mol)		
		OPBE	B3LYP	M06
14	0	-0.33	0.8	x
15		24.4	31.7	39.2
12a		35.5	20.9	25.8
12b L = H_2O		13.1	15.2	28.8
12b L = NH_3		13.8	13.2	27.6
12b L = Pyr		8.23	9.9	27.4
13	-1	~	-25.7	-25.1
11a	1	-23.8	-28.1	-11.2

In terms of solvation, there is a clear effect on the metal dissociation free energy. On average, in water the metal dissociation free energy decreases by 15.1 kcal/mol. This effect can be rationalized by the same mechanism that drives up the energetic cost of the coupling step. The average solvation free energy for the coupled product is -30.9 kcal/mol. The combined solvation free energy for both the dioxygen species and the reduced ruthenium complex is -49.1 kcal/mol (-21.4 and -27.8 kcal/mol respectively). The dioxygen complex and reduced ruthenium complex, much like the ruthenium oxo complex, experience a much greater stabilization from solvation than the bridged peroxide, contributing to the more favorable metal dissociation free energy.

Table 16: Solvation data for metal dissociation reaction with B3LYP.

Complex	ΔG_{solv} $(LRuO)_2$	ΔG_{solv} LRuOO	ΔG_{solv} LRu	$\Delta G_{metal\ diss.}$ (gas)	$\Delta G_{metal\ diss.}$ (H_2O)
7b L = Pyr	-32.2	-19.3	-25.7	9.9	-3.0
7b L = NH_3	-35.6	-22.3	-28.5	13.2	-2.0
7b L = H_2O	-34.3	-22.5	-29.1	15.2	-2.1

Reduced Ruthenium Complexes and O_2 Evolution

The ground state spin state for the majority of the reduced ruthenium complexes is predicted to be a doublet with complex **18** (AHA) predicted to be a quartet. All functionals qualitatively agree on the assignment of the spin state, although it should be noted that ground states for complexes **18** and **16a** (BDA) could not be optimized utilizing OPBE. Quantitatively there is fairly good agreement between the three functionals as well. Generally speaking, M06 tends to show a stabilization of the higher spin state (less positive, more negative) with a maximum difference of 13.7 kcal/mol.

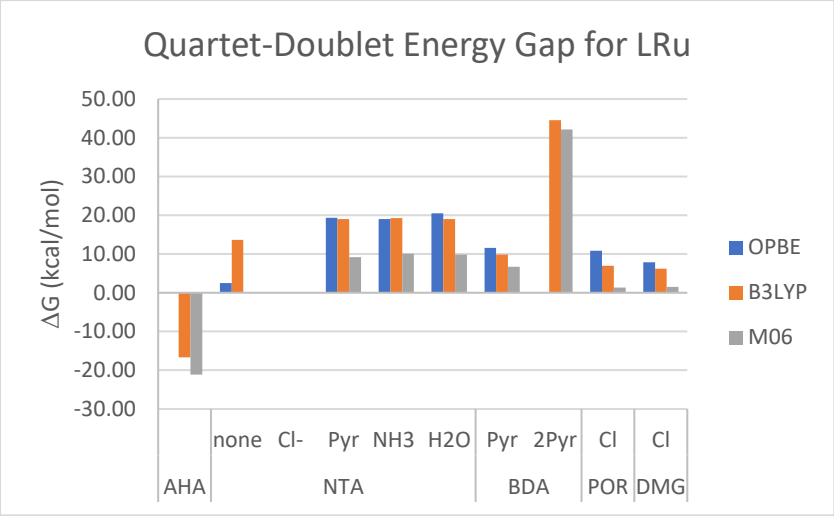

Figure 36: Free energy difference between quartet and doublet spin states for reduced ruthenium complexes. A positive difference indicates a doublet ground state, a negative difference gives a quartet ground state.

The molecular geometries of the reduced species vary considerably, likely due to the low coordination number of the central ruthenium atom. With that being said, many of the reduced species retain a similar geometry around the metal center in relation to the related oxo, bridged peroxo, and dioxygen intermediates (octahedral/trigonal bipyramidal) minus the reactive oxygen. The exception to this trend is complex **18** which transforms from a trigonal bipyramidal geometry into a square planar geometry. Such a geometry is highly unusual for a d^5 complex

such as Ru(III). Typical square planar complexes have a d^8 electron configuration (Ni, Pd, Pt), however there is some precedence for square planar Ru (II)[57,58] and Ru (IV)[59] complexes.

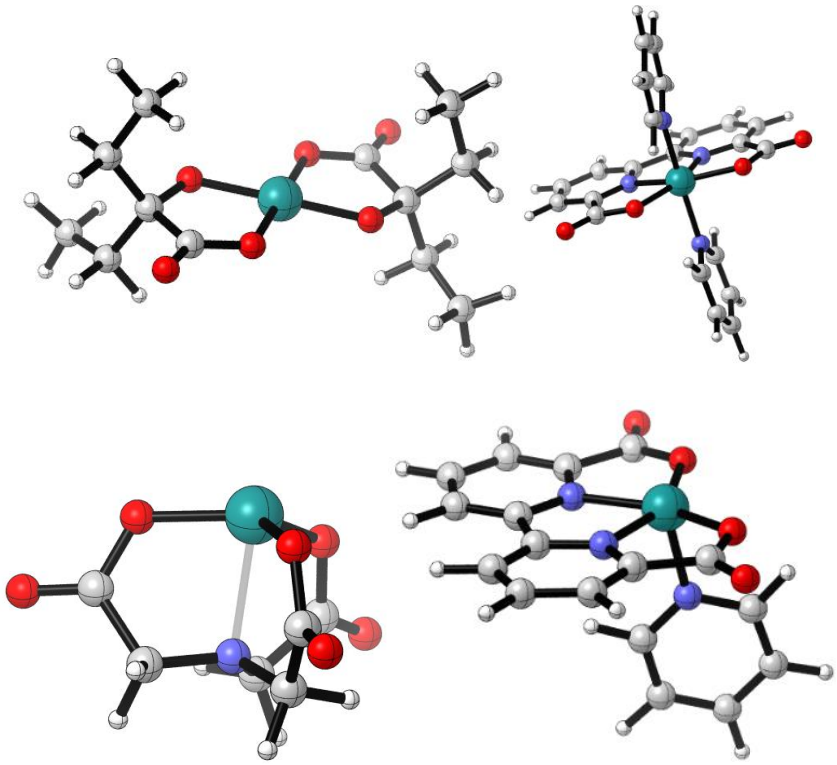

*Figure 37: Molecular geometries for complex **18** (top left|AHA), **16a** (top right|BDA), **17a** (bottom left|NTA), and **16b** (bottom right|BDA).*

The Mulliken spin density on the reduced ruthenium complexes is primarily located on the ruthenium atoms for each of the complexes. The HOMO for all of the reduced ruthenium species contain pi antibonding character between the metal d orbital and ligand orbitals, although in the case of complex **19** this also includes sigma antibonding character with respect to the Ru-Cl bond. Complex **20** contains very little electron density on the ruthenium atom in the HOMO, instead being localized around the DMG pi bonds. The LUMOs for these complexes are also pi antibonding orbitals, albeit in a different direction (d_{xz} vs. d_{yz}).

Table 17: Mulliken spin density for reduced ruthenium complexes.

Complex	Formal Charge	Spin Multiplicity	Ru Mulliken Spin Density
19	0	q	2.28
20		d	0.63
17a		d	0.83
17b L = H_2O		d	0.77
17b L = NH_3		d	0.80
17b L = Pyr		d	0.78
18	-1	q	2.36
16a	1	d	0.77
16b		d	0.76

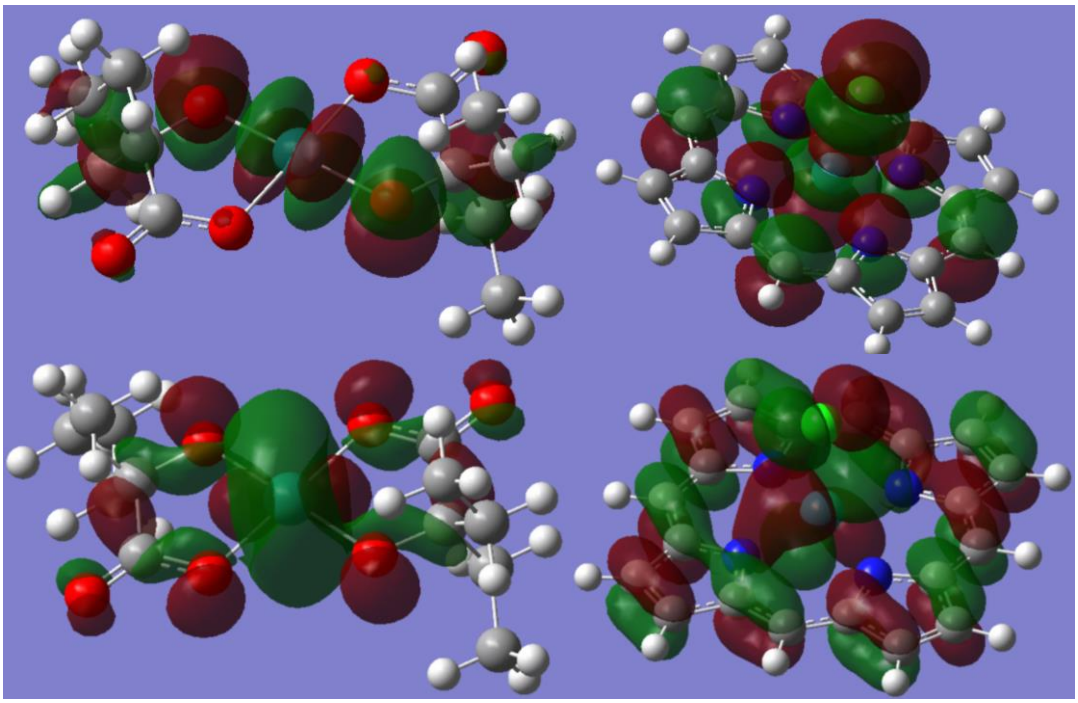

*Figure 38: HOMO/LUMOs (top/bottom) for complex **18** (left|AHA) and **19** (right|POR).*

There is considerable variation between the three functionals for the oxygen evolution reaction. Only for complex **17a** do all three functionals make the same prediction for the spontaneity of the reaction, although there is quantitatively a huge variation between each functional on the magnitude of 10.5 kcal/mol between OPBE and M06, and 23.1 kcal/mol

between OPBE and B3LYP. For the **17b** (NTA) complexes and **19** (POR) there is comparatively better agreement with respect to OBPE and B3LYP. Both functionals predict the O_2 evolution reaction to be exoergic, with a maximum difference between the two functionals of 7.1 kcal/mol. The free energy of oxygen evolution for the **17b** complexes and most of the others complexes (**16a** excluded) with respect to M06 is fairly small, ranging from -7.4 kcal/mol to 6.3 kcal/mol, with the **17b** complexes ranging from -0.4 kcal/mol to 0.1 kcal/mol. The small energies associated with the **17b** make any determination of endergonic vs. exergonic difficult. The free energy of oxygen evolution was unable to be determined with OPBE for complexes **18** and **16a**, and as discussed above, attempts to optimize a dioxygen complex utilizing the BDA backbone and two axial pyridines were unsuccessful, inevitably leading to dioxygen unbound and far removed from the ruthenium center. The free energy here, unlike the other complexes, represents the evolution of oxygen directly from the bridged peroxo species. For both complex **18** and **16a**, B3LYP and M06 predict fairly different energies: 10.8 vs. -7.4 for **18**, and -55.0 vs. -31.2 for **16a**. The large discrepancies between the functionals may point to the difference in the ability of these functionals to handle non-covalent interactions, with respect to the long Ru-O bond lengths in the dioxygen complexes.

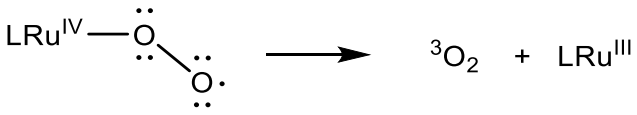

Figure 39: Oxygen evolution reaction equation.

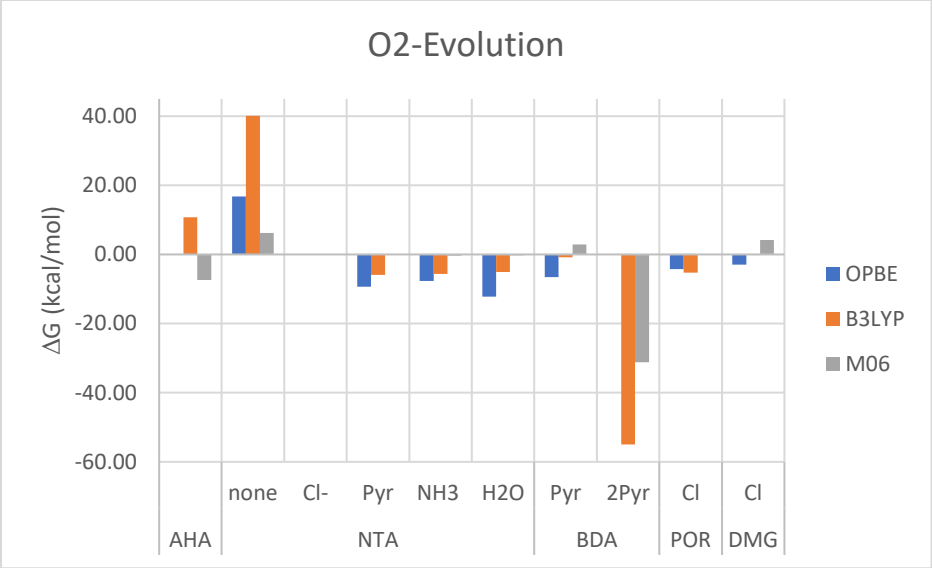

Figure 40: Free energy of oxygen evolution from LRuOO.

With respect to B3LYP, complexes **17a** (NTA) and **16a** show the largest free energies of oxygen evolution, albeit with different signs. The coordination numbers for the dioxygen complexes and reduced metal complexes represent extremes in the set of complexes discussed here. Oxygen evolution from complex **17a** causes the ruthenium to transition from a coordination number of 5 to 4. For ruthenium complexes, a coordination number of 4 is fairly rare. Such complexes have open sites primed for functionalization, and have been utilized as reactive intermediates in the Grubbs olefin metathesis, being the active state of the Grubbs catalyst.[60,61] The 4-coordinate Grubbs catalysts have a trigonal pyramidal geometry, similar to the geometry of the reduced ruthenium complex **17a**. To this end, the large penalty for forming the 4-coordinate complex **17a** from the 5-coordinate **12a** may represent the reactivity and the potential for the reduced complex to act as a reducing agent. It should also be mentioned that both complexes **17a** and **18** feature η^2 coordination of oxygen. These are the only two complexes in the series that feature this sort of binding mode, thus it may also be that it is simply more

demanding to evolve η^2-bound O_2, on account of the 2 Ru-O bonds that must be cleaved. With respect to complex **17a**, it is also possible that the low coordination is responsible for this binding mode, since the **17b** complexes do not feature this mode. The effect of coordination number and O_2 binding are not necessarily mutually exclusive in this scenario.

Table 18: Free energies of oxygen evolution.

Complex	Formal Charge	ΔG (kcal/mol)		
		OPBE	B3LYP	M06
19	0	-4.3	-5.2	
20		-2.9	-0.2	4.2
17a		16.8	40.1	6.3
17bH_2O		-12.2	-5.1	-0.2
17bNH_3		-7.7	-5.6	-0.4
17bPyr		-9.3	-5.9	0.1
18	-1	~	10.8	-7.4
16a	1	~	-55.0	-31.2
16b		-6.6	-0.8	2.9

A somewhat opposite effect occurs for the $BDA(Py)_2Ru^+$ set of complexes. Transforming from an initially 7-coordinate species into a 6-coordinate one. The introduction of the oxo and dioxygen groups in the equatorial plane causes severe distortion of the octahedral geometry and causes steric repulsion. The elimination of dioxygen should then be favorable based on the easing of distortion and repulsion in the equatorial plane.

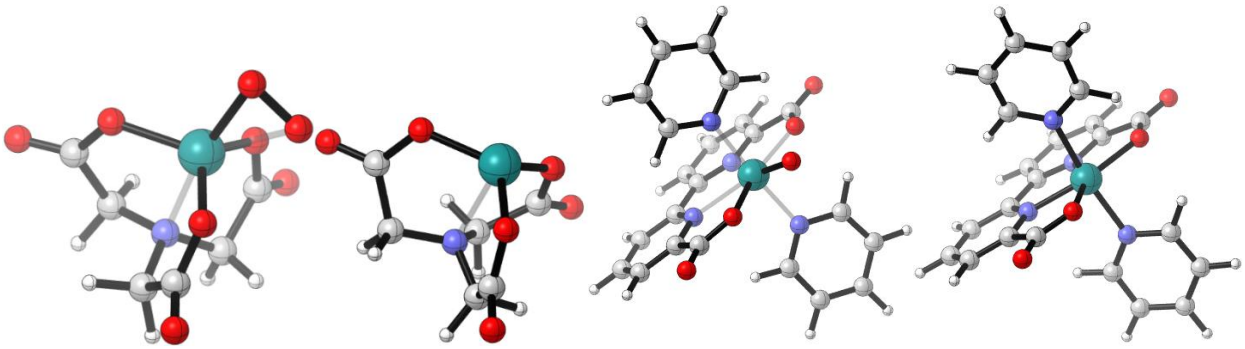

*Figure 41: Molecular geometries for complexes **12a** (far left), **17a** (middle left), **1a** (middle right), and **16a** (far right).*

Like the coupling and metal dissociation step, the difference in solvent free energy in the reactants and products can be seen contributing to the difference of the free energy of oxygen evolution in the gas and aqueous phase. The more favorable solvation free energy of the reduced complex in comparison to the dioxygen complex brings the free energy of oxygen evolution down. Work done by Khan, et al. presented the dioxygen affinities for a number ruthenium (III) Schiff base complexes.[62] The reverse of these affinities is precisely the oxygen evolution from a ruthenium (IV) dioxygen complex. Khan reports an average oxygen evolution free energy in DMF of 3.3 ± 0.4 kcal/mol.[62] In both the aqueous and gas phase (DMF is somewhere between these two), the free energy of oxygen evolution is even more favorable.

Table 19: Solvation data for O_2 evolution step.

Complex	ΔG_{solv} LRuOO	ΔG_{solv} LRu	$\Delta G_{O2\ evol.}$ (gas)	$\Delta G_{O2\ evol.}$ (H_2O)
7b L = Pyr	-19.3	-25.7	-5.7	-12.1
7b L = NH_3	-22.3	-28.5	-5.9	-12.2
7b L = H_2O	-22.5	-29.1	-5.1	-11.7

Summary of Computational Results

The oxygen evolution pathway for the different complexes reveals a number of different trends. For the ligated NTA complexes (NTARuPyr, NTARuH_2O, NTARuNH_3), the pyridine complex has the greatest activation barrier for the coupling step at a height of 16.2 kcal/mol, followed by the ammonia complex at 10.4 kcal/mol. The trend for the thermodynamic free energy of coupling is similar, in the order pyridine > NH_3 > H_2O. A transition state was not found for the coupling step of the (NTA)RuH_2O complex, but if it follows the aforementioned trend, then the activation free energy is likely similar in magnitude to the NH_3 and pyridine complexes. Without transition states for the metal dissociation and oxygen evolution steps it is

unclear whether the coupling step is rate limiting. However, the modest uphill thermodynamics in the metal dissociation step suggest that any barrier in this step or in the oxygen evolution step is not large. The entire reaction for these three complexes is nearly thermoneutral, indicating that they are well suited for the oxygen evolution reaction.

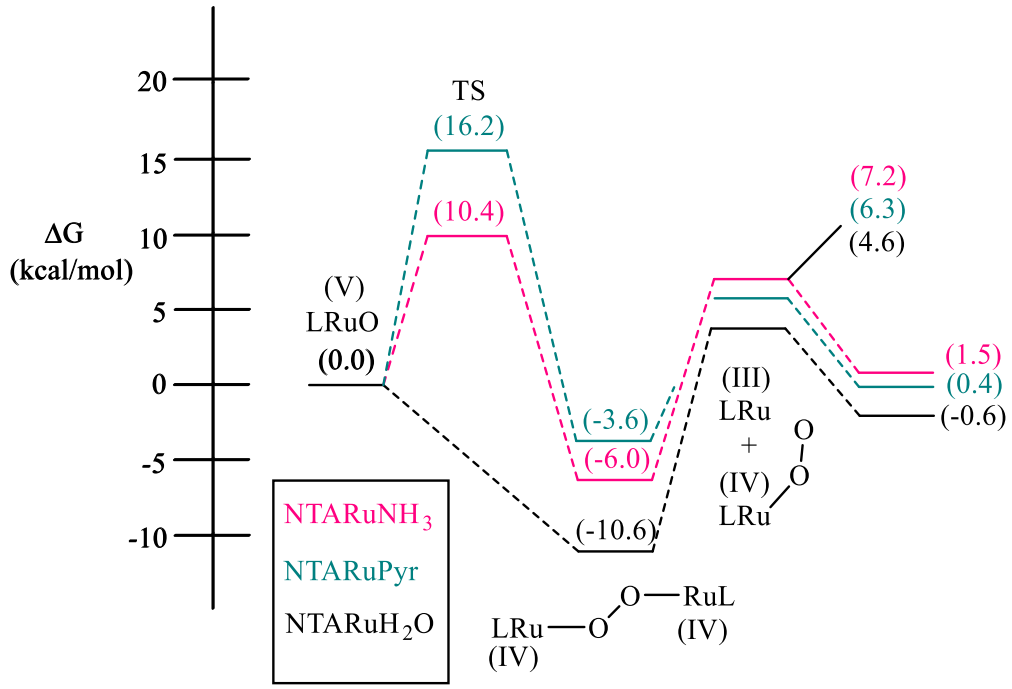

Figure 42: Reaction coordinate for OER of NTARuO(L) complexes.

The activation energies of coupling for the ligated NTA complexes are similar to that found for the non-ligated NTA complex. All of the NTA complexes (chloride complex aside) feature a modest activation barrier coupled with an exoergic coupling free energy. This is then followed by a modestly endoergic metal dissociation step. The similarities end at the oxygen evolution step, where a fairly uphill step brings the thermodynamics up to a net of 54.4 kcal/mol for the non-ligated NTA complex. This reveals that the presence of another ligand in the coordination sphere may be necessary for favorable thermodynamics. The oxygen evolution step in the reaction has the non-ligated (NTA)Ru complex transition from a coordination number of 5

to 4, while the ligated species goes from 6 to 5. This indicates that particularly low-coordinate species may face a significant barrier in evolving oxygen to the formation of low-coordinate products. In this same vein, the 7 coordinate $(BDA)RuO(Pyr)_2^+$ complex features the most favorable thermodynamics with a net free energy of -42.9 kcal/mol, exhibiting a large driving force for this reaction. While a ground state was unable to be optimized for the $(BDA)Ru(Pyr)_2(O_2)^+$ complex, the oxygen evolution step from the bridged peroxide shows a transition from a coordination number of 7 to 6. While the free energy for the coupling step of the $(BDA)RuO(Pyr)_2^+$ is uphill, it is only uphill by 15.1 kcal/mol, which is fairly small. To this end the thermodynamics for the coupling and metal dissociation steps are all fairly small whether uphill or downhill. The effect of coordination number appears to mainly be expressed in the oxygen evolution step. To this end, in the design of complexes for oxygen evolution reactions, a crowded geometry can provide a good driving force, while a complex that is under-coordinated will have significant barriers. This leaves the octahedral complexes that transitions from 6 to 5, in a somewhat sweet spot, not overly favorable, but not prohibitively unfavorable.

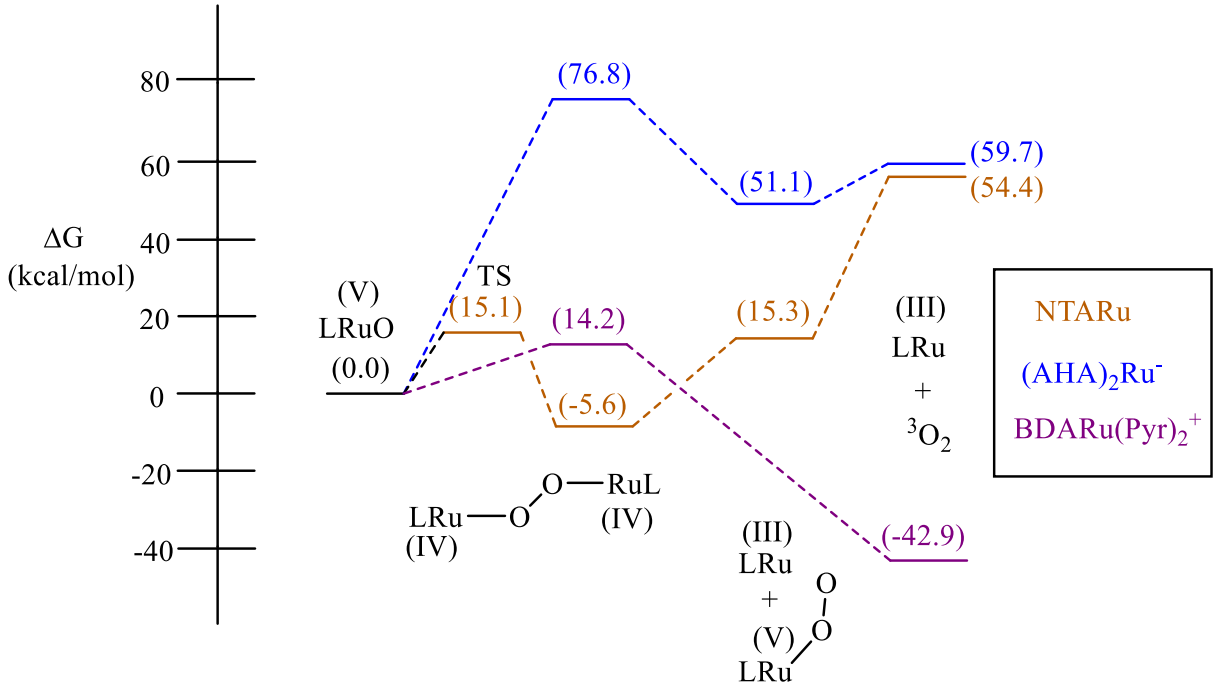

Figure 43: Reaction coordinate for NTARuO, $(AHA)_2RuO^-$, and $BDARu(Pyr)_2O^+$.

This same aspect is seen when comparing the mono- and bis-pyridine BDA complexes. The coupling free energy is similar (20.4 vs 14.2), but when looking at the net free energy the monopyridine complex is only -8.5 kcal/mol, considerably smaller than that seen for the bis pyridine complex (-42.9 kcal/mol). Once again, the effect of coordination is indicating that the crowded geometry yields a stronger driving force for oxygen evolution than the octahedral complexes.

The neutral (Por)RuCl complex (5/6 coordinate) features a relatively thermoneutral oxygen evolution reaction with fairly small energetic requirements for each individual step, in line with the other 5/6 coordinate species. As somewhat of an outlier, the $(DMG)_2RuCl$ complex has a less favorable pathway to oxygen evolution than the other 5/6 coordinate complexes. The reason for this is not clear. The unfavorable step for this complex is the metal dissociation. The free energy for the oxygen evolution step is also fairly small. This suggests that the dissociation

of the opposite ruthenium complex destabilizes the dioxygen that's bound to the remaining ruthenium species. The small free energy for the oxygen evolution step tells us that dioxygen is weakly bound to the (DMG)RuCl complex, thus the presence of both ruthenium centers is necessary to 'trap' and bind dioxygen.

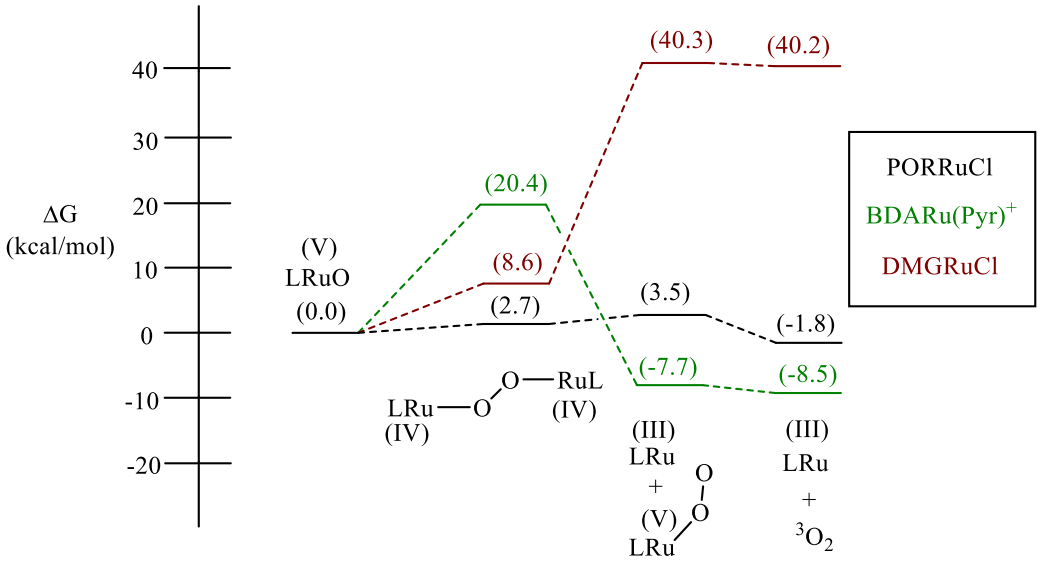

Figure 44: Reaction coordinate for BDARu(Pyr)O$^+$, PORRuCl(O), and DMGRuCl(O).

The effect of solvation on the NTARuO(L) reaction profiles presents a clear change. In the gas phase, the global minimum for each complex is the bridged peroxide, with modest activation energies in the range of 10-16 kcal/mol. In water, these activation barriers are raised to be in the range of 20-23 kcal/mol. The free energy of coupling in water is also raised by 8-9 kcal/mol with respect to the gas phase free energy, making the coupling energy endoergic for the NTARuNH$_3$(O) and NTARuPyr(O) complexes. This is caused by the relatively poor solvation of the bridged peroxide in comparison to the ruthenium oxo complexes. This exact same effect contributes to the lowering of the metal dissociation free energy in water by roughly 15 kcal/mol. This lowering flips the free energy from endoergic to exoergic, making the metal dissociation from the bridged peroxide downhill rather than uphill. This, coupled with the more downhill

oxygen evolution step brings the total free energy for the OER down in the range of -9 to -16 kcal/mol. This in contrast with the gas phase free energy for the OER which is roughly thermoneutral. While the increased activation energy for the coupling step will certainly slow down the overall rate of reaction, the reaction will proceed forward and evolve oxygen, producing the reduced ruthenium complex as the main product.

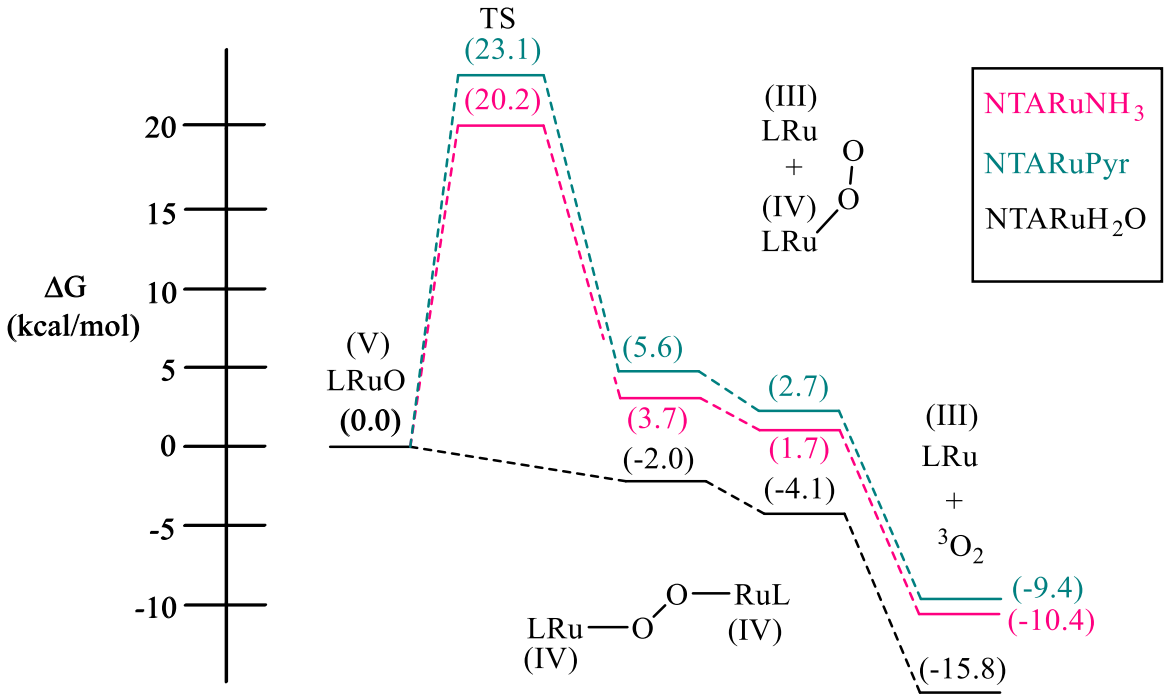

Figure 45: Reaction coordinate for OER of NTARuO(L) complexes in water.

b. Experimental Results

In addition to the computational work presented above, experimental work was undertaken to synthesize the complexes studied and perform the oxygen evolution reaction with them. Of the complexes surveyed, oxo complex **3** (AHA) was synthesized and characterized. Subsequent experiments were done to provide a preliminary indication of whether this complex would be able to undergo the oxygen-evolution reaction. Several attempts were made to synthesize an NTA bound complex (complex **2**/**17**). The outcomes of these attempts are compiled herein.

*Oxygen Evolution Reaction of Complex **3***

Complex **3** was synthesized using a two-step method: oxidation of Ru(III) chloride with sodium bromate to form tetrapropyl ammonium perruthenate (TPAP), followed by the reduction of the perruthenate (Ru(VII)) by excess 2-ethyl,2-hydroxybutanoic acid (AHA) to form complex **3**.[28,29] Complex **3** was characterized by IR, UV-Vis, ESI-MS, and EPR. The EPR spectrum of the complex yields a g-factor of 1.986, closely matching that reported by Dengel[28,29], confirming the doublet ground state of complex **3**.

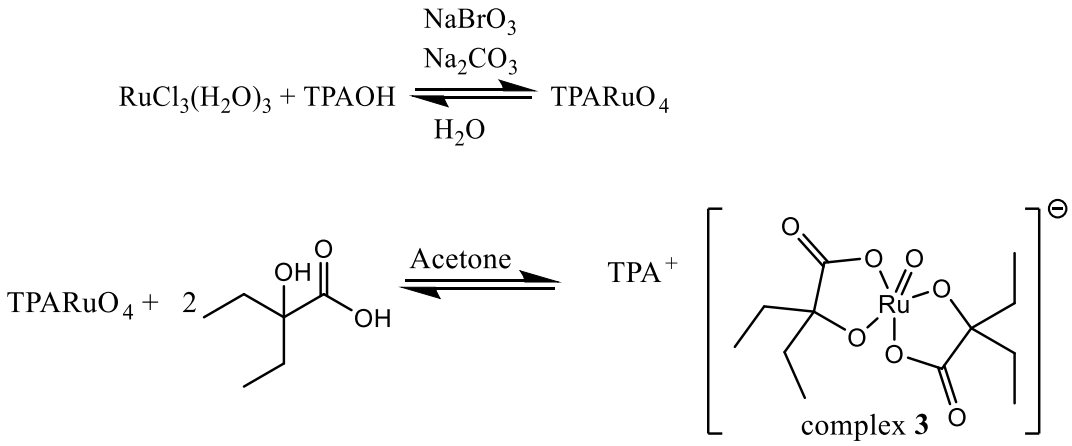

*Figure 46: Synthetic scheme for complex **3**.*

The UV-Vis spectrum for complex **3** obtained in DCM showed three unique absorptions at 328 nm, 394 nm, and 472 nm (λ_1, λ_2, and λ_3 respectively). Wavelengths λ_1 and λ_3 show good agreement with those reported by Dengel[28,29]; however there is a 29 nm difference between the λ_2 reported by Dengel and in this work. Both of these lines were compared to the UV-Vis spectrum predicted by TD-DFT, of which the most intense lines appear at 346, 412, and 509 nm. Plotting the experimental wavelengths vs. the three wavelengths calculated by TD-DFT shows a linear correlation for both complexes, with a slightly better linearity for the wavelengths found by us. However, the difference in the R values is fairly small.

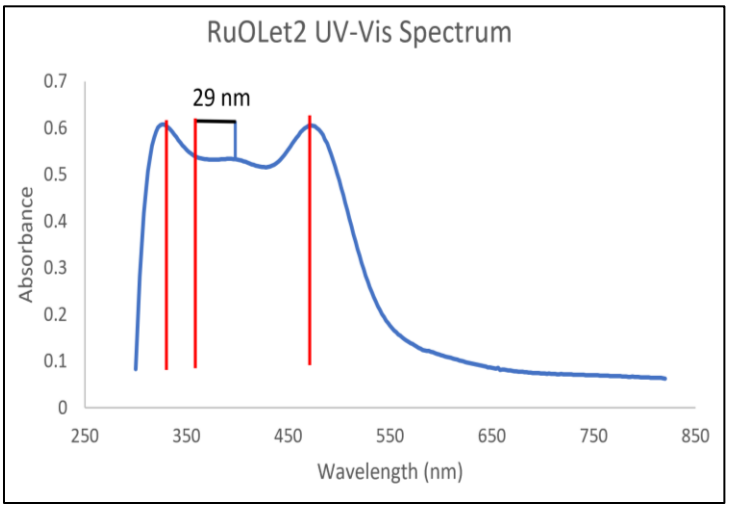

*Figure 47: UV-Vis spectrum of complex **3** in DCM, with the location of the lines reported by Dengel marked by red lines.*

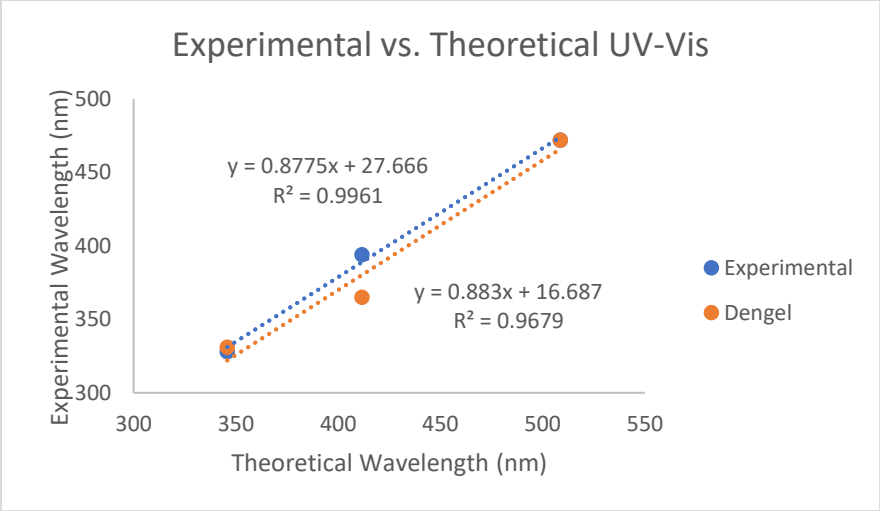

Figure 48: Correlation of experimental wavelengths with theoretical wavelengths.

Looking at the spacing between the different energy levels more clearly shows the difference between our data and Dengel's. The spacing between E_1 and E_3 is relatively constant, with a % error of 2.6% with for the literature data and 0.1% with our data. Both of these agree well with the TD-DFT calculations. The greatest discrepancy is in the location of E_2, and the separations ΔE_{12}, and ΔE_{23}. The error with respect to the literaeture data and the theoretical separations is nearly 4x higher than the data acquired by us. This illustrates that in spite of the discrepancy between our data and Dengel's, our data more closely matches the data generated from TD-DFT.

Table 20: Energy gap data.

	Dengel	**Exp.**	**TD-DFT**	**Dengel Diff.**	**Deng %error**	**Exp. Diff.**	**Exp %error**
ΔE_{12}	8.1	14.6	13.2	5.2	39.2	1.4	10.4
ΔE_{23}	17.8	12.0	13.3	4.5	33.9	1.3	9.6
ΔE_{13}	25.8	26.6	26.5	0.7	2.6	0.1	0.4

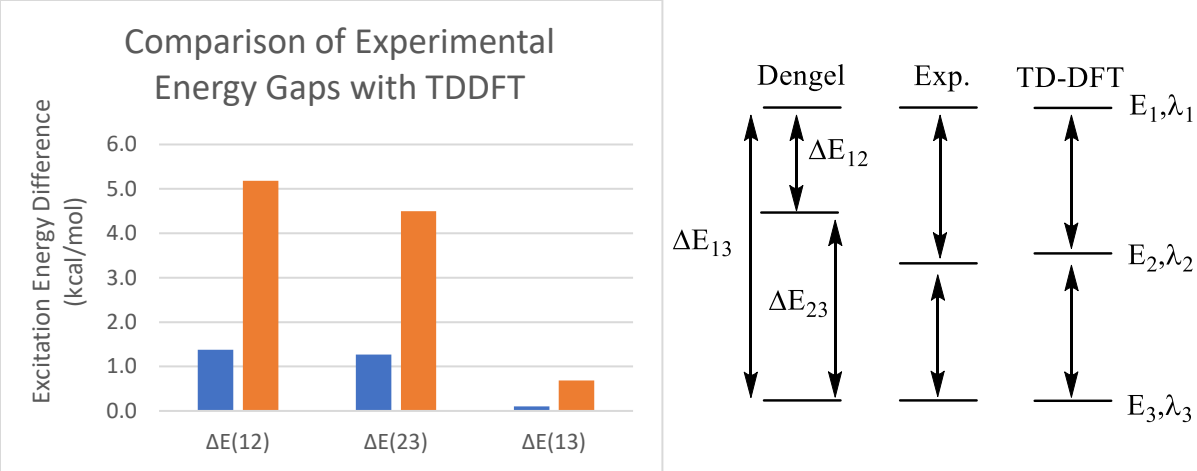

Figure 49: Left: energy level diagram with relative location of excited states. Right: Difference between experimental and theoretical energy gaps.

Preliminary photochemical and thermolysis reactions were performed in DCE to evaluate complex **3**'s ability to undergo the oxygen evolution reaction. Both reactions were tracked over different periods of time by UV-Vis spectroscopy. For the thermolysis reaction UV-Vis spectra were obtained at two different concentrations, in order to resolve the absorptions in the near-UV/UV region. The spectra below show one of the characteristic bands for complex **3** at 464 nm for t = 0 hrs. The subsequent spectra at 20 hrs. and 24 hrs. show that thermolysis of complex **3** shrinks this band at 464 nm, while some broadening/peak growth is occurring in the near-UV/UV region. Because the strength of the absorption at 210 nm saturates the detector, it was necessary to dilute the thermolysis samples further, in order to determine if any changes were occurring in the UV region. The spectra of these diluted solutions do show an increase in the absorption at 232 nm, as well as a new peak emerging as a shoulder at 270 nm. These changes are indicative of a chemical transformation occurring. In addition, the small change between t = 20 hrs. and 24 hrs. indicate that whatever reaction is occurring is finished sometime before 20 hrs.

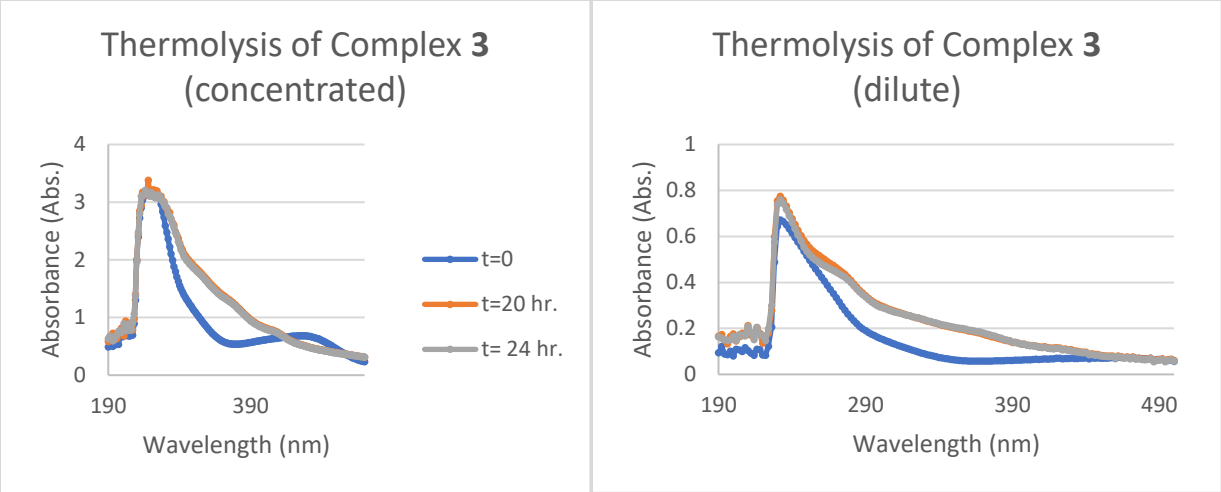

*Figure 50: UV-Vis spectra at 0 hrs. (blue), 20 hrs. (orange), and 24 hrs. (gray) for thermolysis of complex **3**.*

Neither negative or positive ion ESI-MS nor GC/EI-MS showed evidence of any ruthenium containing products of this process. GC/EI-MS did pick up a large array of products that did not appear to have any direct relation to the oxygen-evolution reaction. However, an m/z of 86 can be identified which corresponds to 3-pentanone, a possible decomposition product of the AHA ligand. This decidedly does not show up in the ESI-MS data meaning it could be a result of either the hard ionization method decomposing any ligand leftover from the thermolysis, or an actual decomposition of complex **3** via thermolysis, as shown below. With that being said, EPR analysis on the resulting reaction mixture shows no signal, indicating that no paramagnetic species were present in solution. The apparent mixture of products obtained from the thermolysis reaction indicates that this ligand type may not be suitable as an OER catalyst.

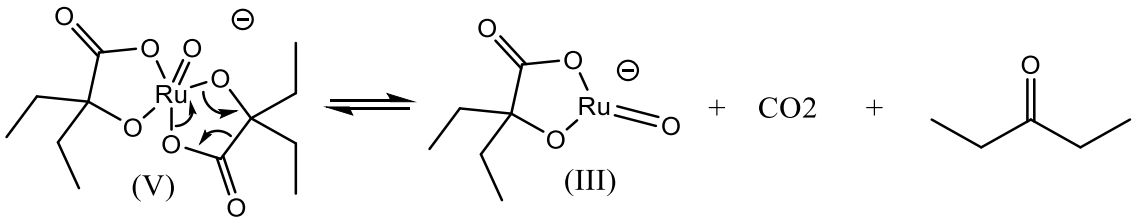

Figure 51: Potential decomposition scheme for $(AHA)_2RuO^-$.

Photolysis experiments were done separately at two different concentrations, in order to study changes in both the visible and the UV region. The concentrated run shows an initial jump in the absorbance at 458 nm, followed by steep decline and then a more gradual increase. The shape of the curve suggests the rapid formation of some intermediate that is then consumed. This same behavior can be seen at the local minimum at 370 nm, which changes in much the same manner as the peak at 458 nm does, suggesting that the changes may be related.

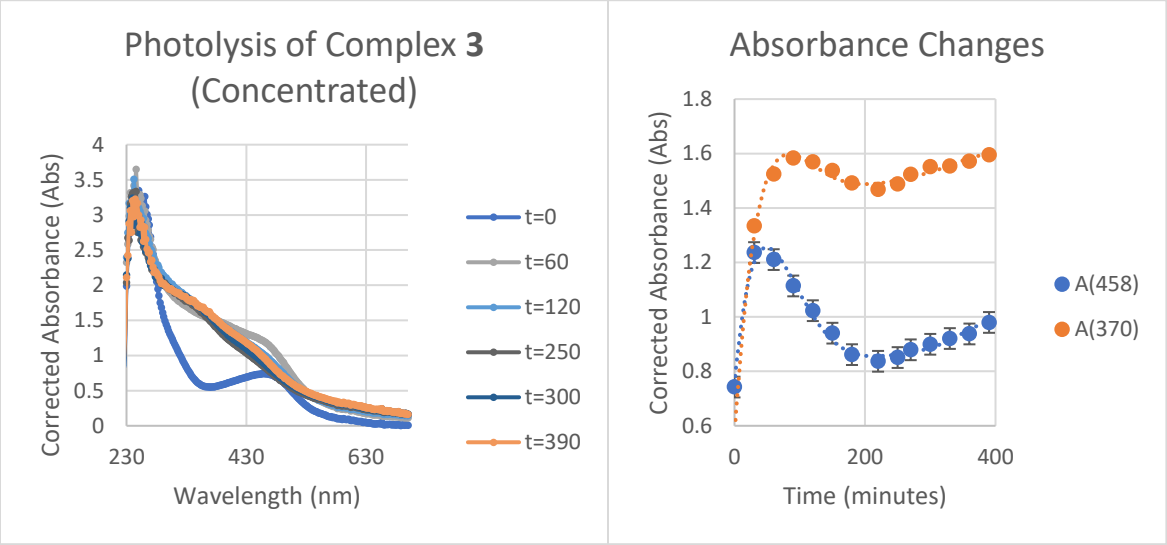

*Figure 52: Left, photolysis of a concentrated solution of complex **3** at several time points. Right, absorbance changes at 458 nm (blue) and 370 nm (orange).*

The dilute photolysis allows the behavior of the UV absorption to be better resolved. The peak at 232 nm experiences growth and then becomes fairly static around 150 minutes. The peak

at 448 nm, which matches closely to the peak at 458 nm, experiences a maximum around 120 minutes, then steadily decays. Again, the changes seen in the spectrum clearly indicate a chemical change occurring.

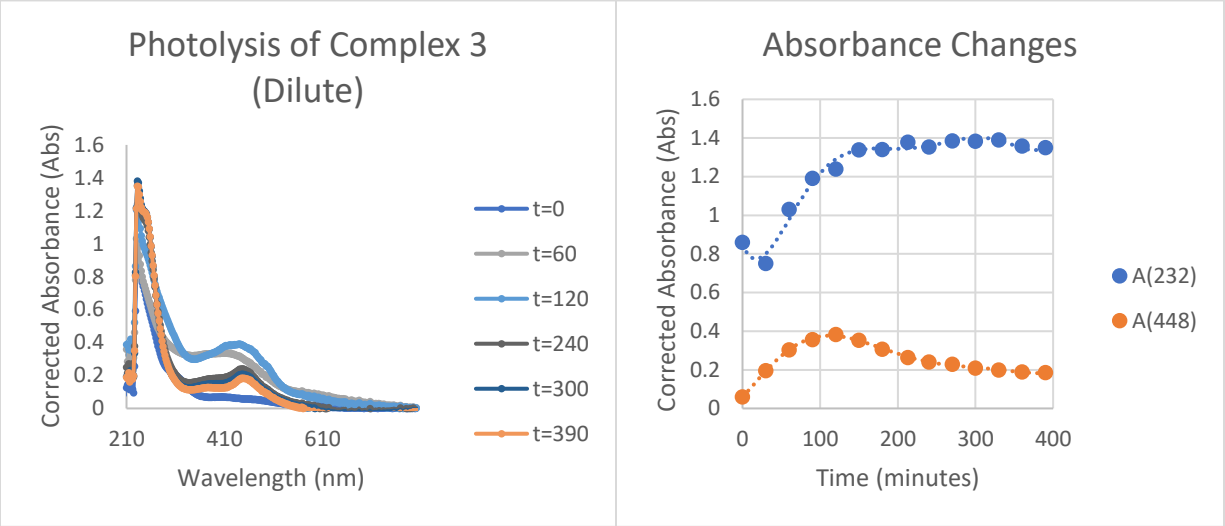

*Figure 53: Left, photolysis of a dilute solution of complex **3** at several time points. Right, absorbance changes at 232 nm (blue) and 448 nm (orange).*

Synthesis of NTARu complexes

In addition to the work done on complex **3**, attempts were also made to synthesize an NTA ligated species (**2a**, **2Cl**, **2Pyr**, **2H$_2$O**). A number of different conditions were used to produce a ligated NTA-ligated Ru complex. The source of ruthenium used in trials 1-11 is $RuCl_3 \bullet 3H_2O$, a relatively cheap source of ruthenium which is in the +3 oxidation state. Its availability, in addition to the facile Ru-Cl bonds should make $RuCl_3$ a good source of ruthenium. $RuCl_3 \bullet 3H_2O$ was combined with either the NTA acid ($NTAH_3$) or trisodium salt (Na_3NTA), in a number of different solvents. Strong and weak bases were used to deprotonate and solubilize the NTA acid. The literature contains only one example of a characterized (NTA)Ru complex, which gives the dianionic $[(NTA)RuCl_2]^{2-}$ complex[63]. This procedure, in

addition to two procedures adapted from electronically similar $(NTA)FeCl_2(PyH)_2$[64,65] and $(NTA)Co(Pyr)(H_2O)$[66] complexes were attempted as well.

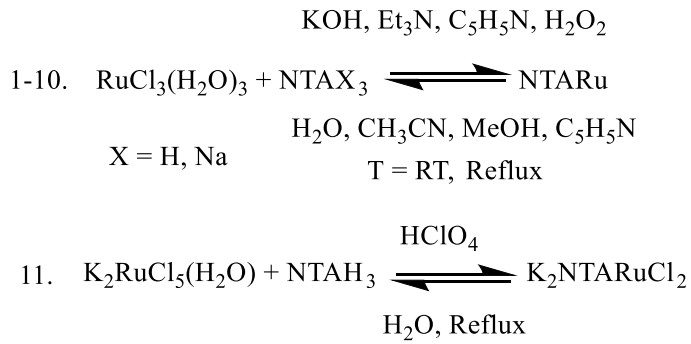

Figure 54: Reaction equations for different NTARu syntheses.

Reaction mixtures from these experiments were analyzed using a combination of IR and ESI (positive and negative) to try to identify the reaction products. To this end, much of the data from IR is qualitative. Its main diagnostic benefit is identifying the presence of, and partially characterizing the state of the NTA ligand. In particular, the precise location of the carbonyl absorption can provide some information on whether it is coordinated. The stretching frequency of the protonated $NTAH_3$ and Na_3NTA are 1734 and 1599 cm^{-1}. A ligated CoNTA complex yields a strong carbonyl stretch at 1622 cm^{-1}.[66] NTA itself is a trianionic chelating ligand. So, if NTA does bind to Ru, we should expect a strong carbonyl peak somewhere in the vicinity of 1622 and 1599 cm^{-1}. The presence of such a peak may suggest that there is some interaction between NTA and Ru, but further spectroscopic data is necessary to give a positive identification of an NTARu complex. On the other hand, ESI-MS can identify ruthenium by its isotopic distribution, making it potentially easy to identify any ruthenium containing products, alongside any bound ligands. However, this is only true if the product obtained is both soluble and easily ionizable. For the attempts where ruthenium was detectable, mass spectrometry showed the binding of ruthenium to coordinating ligands such as pyridine and acetonitrile. For trials 4 and 6,

the oxidation state of ruthenium per the charge balance found in the ESI is +2. For trial 9 both the +2 and +3 oxidation state were observed as well. Trial 11 also exhibits a complex with a +3 oxidation state. It is also the only trial where there is any evidence of an NTA-Ru complex, although in this case ruthenium is found with 2 NTA ligands, which appear to be partially protonated or charge balanced with potassium.

The difference in outcomes can be partially rationalized on a hard/soft acid-base basis. Low oxidation-state ruthenium itself is a relatively soft acid, so it favors interactions with soft bases, of which the carboxylic acid functional groups on NTA are decidedly not. In the presence of soft bases such as acetonitrile and pyridine without fail a ligated ruthenium species appears in the mass spec. In all of these cases the relatively softer +2 oxidation state is present, although the +3 oxidation state is present in trials involving pyridine. Trial 11 has ruthenium in the +3 oxidation state, with 2 NTAs associated with it. If there is bonding occurring between Ru and NTA, then these are bound predominately by the carboxylates. This suggests that to actually bind NTA to Ru a higher oxidation state and a harder Ru is necessary. In addition, a different source of Ru was used alongside a strong acid, as opposed to several trials that used either weak or strong bases. A hard acid such as $HClO_4$ is fairly oxidizing which likely stabilizes the higher oxidation state. Combined with the aqueous solvent, which in hard base, the reaction itself almost exclusively contains hard acids and bases. To this end, it may be that targeting an NTARu requires a predominately hard environment, lest NTA be outcompeted by softer ligands. With that being said, the presence of two NTAs with Ru is not preferred. It may be that more careful considerations are required to obtain a Ru complex bound by a single NTA ligand.

Table 21: Summary of synthetic conditions used and analysis used in attempts to synthesize an (NTA)Ru complex.

Trial	Ru Source	Ligand	Reagent	Solvent	Temp.	IR	ESI
1	$RuCl_3$•$3H_2O$	$NTAH_3$	KOH	Water	RT	$NTAH_3$	No Ru
2		$NTAH_3$	Et_3N	Acetone	RT	Unclear	No Ru
3		$NTAH_3$	KOH	CH_3CN	RT	Na_3NTA	N/A
4		$NTAH_3$	KOH	CH_3CN	Reflux	$NTAH_3$/ CH_3CN	$RuCl_x(CH_3CN)_y$
5		Na_3NTA	none	CH_3CN	RT	Multiple NTA/ CH_3CN	N/A
6		Na_3NTA	none	CH_3CN	BP of CH_3CN	Multiple NTA	$RuCl_x(CH_3CN)_y$
7		Na_3NTA	none	MeOH (Anhyd.,Ar)	RT	NTA Present	No Ru
8		Na_3NTA	none	MeOH (Anhyd.,Ar)	Reflux	Multiple NTA	No Ru
9[64,65]		$NTAH_3$	none	Pyridine	RT	Pyridine Present	$RuCl_x(C_5H_5N)_y$
10[66]		$NTAH_3$	Pyridine H_2O_2	Water	60°C	Pyridine Multiple NTA	N/A
11[63]	K_2RuCl_5•H_2O	$NTAH_3$	HClO4	Water	Reflux	Multiple NTA	$K_xH_yRu(NTA)_2$

Summary of Experimental Results

The $(AHA)_2RuO^-$ complex (complex **3**) was successfully synthesized and characterized according to literature procedure. Both thermolysis and photolysis of complex **3** seemed to indicate that the complex underwent decomposition. At present there is no definitive evidence to conclude one way or the other whether complex **3** is evolving oxygen. That being said, the decomposition of complex **3** under fairly modest conditions paints a somewhat pessimistic picture of the viability of this complex. Regardless, more rigorous studies are necessary to give a solid conclusion.

A number of synthetic methods were used pursuing a stable and characterizable NTA ruthenium complex. While none were successful, they do provide a clear direction for future

attempts. Of the 11 trials, only trial 11 showed any evidence of NTA bound to ruthenium. Trial 11 is different from trials 1-10 in a number of ways. All of the other trials utilize base in some way, whether it be an added reagent, the trianionic NTA ligand, or the solvent itself. By contrast, trial 12 is in fairly acidic media ($HClO_4$). In addition, the $K_2RuCl_5(H_2O)$ starting material is used here instead of $RuCl_3*3(H_2O)$. To properly synthesize and isolate an NTARu complex, a hard acid is necessary to ensure that NTA is bound to ruthenium. Work-up with a strong base to neutralize and to limit the number of NTA per ruthenium may be necessary. In addition, a more vigorous oxidizing agent could be utilized to directly produce a ruthenium (IV) hydroxide or ideally a ruthenium (V) oxo complex. The attempts made here alongside the literature on metal NTA complexes strongly imply that an NTARu complex can be synthesized under the right conditions.

Conclusions

The ability of a number of ruthenium (V) oxo complexes to undergo the oxygen evolution reaction has been evaluated. Gas-phase calculations have demonstrated two distinct phenomena. The first is the effect of charge. Both anionic complexes evaluated, $(AHA)_2RuO^-$ and $NTARu(O)Cl^-$, demonstrated prohibitively large free energies of coupling. This suggests that anionic complexes will not be able undergo the oxygen evolution reaction. Initial experimental on the $(AHA)_2RuO^-$ seems to corroborate this finding, yielding only decomposition products under the experimental conditions employed. However, more work is required to reach a definitive conclusion on an experimental basis. The second phenomena observed is that of coordination number. In comparison of the NTARuO(L) complexes with the NTARuO complex, and the $BDARuO(Py)_2^+$ complex with the $BDARuO(Py)^+$, the effect of coordination number is apparent. The sterically strained 7-coordinate $BDARuO(Py)_2^+$ experiences considerably lower free energies of oxygen evolution than it's octahedral counterpart (-57.1 kcal/mol vs. -28.5 kcal/mol from the bridged peroxide). The octahedral NTARuO(L) complexes experience fairly modest oxygen evolution thermodynamics (+7.7 kcal/mol), but the 5-coordinate NTARuO series has substantially large thermodynamic barrier for these steps (+60.0 kcal/mol), similar in magnitude to the barriers seen in the anionic complexes. Therefore, steric crowding in the coordination sphere of the catalyst can provide a significant driving force for oxygen evolution, while complexes that are undercoordinated may experience significant barriers.

Transition states were determined in the gas phase for the coupling step for complexes NTARuO, NTARuO(Pyr), $NTARuO(NH_3)$, and PorRuO(Cl). The activation energies for all 4 complexes are fairly modest, reaching a maximum of 22.3 (determined by OPBE, $\Delta G^{\ddagger}$ for NTA complexes in B3LYP and M06 are similar in magnitude). With the exception of the NTARuO

which is has a fairly large oxygen evolution free energy, the modest activation energies and the modest free energies along the reaction coordinate suggest that all 3 complexes may be suitable oxygen evolution catalysts.

The effect of solvation on the ligated complexes illustrates 2 effects. The first is a destabilization of the bridged peroxide. Comparatively poor solvation of the bridged peroxide results in a destabilization of the transition state, driving the up the activation barrier and free energy of coupling. This destabilization is on the order of roughly 10 kcal/mol, which is significant, but not crippling by any measure. On the opposite side of this reaction, the free energies for metal dissociation and oxygen evolution are driven down significantly, so that the entire process results in a net exergonic reaction. In both the gas phase and in water, ligated NTA complexes appear to be well suited for the oxygen evolution reaction. To this end, several attempts were made to synthesize an NTARu complex. While no method yielded a well separated and well characterized NTARu complex, they did illustrate that hard acids, rather than soft bases, may be necessary to achieve coordination of the NTA ligand. This suggests that it is possible to synthesize an NTARu complex, provided that the proper methods are employed.

Of the remaining non-NTA-ligated complexes, only the PorRuO(Cl) complex appears to have favorable activity for the OER reaction. With a modest coupling barrier of 19.4 kcal/mol (determined by OPBE). The free energy requirements for this complex to evolve dioxygen fairly small, coming out to be net-neutral. Transition states were not located for the metal dissociation and oxygen evolution steps and could very well be rate-limiting, showing the PorRuO(Cl) complex to be unfavorable from a kinetic standpoint, however this is true for every complex studied here. As it stands, it appears that the PorRuO(Cl) complex may be a good candidate for OER reactivity. The $(DMG)_2RuO(Cl)$ complex shows a modest free energy requirement for O-O

coupling, but the subsequent metal dissociation reaction is incredibly uphill, and the activation barrier for this is likely higher. In this regard, this complex will likely not perform well undergoing the oxygen evolution reaction.

The work herein has demonstrated a number of important aspects for the oxygen evolution reaction. Anionic complexes and ruthenium (V) oxo complexes with a coordination number less than 6 experience increased energy requirements for the oxygen evolution reaction. Activation barriers for the coupling step for the ligated NTA complexes and the POR complex are moderate, indicating promising behavior for the OER. Solvation of the ligated NTA complexes destabilizes the coupling step, but lowers energy requirements for subsequent steps, making the NTA complexes promising candidates for the OER. Attempts to synthesize an NTARu complex, while unsuccessful, demonstrate potential for future syntheses.

Future Directions

The work presented herein gives a number of avenues to explore for future work. While in general, the radical coupling step of the oxygen evolution reaction is rate limiting, we did not explore the possibility of the metal dissociation or the oxygen evolution step being rate limiting. Locating the transition states for each of these complexes could provide more insight into the mechanism for the oxygen evolution reaction. In terms of solvent modeling, a single solvent was employed in this work, and it was used on a small subset of the complexes included. Expanding the use of this solvent model to all of the complexes included is important vital for effectively applying the lessons of this work to real systems. While the implicit solvation model used here can not compensate for explicit interactions that may come from hydrogen bonding, Van der Waals interactions, etc., it can provide insight on the affect that solvent polarity has on the OER. Utilizing a wider array of solvents that range from non-polar (hexane, benzene) to more polar (acetone, acetonitrile), can explore the effect of solvation in more depth. Doing so allows the details of this study to be applied not only to water oxidation, but to other systems that may not involve water or proton-coupled electron transfers.

The issue of the initial formation of the ruthenium (V) oxo by means of oxidation (by cerium (IV) or otherwise) has not been addressed in any significant way here. To assess the ability of the complexes to act as water oxidation catalysts, the thermodynamics and kinetics of converting the Ru(II)- or Ru(III)-aqua complexes into the Ru(V) oxo complex. Looking outside of water oxidation, we can explore the oxygen affinity of the Ru(III) complex by studying the reactivity of the Ru(III) complexes with oxidizing agents such as chlorates or bromates, phosphine oxides, and oxygenated organic substrates. This should be done in areas where there is sufficient literature so that comparisons to experimental and computational studies can be made.

We can also expand this body to assess the ability of these complexes to perform small molecule splitting reactions for greenhouse gases such as CO_2 and N_2O. For CO_2, utilizing these oxygen evolution catalysts as oxygen acceptor (reducing agent) may provide insight on the decomposition of CO_2 into CO, which has use as a major component of syn gas. For N_2O, this process can help elucidate some of the finer details in the global nitrogen cycle, determining how oxidized nitrogen returns to the atmosphere as N_2 gas.

Experimentally, there is a clear path forward. For the $(AHA)_2RuO^-$ complex, initial experiments were focused on detection and characterization of ruthenium containing products using UV-Vis and MS. This can tell us the rate of reaction with respect to the metal, but it does not give us any direct information on the evolution of oxygen. Directly detecting both the dissolved oxygen and headspace oxygen can give us important information on whether an oxygen evolution reaction is occurring. It can also tell us the total rate of oxygen evolution. This can be done by using specialized columns designed to separate small gases, such as O_2, CO, CO_2, etc. Utilizing such a column would not only allow for the tracking of O_2, but it can also allow for the detection of CO_2, which may be a decomposition product of the AHA complex. These methods would provide for a conclusive means as to whether oxygen evolution or decomposition is occurring.

As for the synthesis of an (NTA)Ru complex, more acidic and oxidizing conditions can be employed. A strong acid such as $HClO_4$ or HCl can be used in this manner. It is possible that these reagents may produce a $(NTA)RuCl^-$ or even a $(NTA)RuCl_2^{2-}$ species, which according to our calculations would be unfavorable for the oxygen evolution reaction. A reagent such as $AgNO_3$ could be used in conjunction with a more favorable coordinating ligand, such as pyridine or water, to form a more active complex. Furthermore, a strong oxidizing agent such as $NaBrO_3$

could be employed to bypass the reduced ruthenium (III) complex, to form a more oxidized complex, such as a ruthenium (IV) hydroxide, a ruthenium (VII) dioxide, or the preferred ruthenium (V) oxo.

III. Experimental Section

General Methods and Materials

All reactants and materials were obtained commercially and used without further modification. All solvents used were ACS grade. IR spectra were obtained using a Shimadzu IRAffinity-1 and processed using IRSolution software. UV-vis spectra were obtained with a Hewlett Packard 8452A Diode Array Spectrophotometer and processed with the complementary software package. Quantum chemical calculations were done using the Gaussian09 software package[67] in GaussView4[68]. Molecular geometries were modelled using CYLview 1.0.[69]

Geometry Optimizations and Single Point Calculations

Ground states geometries were optimized utilizing unrestricted DFT. An ultrafine grid was used for all geometry optimizations. Frequency calculations were run in tandem with every geometry optimization to determine the Gibbs free energy. Optimizations were done utilizing B3LYP[31–33] and OPBE[34–37]. The basis set 6-31G(d)[38–42] was used for H, C, N, and O, and the basis set 6-311++G(d,p)[43,44] was used for Cl. The LANL2DZ[45–47] basis and effective core potential (ECP) was used for Ru. Single point energy calculations were done on B3LYP optimized geometries (and OPBE geometries where noted) utilizing the M06[48,70] functional. For M06 calculations, the SDD (Stuttgart-Dresden)[49] basis and ECP was used for Ru. The basis set 6-311++G(d,p)[43,44] was used for H, C, N, O, and Cl. Optimizations were done in the gas-phase without a solvent model. In addition to gas phase calculations, the Conductor-like Polarizable Continuum Model (CPCM)[50] solvent model for water was used on the NTARuL (L = NH_3, Pyridine, H_2O) complexes.

Transition State Location and Optimization

Transition states were located by scanning selected bond lengths with relaxed mod redundant calculations using either B3LYP or OPBE. Maxima in energy were located along the mod redundant scan. Geometries at these maxima were then optimized to a transition state utilizing TSBerny, followed by a frequency calculation. Transition states contained a single imaginary frequency. Transition state energies for M06 were completed by performing single point energy calculations on the B3LYP/OPBE optimized transition state.

Preparation of Tetrapropyl Ammonium Perruthenate $(Pr)_4N^+[RuO_4]^-$ [29,71]

Ruthenium (III) chloride trihydrate (0.7844 g, 3 mmol, 1 equivalence) was dissolved in 15 mL of deionized water (DI water), forming a dark red-brown solution. This solution was added to a 120 mL solution containing an excess of $NaBrO_3$ (40 eq.) and Na_2CO_3 (30 eq.). The resulting solution was stirred for 2 hours, forming a dark yellow solution. After 2 hours, 3 mL of 1 M tetrapropyl ammonium hydroxide (1 eq.) was added to the reaction solution, causing the precipitation of a dark green solid. Green precipitate was extracted using 4 washes of 75 mL of dichloromethane. The green solution was dried over $MgSO_4$, filtered, then concentrated to roughly 20-25 mL. A dark green solid was precipitated using carbon tetrachloride. The resulting product was filtered then dried in vacuo, yielding 0.8223 g of product (78% yield).

IR /cm^{-1}: 2920 (C-H), 1480(C-H), 1100 (C-N), 1055 (C-N), 836 (s, RuO_2 asym).

UV-Vis (DCM) Wavelength/nm (molar absorptivity/L*mol^{-1}*cm^{-1}): 232 (3010), 318 (2030), 386 (1820).

Preparation of Tetrapropyl Ammonium Bis-2-ethyl-2-hydroxybutyrato(oxo) Ruthenate (V)

$(C_3H_7)_4N^+[(C_6H_{10}O_3)_2RuO]^-$[28,29]

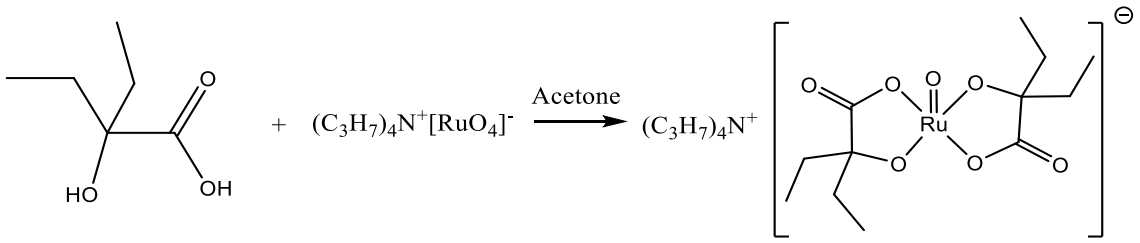

Tetrapropyl ammonium perruthenate (0.2811 g, 0.8 mmol, 1 equiv.) was dissolved in 20 mL of acetone forming a dark yellow green solution. Two equivalences of the α-hydroxy acid ligand (1.6 mmol, 0.2115 g) was added to the solution, forming a dark brown solution. After stirring for 48 hours, 60 mL of hexane was added. The supernatant solution was decanted, and the remaining solid was dried in vacuo. The supernatant was then concentrated to 20 mL using rotary evaporation, precipitating light brown crystals. The solution was filtered, and the extra light brown crystals were also dried in vacuo, yielding a total mass of 0.3988 g (88% yield).

IR /cm^{-1}: 2980(C-H), 1770(s, C=O), 900 (s, Ru=O).

UV-Vis (DCM) Wavelength/nm (molar absorptivity/L*mol^{-1}*cm^{-1}): 328 (1161), 394 (1021), and 472 (1157).

EPR (9.739072 GHz, DCM) g (H/Gauss): 1.986 (3503.7).

Negative Ion ESI-MS: 378.0305 (m/z)

General Synthesis of Nitrilotriacetato Ruthenium Complexes

Ruthenium (III) chloride trihydrate (0.5 mmol, 1 equiv.) was dissolved in 5-10 mL of solvent. One equivalent of the nitrilotriacetate ligand ($NTAH_3$ or Na_3NTA) was added to 20-25 mL of solvent. To the ligand containing solution, 3 equivalences of base were added. This solution was then allowed react for at least 24 hours, at either room temperature or the boiling point of the solvent used. The resulting solution was examined for precipitate, which if present, was separated from the solution by filtration.

Trial	Ru Source	Ligand	Reagent	Solvent	Temp.
1	$RuCl_3•3H_2O$	$NTAH_3$	KOH	Water	RT
2		$NTAH_3$	Et_3N	Acetone	RT
3		$NTAH_3$	KOH	CH_3CN	RT
4		$NTAH_3$	KOH	CH_3CN	BP of CH_3CN
5		Na_3NTA	none	CH_3CN	RT
6		Na_3NTA	none	CH_3CN	BP of CH_3CN
7		Na_3NTA	none	MeOH (Anhydrous,Ar)	RT
8		Na_3NTA	none	MeOH (Anhydrous,Ar)	BP of MeOH
9[64,65]		$NTAH_3$	none	Pyridine	RT
10[66]		$NTAH_3$	Pyridine, H_2O_2	Water	60°C

Trial 1

Addition of $RuCl_3•3H_2O$ to water forms a dark brown solution. Addition of ligand to the $RuCl_3$ solution results in no color change, but addition of KOH yields a slightly greener solution. After 2 days, a brown precipitate was collected from solution. The remaining solution was concentrated to a dark brown oil. The IR spectrum of the precipitate matched precisely to reported IR spectrum of $NTAH_3$. The IR spectrum of the oily filtrate contained significant

intensities corresponding to a O-H stretching frequency and a C=O frequency at a lower stretching frequency than that of the pure $NTAH_3$, indicating carboxylate character. There was no evidence of Ru in the ESI for the filtrate.

Precipitate, IR /cm^{-1}: 3041(m, C-H), 1734(s, C=O), 1246(s, C-N), 1225(s, C-N).

Filtrate, IR /cm^{-1}: 3283(w, C-H), 1640(s, C=O), 1400(m, C-H), 1308(m, C-N).

Trial 2

Addition of $RuCl_3*3H_2O$ to acetone forms a dark red solution. The $NTAH_3$ ligand is initially insoluble, but eventually dissolves. Addition of Et_3N causes small amount of smoke/gas, and the formation of a dark brown precipitate around the edge of the flask. Filtration of the solution yields a brown precipitate, with an IR spectrum that matches that of the $NTAH_3$ compound. The filtrate was concentrated, yielding red oil. There was no evidence of Ru in the ESI for the filtrate.

Precipitate, IR /cm^{-1}: 3404(b, O-H), 3059(s, C-H), 2984(s, C-H), 1740(s, C=O).

Trial 3

Addition of $RuCl_3*3H_2O$ to acetonitrile forms a dark red, yellow solution which slowly turns black. Both KOH and $NTAH_3$ are initially insoluble, but gradually dissolve, forming a blood red solution. After an hour, the solution begins to turn brown, precipitating a dark brown precipitate. After 2 days, the solution was a light-yellow green, with a dark green-black precipitate. Filtration of the precipitate yields a dark brownish green precipitate, and a yellow green filtrate. The filtrate was then concentrated to a solid yellow, nearly colorless compound. The IR of the precipitate shares a number of peaks with Na_3NTA, including the broadened C=O

stretch that is characteristic of the 3 carboxylates. The filtrate IR suggest the presence of some amount of acetonitrile showing a clear C=N. There are also two peaks in C=O range, although the intensity is far smaller than what would be expected from a pure carbonyl containing compound, indicating that the filtrate likely contains a mixture of NTA, CH_3CN, and other byproducts.

Precipitate, IR /cm^{-1}: 3041(m, C-H), 1734(s, C=O), 1246(s, C-N), 1225(s, C-N).

Filtrate, IR /cm^{-1}: 3456(b, C-H), 2965(s, C-H), 2911(s, C-H), 2276, (m, C=N), 1663(w, C-N).

Trial 4

Addition of $RuCl_3 \bullet 3H_2O$ to acetonitrile forms a dark red-yellow solution which slowly turns black. Both KOH and $NTAH_3$ are initially insoluble, but gradually dissolve, forming a blood red solution. The solution was refluxed at 89°C, causing the deep red solution to become a more translucent brighter red. After a day, a light brown precipitate started to form. After a second day of refluxing more precipitate had formed, and the solution had become a more translucent orange color. The precipitate was separated by filtration giving a sticky brown substance. The solution was then concentrated, and an aliquot was taken and subjected to vapor diffusion in toluene. Light red crystals were grown, but preliminary SXRD only showed the presence of a Ru-$NCCH_3$ type complex with no NTA present. The IR for the precipitate matched the IR of the $NTAH_3$ ligand. Positive ion ESI showed various $Ru(CH_3CN)_xCl_y^+$. Negative ion ESI showed a number of $RuCl_y^-$ species. This suggests that there was a significant amount of unreacted Ru.

Precipitate, IR /cm^{-1}: 3413(b, O-H), 3041(m, C-H), 2999(m, C-H), 1726(s, C=O).

Filtrate, IR /cm^{-1}: 3576(b, O-H), 2976(s, C-H), 2918(s, C-H), 2326 (m, C≡N), 1663(w, C-N).

Positive Ion ESI-MS: 177.8986 (m/z); $Ru(CH_3CN)Cl^+$

Negative Ion ESI-MS: 208.8116 (m/z); $RuCl(HCl)_2^-$

Trial 5

Addition of $RuCl_3•3H_2O$ to acetonitrile forms a dark red, yellow solution which slowly turns black. Only Na_3NTA was added to the solution resulting in little initial color change. Na_3NTA is also partially insoluble. Room temperature solution is relatively unchanged after 8 hours, aside from the precipitation of a small amount of yellow-green precipitate. After stirring at room temperature for an additional day and a half, more green precipitate had formed, though the color of the solution had still not changed. The solution was decanted from green precipitate, which was then dried in vacuo. The filtrate was concentrated to a solid. The IR spectrum of the precipitate matched fairly closely the spectrum of free Na_3NTA. The deviations were apparent on the C=O stretch, where three unique peaks can be seen, showing that this sample is a mixture. The IR spectrum of the filtrate showed what looks like a single C=O stretch, alongside a C≡N stretch, which does not match any of the reagents employed here.

Precipitate, IR /cm^{-1}: 3369(b, O-H), 1730(s, C=O), 1668(s, C=O), 1599(s, C=O), 1406(s, O-H).

Filtrate, IR /cm^{-1}: 34979(b, O-H), 2978(w, C-H), 2920(w, C-H), 2328 (m, C≡N), 1632(s, C=O), 1406(m, C=O).

Trial 6

Addition of $RuCl_3*3H_2O$ to acetonitrile forms a dark red, yellow solution which slowly turns black. Only Na_3NTA was added to the solution resulting in little initial color change. Na_3NTA is also partially insoluble. Refluxed solution within 5-6 hours turns a lighter translucent yellow-orange, with the formation of a large amount of orange precipitate. Solution was

decanted from the precipitate. The precipitate was then dried under high vacuum. The filtrate was concentrated to a solid. The IR for both the precipitate and filtrate contain multiple carbonyls. The ESI contains a variety of $Ru(CH_3CN)_xCl_y$ ions, indicating there is no NTARu species in significant amounts.

Precipitate, IR /cm^{-1}: 3448(b, O-H), 1721(s, C=O), 1636(s, C=O), 1404(m, O-H).

Filtrate, IR /cm^{-1}: 3485(b, O-H), 2976(m, C-H), 2920(m, C-H), 1736(w, C=O), 1653(s, C=O), 1420(w, O-H).

Positive Ion ESI-MS: 503.7310 (m/z); $Ru2(CH_3CN)_3Cl_5^+$

Trial 9[64,65]

One equivalence of $NTAH_3$ was dissolved in refluxing pyridine, then allowed to cool, resulting in a slightly yellow translucent solution. One equivalence of $RuCl_3•3H_2O$ was added to the $NTAH_3$-pyridine solution, resulting in the change of the color from clear to dark green. After stirring for 18 hours, the solution has turned to a more yellow green color. The solution was then concentrated to a black oil by rotary evaporator. Multiple C=O stretches were observed in the IR, indicating the presence of several NTA species. There are also peaks in the fingerprint region characteristic of pyridine. The mass spectrum shows combinations of $Ru(C_5H_5N)_xCl_y$ ions, indicating an NTARu species is not present.

Filtrate, IR /cm^{-1}: 3439(b, O-H), 3121(m, C-H), 1728(s, C=O), 1736(w, C=O), 1653(s, C=O), 1420(w, O-H).

Positive Ion ESI-MS: 374.0015 (m/z); $Ru(C_5H_5N)_3Cl^+$

Trial 10[66]

One equivalence of $NTAH_3$ was partially dissolved in 15 mL room temperature water. Three equivalences of pyridine (0.092 mL) were added to the solution, completely dissolving the $NTAH_3$. One equivalence of $RuCl_3•3H_2O$ was dissolved in a separate 15 mL, forming a dark brown solution. The ruthenium containing solution was then added to the $NTAH_3$ and pyridine containing solution. The resulting solution immediate began to turn red-brown and quickly became a dark yellow-green. The reaction solution was then heated at 60°C for 20 minutes. Then, an excess of H_2O_2 was added (2.1 equiv.) to the solution. Upon addition, the solution began to bubble, and turn brown. This solution was left to sit without stirring for two days, turning blue and forming black precipitate. The IR spectrum shows multiple individual C=O peaks, indicating a significant variety of NTA species in the product.

Filtrate, IR /cm^{-1}: 3424(b, O-H), 1738(w, C=O), 1636(w, C=O), 1609(w, C=O).

Positive Ion ESI-MS: 503.7310 (m/z); $Ru2(CH_3CN)_3Cl_5^+$

General Procedure for Trials 7 and 8

Both methanol and Na_3NTA were pre-dried before the reaction. Methanol was dried with activated 3Å sieves. Na_3NTA was dried under high-vacuum and heated with a heat gun. $RuCl_3*3H_2O$ was then added to the dried methanol, forming an opaque brown solution. This solution was then sparged with N_2 for 10-15 minutes. After this, the flask was sealed with a rubber stopper. Half of the solution was transferred via glass syringe to another sealed, N_2-filled flask. One half equivalence of Na_3NTA was added to each flask. No immediate change in color was visible.

Trial 7

After the addition of Na_3NTA, the solution was stirred at room temperature for 2 and a half hours, resulting in a yellow green solution, with a small amount of orange precipitate. The solution was left to stir overnight, producing a deep orange-brown solution. Slightly more precipitate was produced as well, with an orange-brown color, though it was not present any quantities significant enough for analysis. The reaction solution was concentrated to a solid, resulting in a brown solid. This crude product resisted attempts to dissolve it in methanol at room temperature, but it was slightly soluble in chloroform. The IR spectrum shows only a single NTA carbonyl. No ruthenium was detected in the ESI mass spectrum.

Crude Product, IR /cm^{-1}: 3435(b, O-H), 1636(s, C=O).

Trial 8

After the addition of Na_3NTA, the solution was refluxed at 76°C, turning the solution orange/red after 2.5. The solution was left to reflux overnight, though there was solvent loss due to insufficient cooling. An additional 25 mL of dried methanol was added to redilute the sample, resulting in an opaque light orange-brown solution. After an additional day at reflux, the solution was concentrated to a solid, giving a tan product. The IR spectrum indicates the presence of several NTA species. No ruthenium was detected in the ESI mass spectrum.

Precipitate, IR /cm^{-1}: 3429(b, O-H), 1668(s, C=O), 1632(s, C=O).

Filtrate, IR /cm^{-1}: 3441(b, O-H), 1670(s, C=O), 1632(s, C=O), 1599(s, C=O).

Synthesis of Potassium Ruthenium (III) Pentachloride Monohydrate $K_2NTARuCl_2*H_2O$[72]

To a solution of concentrated HCl, one equivalence (1.0029 g, 3.836 mmol) of $RuCl_3•3H_2O$ was dissolved, initially forming a deep red solution. To this solution, 2 eq. of KCl (1.575 g) were added, causing the solution to become slightly more orange. This is followed by the addition of 57 μL of Hg, causing the solution to become brown. After this addition, a small amount of fine dark grey mercurous chloride formed. After stirring overnight, the excess mercury and mercurous chloride were filtered off. The filtrate was then concentrated to a small volume, partially precipitating red crystals alongside some grey solid. To eliminate the grey solid, the solution was diluted again in DI water and re-filtered, yielding a homogeneous red solution. This solution was reconcentrated and then cooled in ice, yielding a red crystalline solid. The solution was then filtered, and the red solid was washed with ethanol. The washed product was then recrystallized from 6M HCl solution, yielding 0.6672g of product (46% yield). Negative Ion ESI-MS: 243.7723 (m/z); $RuCl_4$-

Synthesis of Potassium Nitrilotriacetato Ruthenium (III) Chloride Monohydrate $K_2NTARuCl_2*H_2O$[63]

One equivalence of $K_2RuCl_5•H_2O$ (0.3752 g, 1 mmol) was dissolved in 10 mL of 1 mM $HClO_4$ heating at 50°C, forming a deep red solution. A slight excess of $NTAH_3$ (1.02 eq, 0.195 g) was dissolved in a separate 10 mL of room temperature 1 mM $HClO_4$. This solution was slowly added to the solution of $K_2RuCl_5•H_2O$. Due to poor solubility, an additional 5 mL of $HClO_4$ solution was used to transfer the $NTAH_3$ to the reaction solution. This solution was refluxed for 2 hours, showing a change from red, to orange, to yellow. After 2 hours, the solution was concentrated to approximately 5 mL. Cold ethanol was then added, causing the immediate

precipitation of a yellow solid. The reaction solution was subsequently filtered with 9:1 acetone:water. The pale yellow precipitate was washed with the aforementioned solution. Precisely 0.1736 g of product was collected. The IR spectrum shows two carbonyl absorptions from two distinct NTA complexes. The mass spec shows two NTAs coupled to a ruthenium atom.

IR /cm^{-1}: 2945(C-H), 1742(s, C=O), 1742(s, C=O), 1609(s, C=O), 1358(s, COO), 1225(s, C-O).

UV-Vis (DCM) Wavelength/nm (molar absorptivity/$L*mol^{-1}*cm^{-1}$): 202, 242.

Positive Ion ESI-MS: 481.9760 (m/z); $(C_6H_6O_6N)_2H_4Ru^+$

Negative Ion ESI-MS: 479.9625 (m/z); $(C_6H_6O_6N)_2H_2Ru^-$

Thermolysis of $(Pr)_4N^+[(AHA)_2RuO]^-$

Complex **3** (23.8 mg, 38.9 μmol) was added to a thick-walled Ace glass reactor tube. To this reactor tub 5 mL of dichloroethane (DCE) was added, forming an 8.43 mM solution. Once complex **3** was completely dissolved, the solution was sparged with argon for 15 minutes, then a small aliquot of 0.3 mL was taken and set aside. The solution was then sealed with a Teflon cap and placed in an oil bath at 150°C. The reaction was heated for 20 hours, then allowed to cool to room temperature. An additional aliquot of 0.3 mL was taken. The reaction tube was resealed, then placed back in the oil bath for an additional 4 hours. After 4 hours, the tube was taken out of the bath and another aliquot of 0.3 mL was taken. Each aliquot was diluted to by a factor of 10, and a UV-Vis spectrum was obtained. These diluted solutions were further diluted by a factor of 8, and an additional UV-Vis spectrum was contained. An aliquot of the reaction solution was run through electron impact GC/MS.

Photolysis of $(Pr)_4N^+[(AHA)_2RuO]^-$

Complex **3** (10.0 mg, 1.8 μmol) was dissolved in 20 mL of DCE, to form a 0.89 mM solution. A small amount of this solution was then added to a screw cap quartz cuvette, so that the cuvette ¾ of the way filled. This solution was then sparged with argon for 15 minutes. Once complete, the cuvette was sealed a septa screw cap. An initial UV-Vis spectrum was acquired. The cuvette was then immobilized in a photochemical reactor with lamps that emit UV light at 150 and 250 nm. A fan in the reactor was utilized to prevent thermal effects from the high energy radiation. The lamps were then turned on. The cuvette was then irradiated for periods of 30 minutes for a total time of 6 and a half hours. After every 30 minute period, the cuvette was taken out and a UV-Vis spectrum was obtained. This process was repeated for a more dilute sample (0.11 mM) in order to resolve behavior in the UV region.

LITERATURE CITED

(1) Steffen, W.; Rockström, J.; Richardson, K.; Lenton, T. M.; Folke, C.; Liverman, D.; Summerhayes, C. P.; Barnosky, A. D.; Cornell, S. E.; Crucifix, M.; et al. Trajectories of the Earth System in the Anthropocene. *Proc. Natl. Acad. Sci. U. S. A.* **2018**, *115* (33), 8252–8259.

(2) Balmaseda, M. A.; Trenberth, K. E.; Källén, E. Distinctive Climate Signals in Reanalysis of Global Ocean Heat Content. *Geophys. Res. Lett.* **2013**, *40* (9), 1754–1759.

(3) Stocker, T. F.; Qin, D.; Plattner, G. K.; Tignor, M. M. B.; Allen, S. K.; Boschung, J.; Nauels, A.; Xia, Y.; Bex, V.; Midgley, P. M. *Climate Change 2013 the Physical Science Basis: Working Group I Contribution to the Fifth Assessment Report of the Intergovernmental Panel on Climate Change*; 2013; Vol. 9781107057.

(4) Field, C. B.; Barros, V. R.; Dokken, D. J.; Mach, K. J.; Mastrandrea, M. D.; Bilir, T. E.; Chatterjee, M.; Ebi, K. L.; Estrada, Y. O.; Genova, R. C.; et al. Climate Change 2014 Impacts, Adaptation and Vulnerability: Part A: Global and Sectoral Aspects: Working Group II Contribution to the Fifth Assessment Report of the Intergovernmental Panel on Climate Change. *Clim. Chang. 2014 Impacts, Adapt. Vulnerability Part A Glob. Sect. Asp.* **2014**, 1–1131.

(5) Barros, V. R.; Field, C. B.; Dokken, D. J.; Mastrandrea, M. D.; Mach, K. J.; Bilir, T. E.; Chatterjee, M.; Ebi, K. L.; Estrada, Y. O.; Genova, R. C.; et al. Climate Change 2014 Impacts, Adaptation, and Vulnerability Part B: Regional Aspects: Working Group II Contribution to the Fifth Assessment Report of the Intergovernmental Panel on Climate Change. *Clim. Chang. 2014 Impacts, Adapt. Vulnerability Part B Reg. Asp. Work. Gr. II*

Contrib. to Fifth Assess. Rep. Intergov. Panel Clim. Chang. **2014**, 1–1820.

(6) Bockris, J. O. M.; Dandapani, B.; Cocke, D.; Ghoroghchian, J. On the Splitting of Water. *Int. J. Hydrogen Energy* **1985**, *10* (3), 179–201.

(7) Boyarkin, O. V.; Koshelev, M. A.; Aseev, O.; Maksyutenko, P.; Rizzo, T. R.; Zobov, N. F.; Lodi, L.; Tennyson, J.; Polyansky, O. L. Accurate Bond Dissociation Energy of Water Determined by Triple-Resonance Vibrational Spectroscopy and Ab Initio Calculations. *Chem. Phys. Lett.* **2013**, *568–569*, 14–20.

(8) Cox, N.; Pantazis, D. A.; Neese, F.; Lubitz, W. Biological Water Oxidation. *Acc. Chem. Res.* **2013**, *46* (7), 1588–1596.

(9) Matheu, R.; Garrido-Barros, P.; Gil-Sepulcre, M.; Ertem, M. Z.; Sala, X.; Gimbert-Suriñach, C.; Llobet, A. The Development of Molecular Water Oxidation Catalysts. *Nat. Rev. Chem.* **2019**, *3* (5), 331–341.

(10) Hunter, B. M.; Gray, H. B.; Müller, A. M. Earth-Abundant Heterogeneous Water Oxidation Catalysts. *Chem. Rev.* **2016**, *116* (22), 14120–14136.

(11) Shi, Q.; Zhu, C.; Du, D.; Lin, Y. Robust Noble Metal-Based Electrocatalysts for Oxygen Evolution Reaction. *Chem. Soc. Rev.* **2019**, *48* (12), 3181–3192.

(12) Dong, S.; Feng, J.; Fan, M.; Pi, Y.; Hu, L.; Han, X.; Liu, M.; Sun, J.; Sun, J. Recent Developments in Heterogeneous Photocatalytic Water Treatment Using Visible Light-Responsive Photocatalysts: A Review. *RSC Adv.* **2015**, *5* (19), 14610–14630.

(13) Zaman, W. Q.; Sun, W.; Tariq, M.; Zhou, Z.; Farooq, U.; Abbas, Z.; Cao, L.; Yang, J. Iridium Substitution in Nickel Cobaltite Renders High Mass Specific OER Activity and

Durability in Acidic Media. *Appl. Catal. B Environ.* **2019**, *244*, 295–302.

(14) Zhu, K.; Zhu, X.; Yang, W. Application of In Situ Techniques for the Characterization of NiFe-Based Oxygen Evolution Reaction (OER) Electrocatalysts. *Angew. Chemie - Int. Ed.* **2019**, *58* (5), 1252–1265.

(15) Fabbri, E.; Schmidt, T. J. Oxygen Evolution Reaction - The Enigma in Water Electrolysis. *ACS Catal.* **2018**, *8* (10), 9765–9774.

(16) Song, J.; Wei, C.; Huang, Z. F.; Liu, C.; Zeng, L.; Wang, X.; Xu, Z. J. A Review on Fundamentals for Designing Oxygen Evolution Electrocatalysts. *Chem. Soc. Rev.* **2020**, *49* (7), 2196–2214.

(17) Duan, L.; Bozoglian, F.; Mandal, S.; Stewart, B.; Privalov, T.; Llobet, A.; Sun, L. A Molecular Ruthenium Catalyst with Water-Oxidation Activity Comparable to That of Photosystem II. *Nat. Chem.* **2012**, *4* (5), 418–423.

(18) Shaffer, D. W.; Xie, Y.; Concepcion, J. J. O-O Bond Formation in Ruthenium-Catalyzed Water Oxidation: Single-Site Nucleophilic Attack: Vs. O-O Radical Coupling. *Chem. Soc. Rev.* **2017**, *46* (20), 6170–6193.

(19) Xie, Y.; Shaffer, D. W.; Concepcion, J. J. O-O Radical Coupling: From Detailed Mechanistic Understanding to Enhanced Water Oxidation Catalysis. *Inorg. Chem.* **2018**, *57* (17), 10533–10542.

(20) Matheu, R.; Ertem, M. Z.; Benet-Buchholz, J.; Coronado, E.; Batista, V. S.; Sala, X.; Llobet, A. Intramolecular Proton Transfer Boosts Water Oxidation Catalyzed by a Ru Complex. *J. Am. Chem. Soc.* **2015**, *137* (33), 10786–10795.

(21) Chen, Z.; Vannucci, A. K.; Concepcion, J. J.; Jurss, J. W.; Meyer, T. J. Proton-Coupled Electron Transfer at Modified Electrodes by Multiple Pathways. *Proc. Natl. Acad. Sci. U. S. A.* **2011**, *108* (52), 1461–1469.

(22) Fan, T.; Zhan, S.; Ahlquist, M. S. G. Why Is There a Barrier in the Coupling of Two Radicals in the Water Oxidation Reaction? *ACS Catal.* **2016**, *6* (12), 8308–8312.

(23) Kang, R.; Chen, K.; Yao, J.; Shaik, S.; Chen, H. Probing Ligand Effects on O-O Bond Formation of Ru-Catalyzed Water Oxidation: A Computational Survey. *Inorg. Chem.* **2014**, *53* (14), 7130–7136.

(24) Cramer, C. J. *Essentials of Computational Chemistry Theories and Models Second Edition*, 2nd ed.; Hoboken, 2004.

(25) Martín, A.; Orpen, A. G. Structural Systematics. 6. Apparent Flexibility of Metal Complexes in Crystals. *J. Am. Chem. Soc.* **1996**, *118* (6), 1464–1470.

(26) Jiménez-Hoyos, C. A.; Janesko, B. G.; Scuseria, G. E. Evaluation of Range-Separated Hybrid and Other Density Functional Approaches on Test Sets Relevant for Transition Metal-Based Homogeneous Catalysts. *J. Phys. Chem. A* **2009**, *113* (43), 11742–11749.

(27) Minenkov, Y.; Singstad, Å.; Occhipinti, G.; Jensen, V. R. The Accuracy of DFT-Optimized Geometries of Functional Transition Metal Compounds: A Validation Study of Catalysts for Olefin Metathesis and Other Reactions in the Homogeneous Phase. *Dalton Transactions*. 2012, pp 5526–5541.

(28) Dengel, A. C.; Griffith, W. P.; O'Mahoney, C. A.; Williams, D. J. A Stable Ruthenium(V) Oxo Complex. X-Ray Crystal Structure and Oxidising Properties of Tetra-n-

Propylammonium Bis-2-Hydroxy-2-Ethylbutyrato(Oxo)- Ruthenate(V). *J. Chem. Soc. Chem. Commun.* **1989**, No. 22, 1720–1721.

(29) Dengel, A. C.; Griffith, W. P. Studies on Transition-Metal Oxo and Nitrido Complexes. 12.1 Synthesis, Spectroscopic Properties, and Reactions of Stable Ruthenium(V) and Osmium(V) Oxo Complexes Containing α-Hydroxy Carboxylate and α-Amino Carboxylate Ligands. *Inorg. Chem.* **1991**, *30* (4), 869–871.

(30) Khan, M. M. T.; Chatterjee, D.; Khan, N. H.; Kureshi, R. I.; Bhatt, K. N. Epoxidation of Cyclohexene with Iodosylbenzene Catalysed by Ru(III)-Dmg and Ru(III)-Dpg Complexes: Synthesis and Characterisation of Catalytically Active Ru(V)-Oxo Intermediates. *J. Mol. Catal.* **1992**, *77* (2), 153–158.

(31) Lee, C.; Yang, W.; Parr, R. G. Development of the Colle-Salvetti Correlation-Energy Formula into a Functional of the Electron Density. *Phys. Rev. B* **1988**, *37* (2), 785–789.

(32) Becke, A. D. Density-Functional Thermochemistry. III. The Role of Exact Exchange. *J. Chem. Phys.* **1993**, *98* (7), 5648–5652.

(33) Kim, K.; Jordan, K. D. Comparison of Density Functional and MP2 Calculations on the Water Monomer and Dimer. *J. Phys. Chem.* **1994**, *98* (40), 10089–10094.

(34) Swart, M.; Groenhof, A. R.; Ehlers, A. W.; Lammertsma, K. Validation of Exchange-Correlation Functional for Spin States of Iron Complexes. *J. Phys. Chem. A* **2004**, *108* (25), 5479–5483.

(35) Swart, M.; Ehlers, A. W.; Lammertsma, K. Performance of the OPBE Exchange-Correlation Functional. *Mol. Phys.* **2004**, *102* (23–24), 2467–2474.

(36) Handy, N. C.; Cohen, A. J. Left-Right Correlation Energy. *Mol. Phys.* **2001**, *99* (5), 403–412.

(37) Hoe, W.; Cohen, A. J.; Handy, N. C. Assessment of a New Local Exchange Functional OPTX. *Chem. Phys. Lett.* **2001**, *341* (June), 319–328.

(38) Ditchfield, R.; Hehre, W. J.; Pople, J. A. Self-Consistent Molecular-Orbital Methods. IX. An Extended Gaussian-Type Basis for Molecular-Orbital Studies of Organic Molecules. *J. Chem. Phys.* **1971**, *54* (2), 720–723.

(39) Hehre, W. J.; Ditchfield, K.; Pople, J. A. Self-Consistent Molecular Orbital Methods. XII. Further Extensions of Gaussian-Type Basis Sets for Use in Molecular Orbital Studies of Organic Molecules. *J. Chem. Phys.* **1972**, *56* (5), 2257–2261.

(40) Hariharan, P. C.; Pople, J. A. The Influence of Polarization Functions on Molecular Orbital Hydrogenation Energies. *Theor. Chim. Acta* **1973**, *28* (3), 213–222.

(41) Hariharan, P. C.; Pople, J. A. Accuracy of AHn Equilibrium Geometries by Single Determinant Molecular Orbital Theory. *Mol. Phys.* **1974**, *27* (1), 209–214.

(42) Francl, M. M.; Pietro, W. J.; Hehre, W. J.; Binkley, J. S.; Gordon, M. S.; DeFrees, D. J.; Pople, J. A. Self-Consistent Molecular Orbital Methods. XXIII. A Polarization-Type Basis Set for Second-Row Elements. *J. Chem. Phys.* **1982**, *77* (7), 3654–3665.

(43) McLean, A. D.; Chandler, G. S. Contracted Gaussian Basis Sets for Molecular Calculations. I. Second Row Atoms, Z=11-18. *J. Chem. Phys.* **1980**, *72* (10), 5639–5648.

(44) Krishnan, R.; Binkley, J. S.; Seeger, R.; Pople, J. A. Self-Consistent Molecular Orbital Methods. XX. A Basis Set for Correlated Wave Functions. *J. Chem. Phys.* **1980**, *72* (1),

650–654.

(45) Hay, P. J.; Wadt, W. R. Ab Initio Effective Core Potentials for Molecular Calculations. Potentials for the Transition Metal Atoms Sc to Hg. *J. Chem. Phys.* **1985**, *82* (1), 270–283.

(46) Wadt, W. R.; Hay, P. J. Ab Initio Effective Core Potentials for Molecular Calculations. Potentials for Main Group Elements Na to Bi. *J. Chem. Phys.* **1985**, *82* (1), 284–298.

(47) Hay, P. J.; Wadt, W. R. Ab Initio Effective Core Potentials for Molecular Calculations. Potentials for K to Au Including the Outermost Core Orbitale. *J. Chem. Phys.* **1985**, *82* (1), 299–310.

(48) Zhao, Y.; Truhlar, D. G. The M06 Suite of Density Functionals for Main Group Thermochemistry, Thermochemical Kinetics, Noncovalent Interactions, Excited States, and Transition Elements: Two New Functionals and Systematic Testing of Four M06-Class Functionals and 12 Other Function. *Theor. Chem. Acc.* **2008**, *120* (1–3), 215–241.

(49) Andrae, D.; Häußermann, U.; Dolg, M.; Stoll, H.; Preuß, H. Energy-Adjusted Ab Initio Pseudopotentials for the Second and Third Row Transition Elements. *Theor. Chim. Acta* **1990**, *77* (2), 123–141.

(50) Barone, V.; Cossi, M. Quantum Calculation of Molecular Energies and Energy Gradients in Solution by a Conductor Solvent Model. *J. Phys. Chem. A* **1998**, *102* (11), 1995–2001.

(51) Collman, J. P.; Barnes, C. E.; Brothers, P. J.; Collins, T. J.; Ozawa, T.; Gallucci, J. C.; Ibers, J. A. Oxidation of Ruthenium(II) and Ruthenium(III) Porphyrins. Crystal Structures of μ-Oxo-Bis[(p-Methylphenoxo)(Meso-Tetraphenylporphyrinato)- Ruthenium(IV)] and Ethoxo(Meso-Tetraphenylporphyrinato)-(Ethanol) Ruthenium(III)-Bisethanol. *J. Am.*

Chem. Soc. **1984**, *106* (18), 5151–5163.

(52) Hughes, T. F.; Friesner, R. A. Correcting Systematic Errors in DFT Spin-Splitting Energetics for Transition Metal Complexes. *J. Chem. Theory Comput.* **2011**, *7* (1), 19–32.

(53) Winkler, J. R.; Gray, H. B. Electronic Structures of Oxo-Metal Ions. *Struct. Bond.* **2012**, *142* (January), 17–28.

(54) Mayer, J. M. Metal-Oxygen Multiple Bond Lengths: A Statistical Study. *Inorg. Chem.* **1988**, *27* (22), 3899–3903.

(55) Holland, P. L. Metal-Dioxygen and Metal-Dinitrogen Complexes: Where Are the Electrons? *Dalt. Trans.* **2010**, *39* (23), 5415–5425.

(56) Gubelmann, M. H.; Williams, A. F. The Structure and Reactivity of Dioxygen Complexes of the Transition Metals. **1983**, 1–65.

(57) Askevold, B.; Khusniyarov, M. M.; Kroener, W.; Gieb, K.; Müller, P.; Herdtweck, E.; Heinemann, F. W.; Diefenbach, M.; Holthausen, M. C.; Vieru, V.; et al. Square-Planar Ruthenium(II) Complexes: Control of Spin State by Pincer Ligand Functionalization. *Chem. - A Eur. J.* **2015**, *21* (2), 579–589.

(58) Askevold, B.; Khusniyarov, M. M.; Herdtweck, E.; Meyer, K.; Schneider, S. A Square-Planar Ruthenium(II) Complex with a Low-Spin Configuration. *Angew. Chemie - Int. Ed.* **2010**, *49* (41), 7566–7569.

(59) Aldrich, K. E.; Odom, A. L. A Photochemical Route to a Square Planar, Ruthenium(Iv)-Bis(Imide). *Chem. Commun.* **2019**, *55* (30), 4403–4406.

(60) Romero, P. E.; Piers, W. E.; McDonald, R. Rapidly Initiating Ruthenium Olefin-

Metathesis Catalysts. *Angew. Chemie - Int. Ed.* **2004**, *43* (45), 6161–6165.

(61) Sanford, M. S.; Henling, L. M.; Day, M. W.; Grubbs, R. H. Ruthenium-Based Four-Coordinate Olefin Metathesis Catalysts. *Angew. Chemie - Int. Ed.* **2000**, *39* (19), 3451–3453.

(62) Khan, M. M. T.; Mizra, S. A.; Shaikh, Z. A.; Sreelatha, C.; Paul, P.; Shukla, R. S.; Srinivas, D.; Rao, A. P.; Abdi, S. H. R.; Bhatt, S. D.; et al. Dioxygen Affinities of Some Ruthenium(III) Schiff Base Complexes. *Polyhedron* **1992**, *11* (14), 1821–1827.

(63) Prakash, R.; Ramachandraiah, G. Ruthenium(III)-Aminopolycarboxylato Complexes Active for the Reduction of the N-N Bond of Hydrazine and Phenylhydrazine in Aqueous Acidic Media. *J. Chem. Soc. Dalt. Trans.* **2000**, No. 1, 85–92.

(64) Walters, M. A.; Vapnyar, V.; Bolour, A.; Incarvito, C.; Rheingold, A. L. Iron(III) Nitrilotriacetate and Iron(III) Iminodiacetate, Their X-Ray Crystallographic Structures and Chemical Properties. *Polyhedron* **2003**, *22* (7), 941–946.

(65) Walters, M. A.; Chaparro, J.; Siddiqui, T.; Williams, F.; Ulku, C.; Rheingold, A. L. The Formation of Disulfides by the [Fe(Nta)Cl2]2- Catalyzed Air Oxidation of Thiols and Dithiols. *Inorganica Chim. Acta* **2006**, *359* (12), 3996–4000.

(66) Barnard, N. I.; Visser, H. G. Novel Synthetic Method for Cobalt Complexes: Structural and Kinetic Study of [Co(Nta)(Py)(H2O)]. *Inorg. Chem. Commun.* **2012**, *15*, 40–42.

(67) Frisch, M. J.; Trucks, G. W.; Schlegel, H. B.; Scuseria, G. E.; Robb, M. A.; Cheeseman, J. R.; Scalmani, G.; Barone, V.; Petersson, G. A.; Nakatsuji, H.; et al. Gaussian 09. Gaussian Inc.: Wallingford CT 2016.

(68) Frisch, E. Dennington, R.D., Keith, T.A., Millam, J. GaussView 4 Reference. Semichem Inc.: Shawnee Mission, KS 2007.

(69) Legault, C. Y. CYLview. CYL Lab 2019.

(70) Zhao, Y.; Truhlar, D. G. The M06 Suite of Density Functional s for Main Group Thermochemistry, Thermochemical Kinetics, Noncovalent Interactions, Excited States, and Transition Elements: Two New Functi Onals and Systematic Testing of Four M06 Functionals and Twelve Other Function. *Theor. Chem. Acc.* **2008**, *120* (1), 215–241.

(71) Shoair, A. G. F. A Novel Method for Preparing of Oxoruthenates Complexes: Trans-[RuO 3(OH)2]2-, [RuO4]-, (n-Pr4N)+[RuO4]- and [RuO 4] and Their Use as Catalytic Oxidants. *Bull. Korean Chem. Soc.* **2005**, *26* (10), 1525–1528.

(72) Mercer, E. E.; Buckley, R. R. Hexaaquoruthenium (II). *Inorg. Chem.* **1965**, *4* (12), 1692–1695.

IV. APPENDIX

Experimental Data

$(Pr)_4N^+[RuO_4]^-$:

Product IR

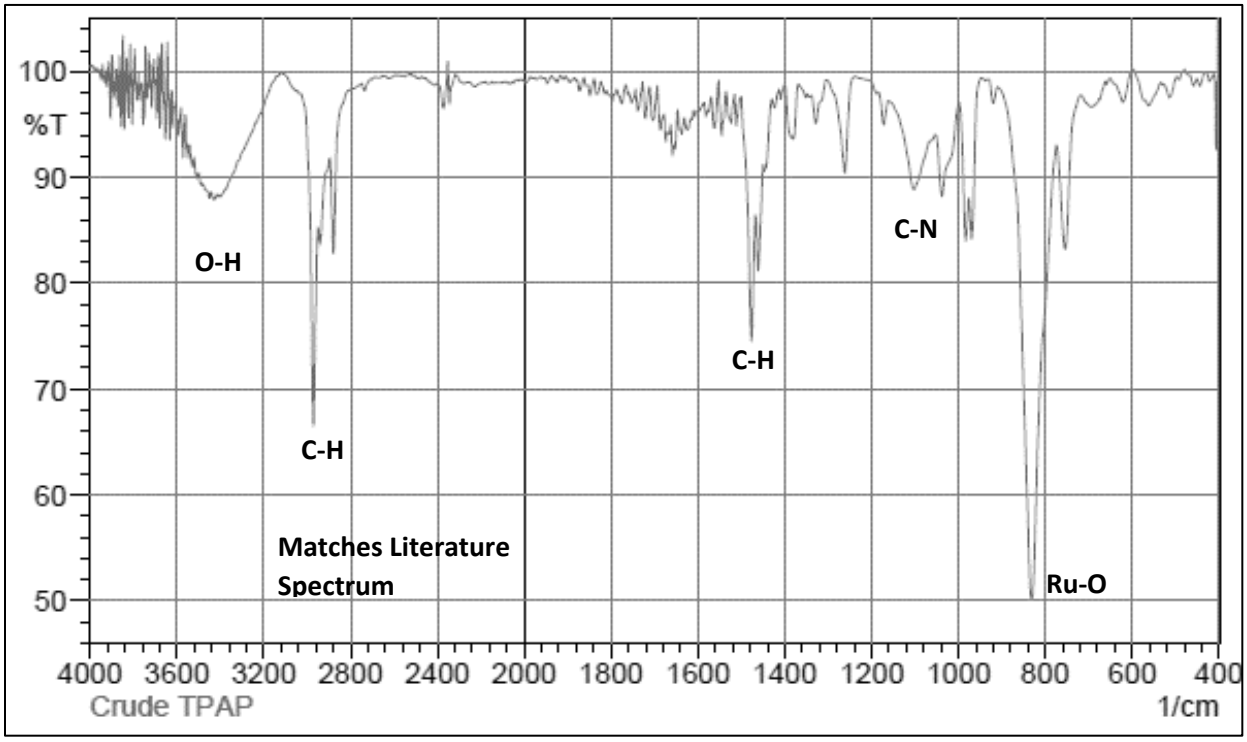

Product UV-Vis

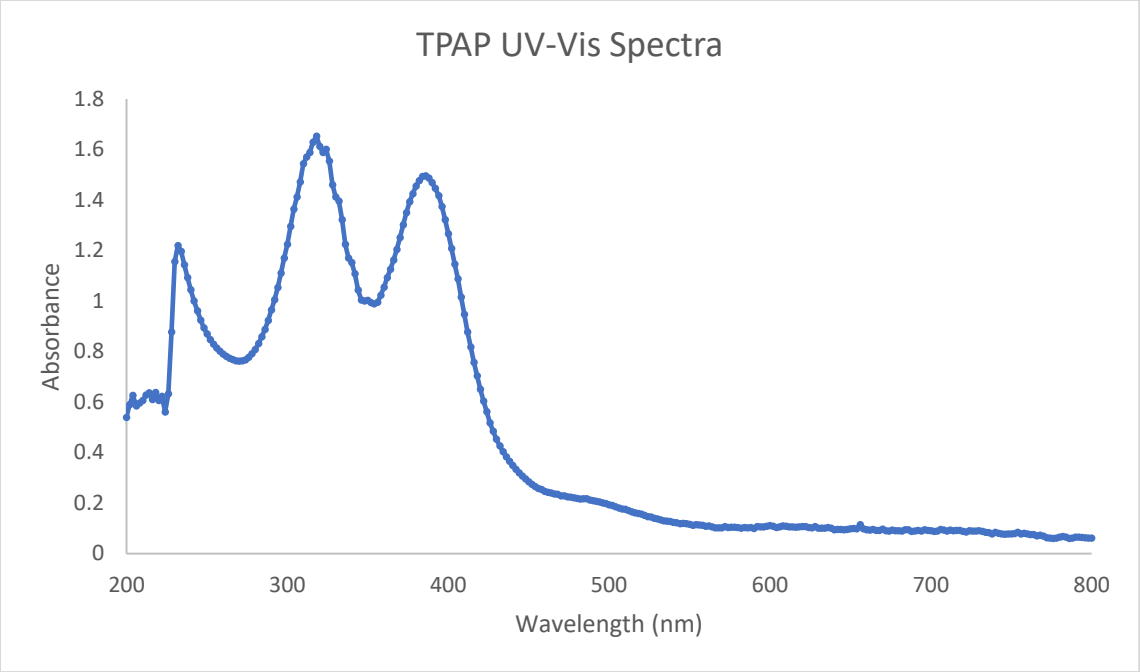

$(Pr)_4N^+[(C_6H_{10}O_3)_2RuO]^-$:

Product IR

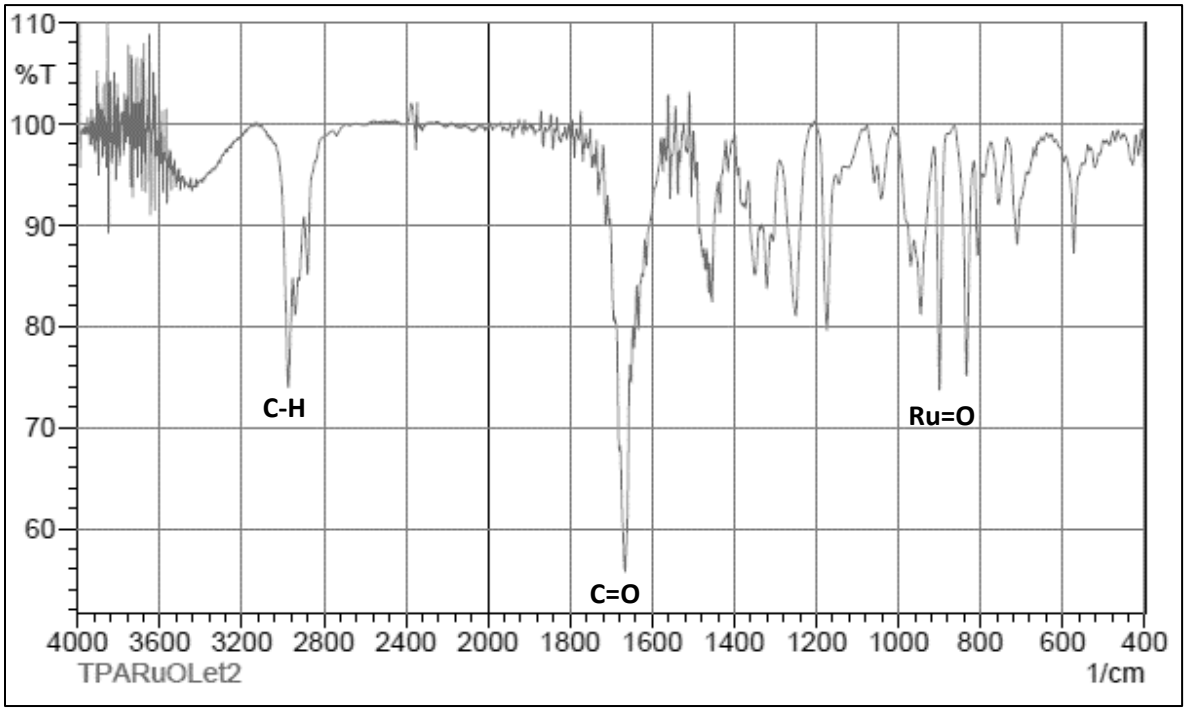

Product Positive Ion ESI

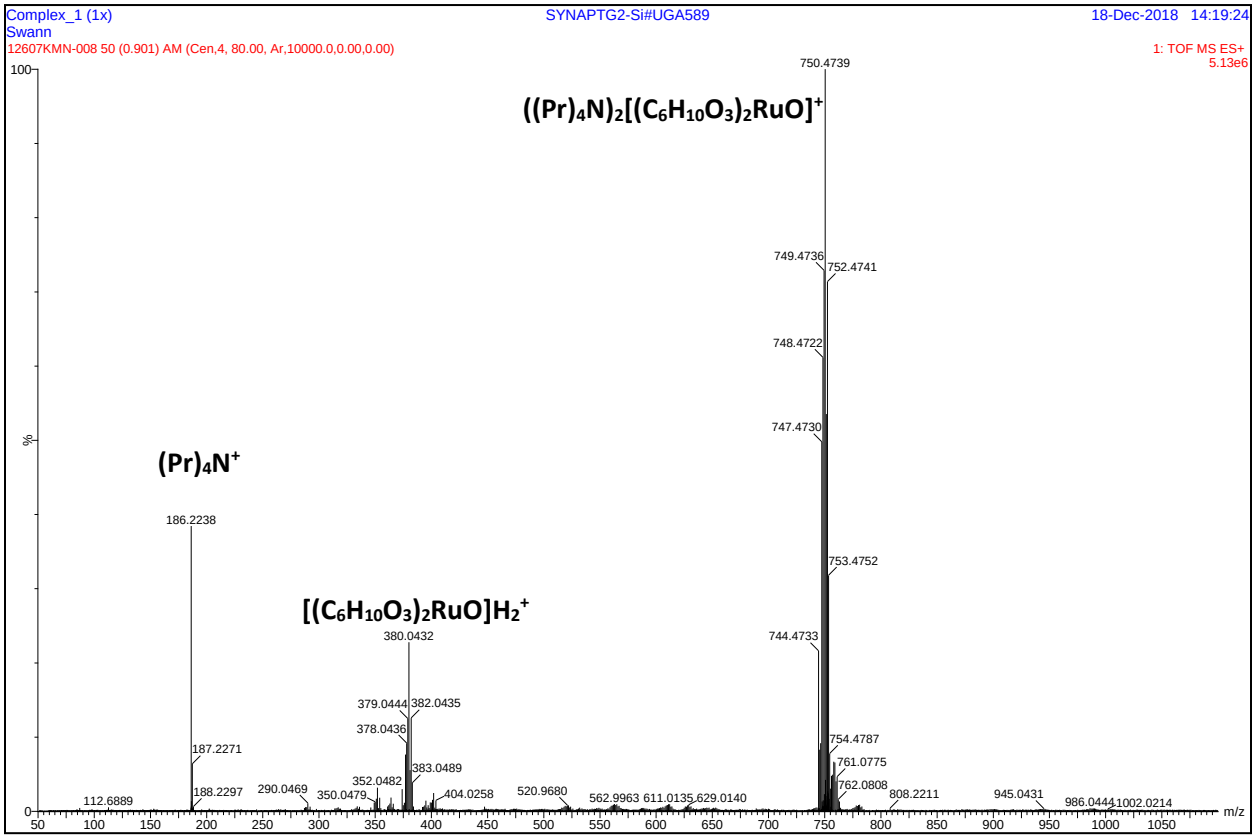

Product Negative Ion ESI

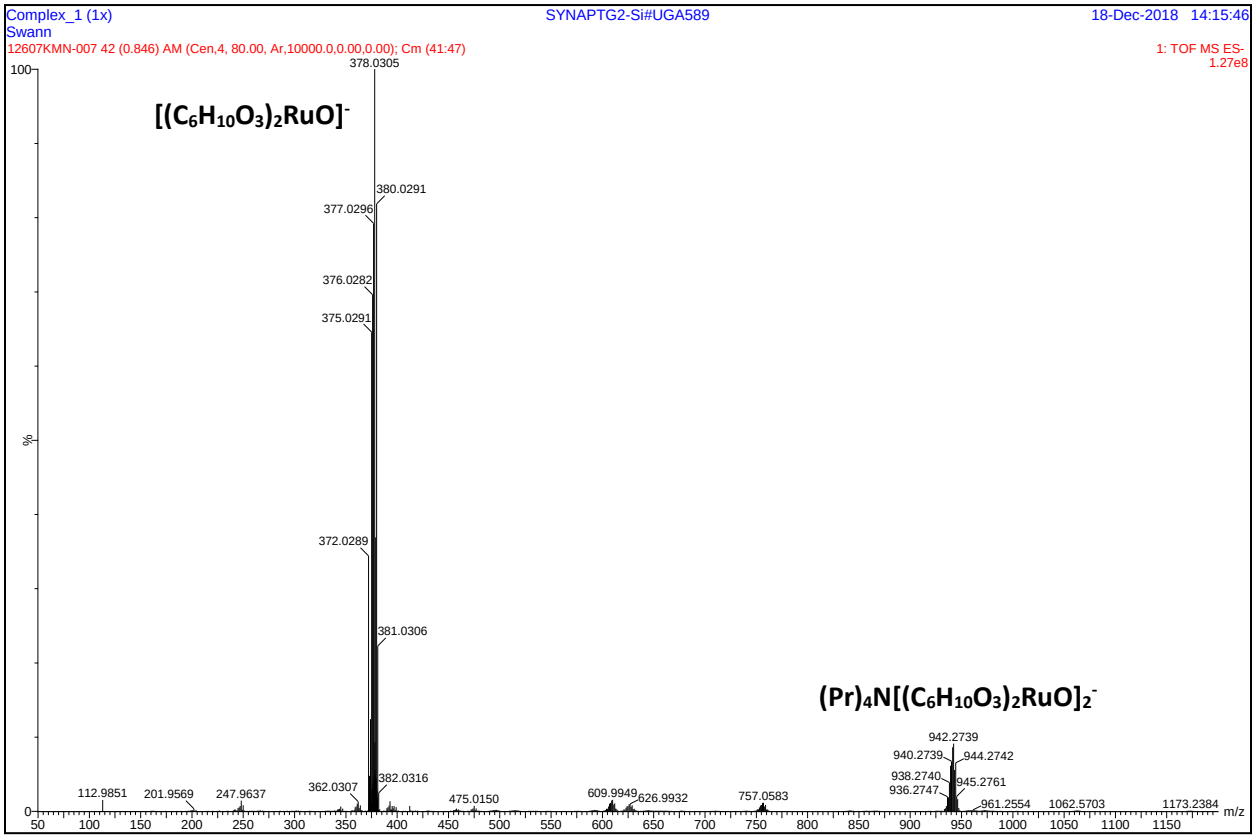

Trial 1 NTARu Synthesis:

Precipitate IR

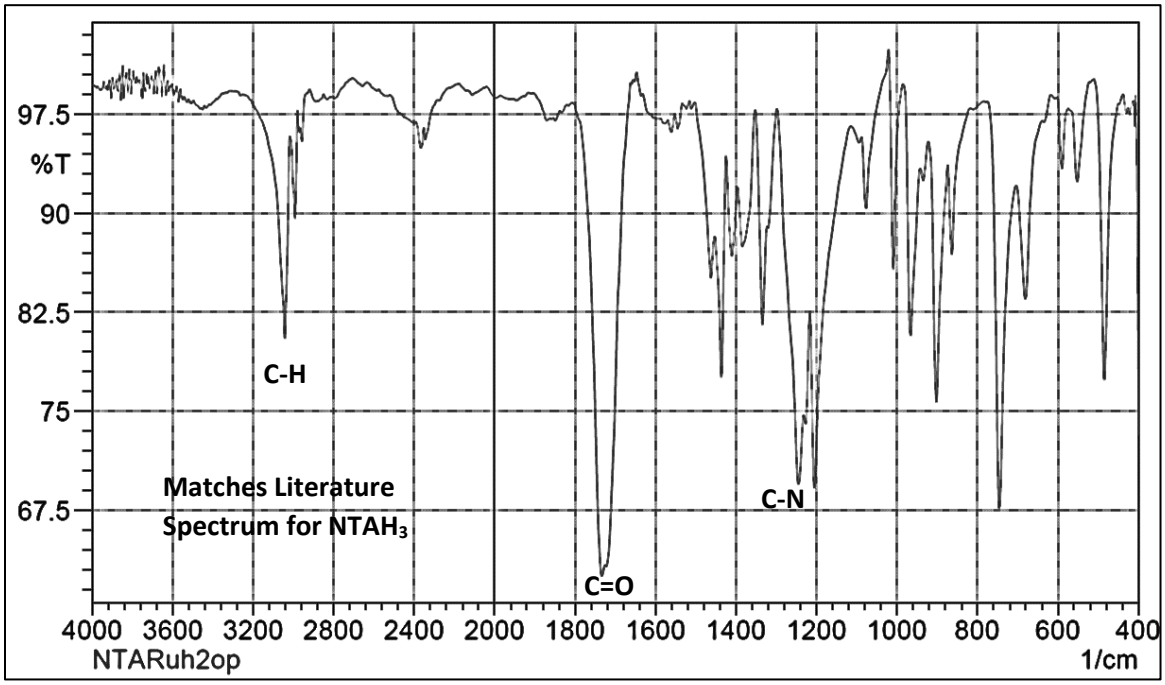

Filtrate IR

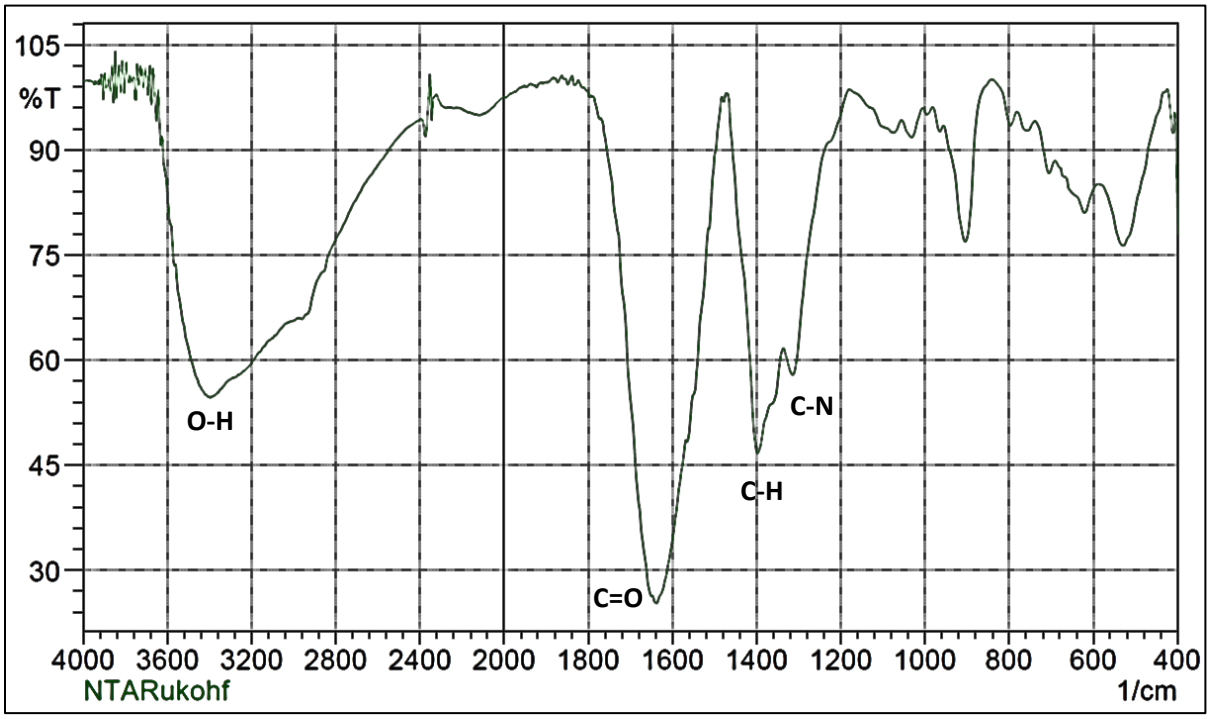
105
%T
90
75
60
45
30
O-H
C=O
C-H
C-N
4000 3600 3200 2800 2400 2000 1800 1600 1400 1200 1000 800 600 400
NTARukohf
1/cm

Filtrate Positive Ion ESI

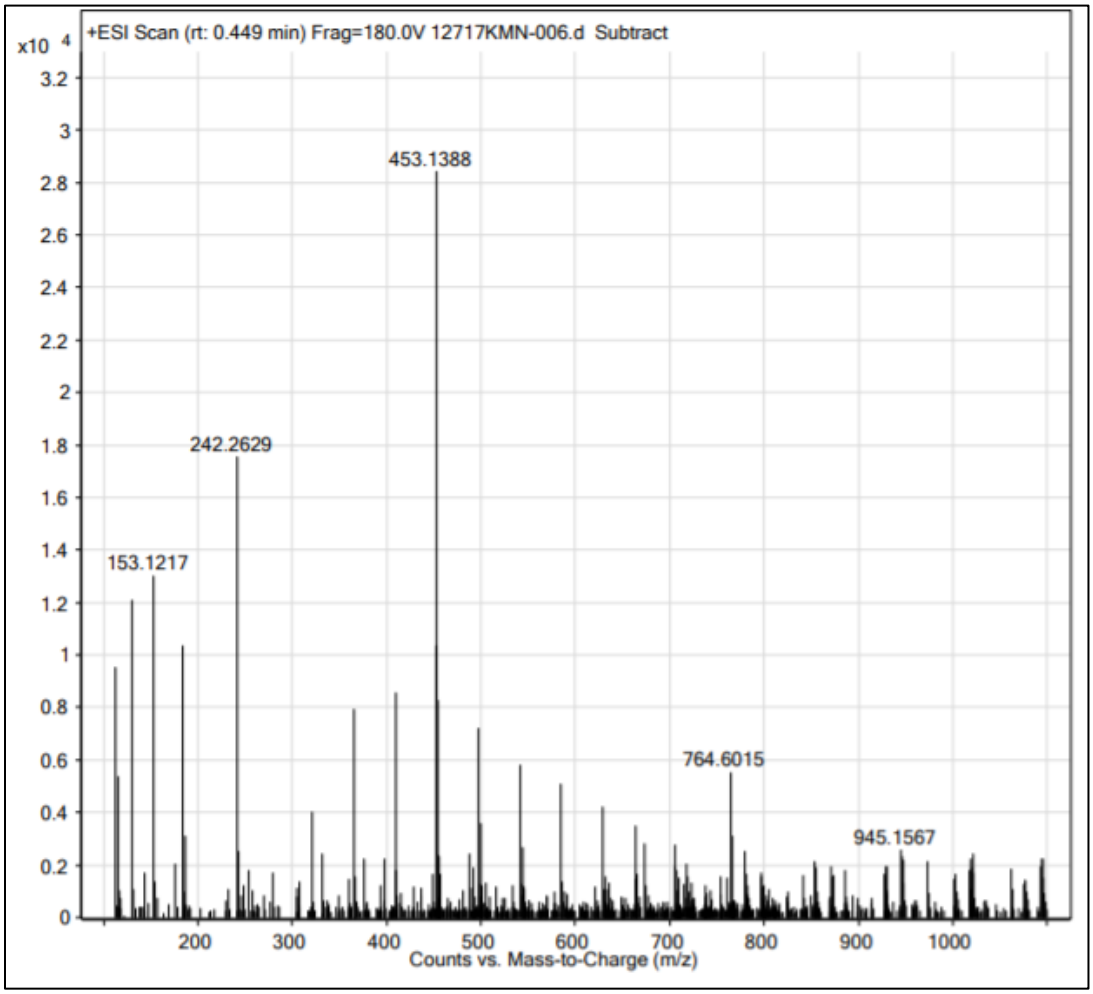

Filtrate Negative Ion ESI

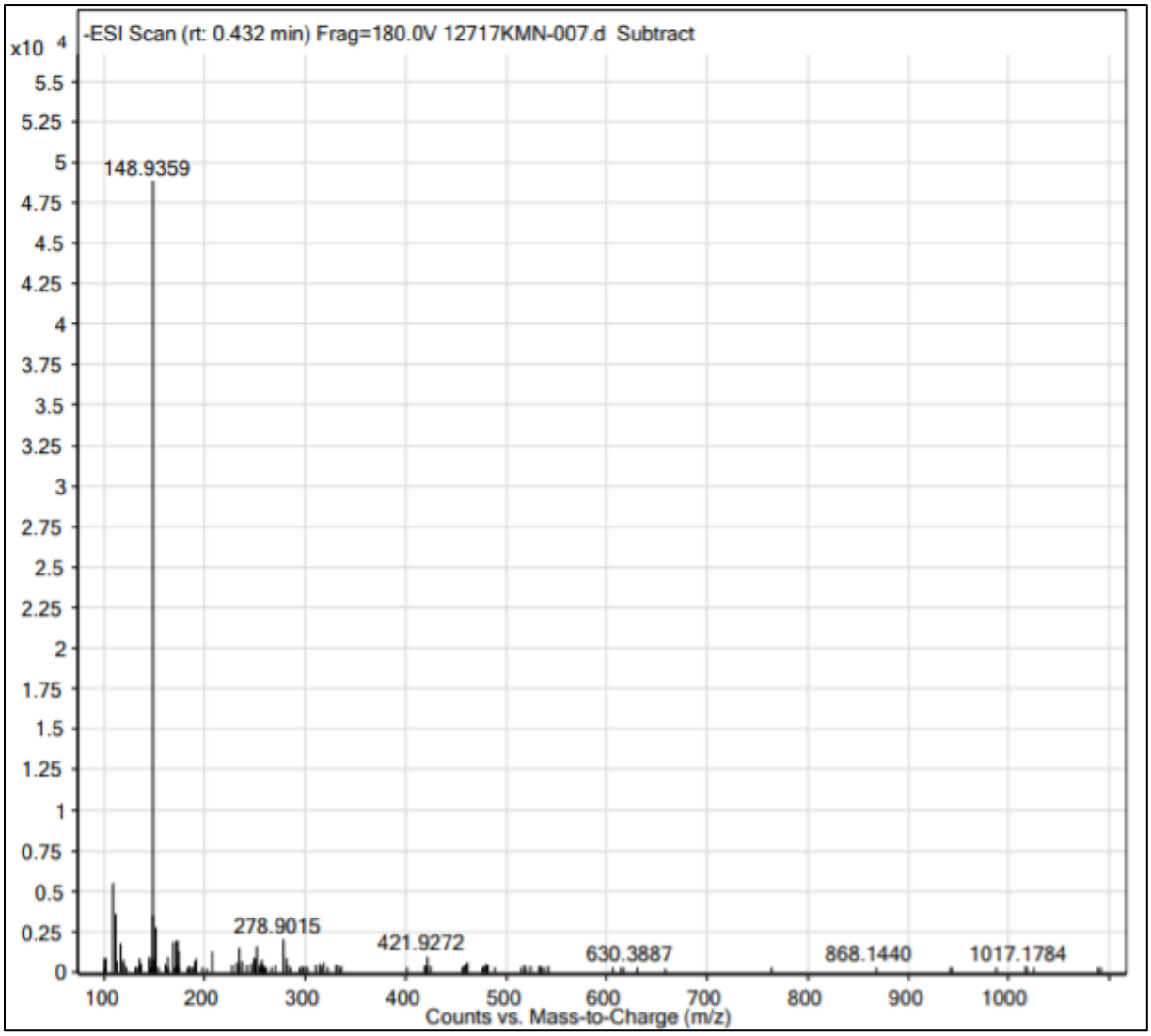

Trial 2:

Precipitate IR

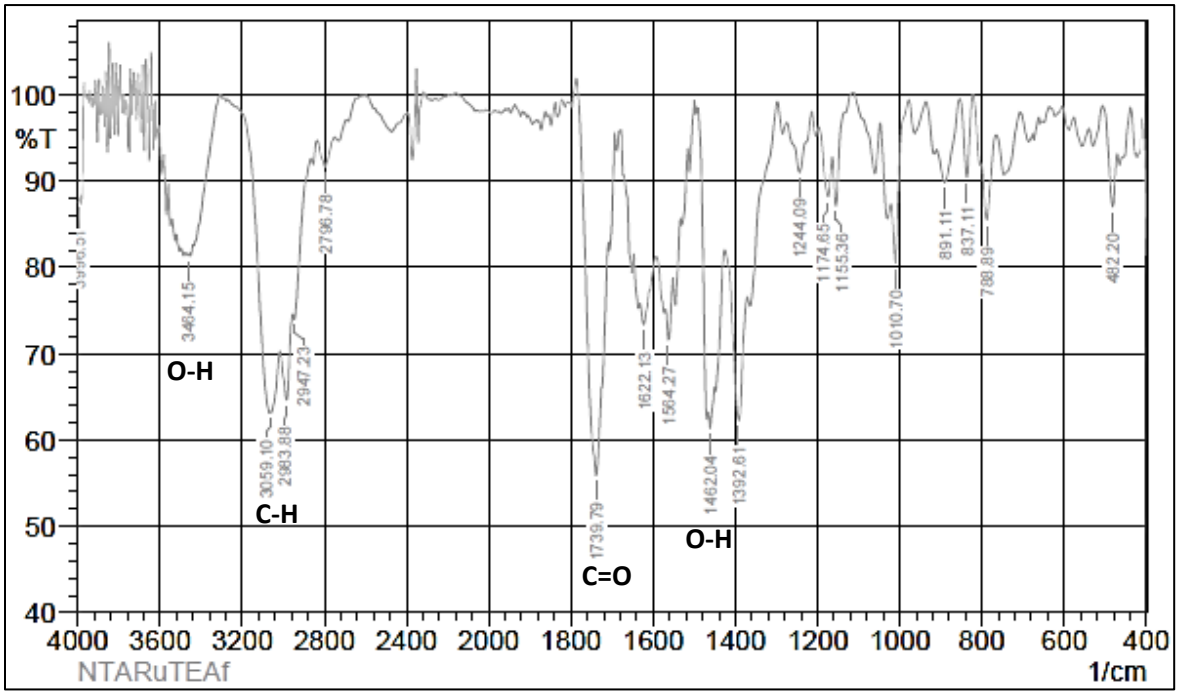

Filtrate Positive Ion ESI

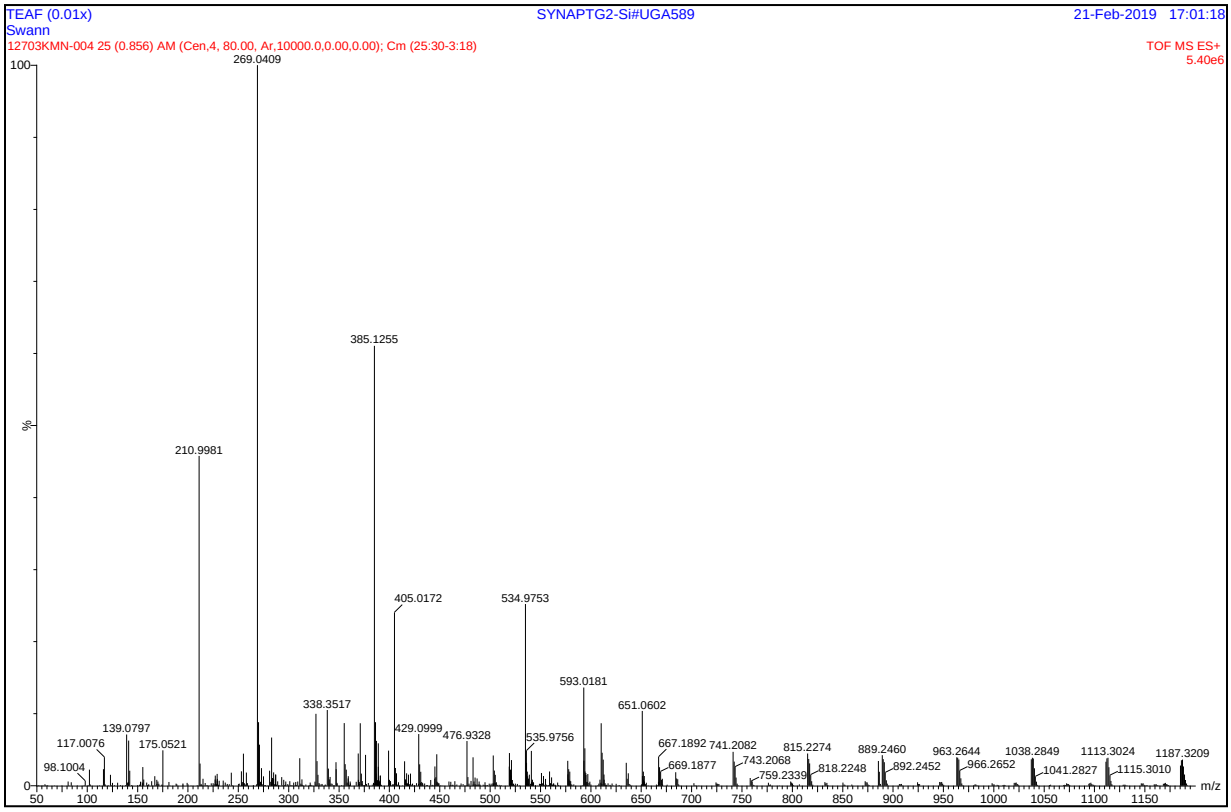

Filtrate Negative Ion ESI

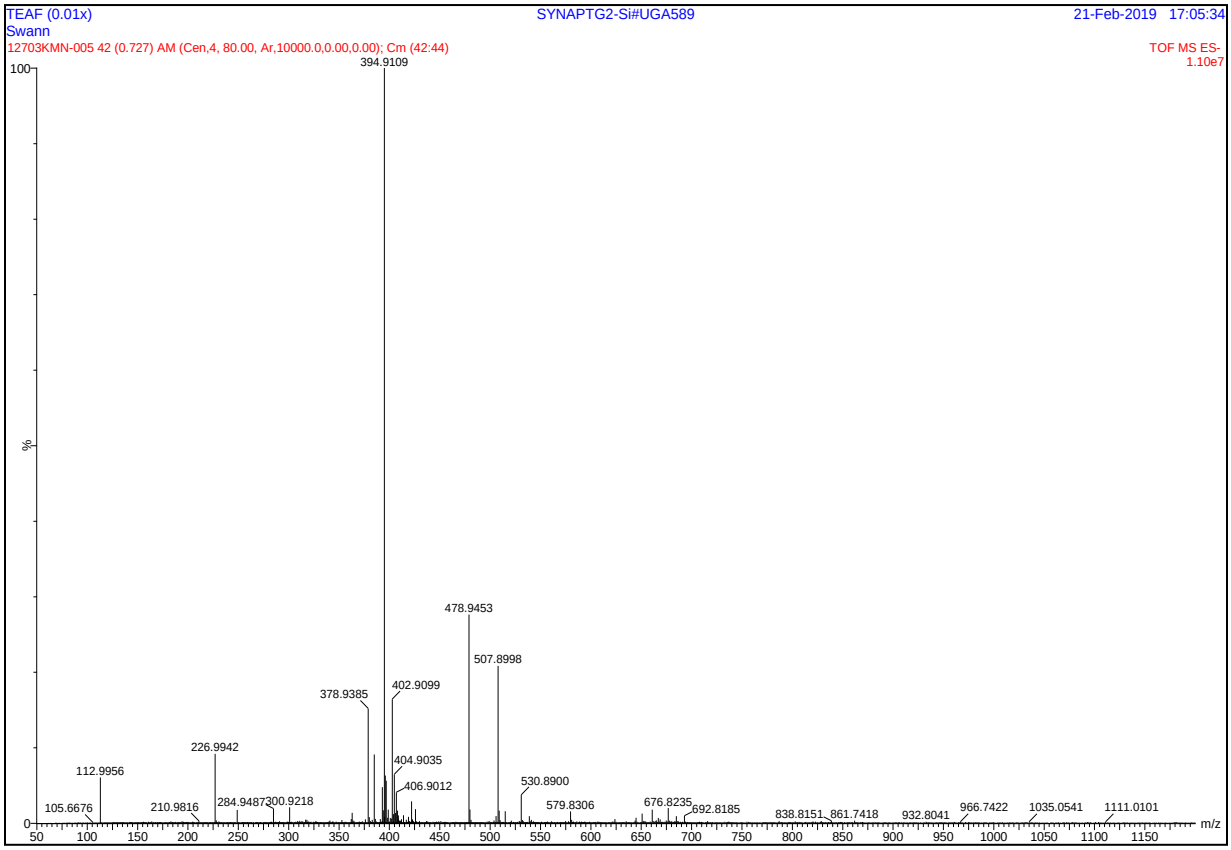

Trial 3:

Precipitate IR

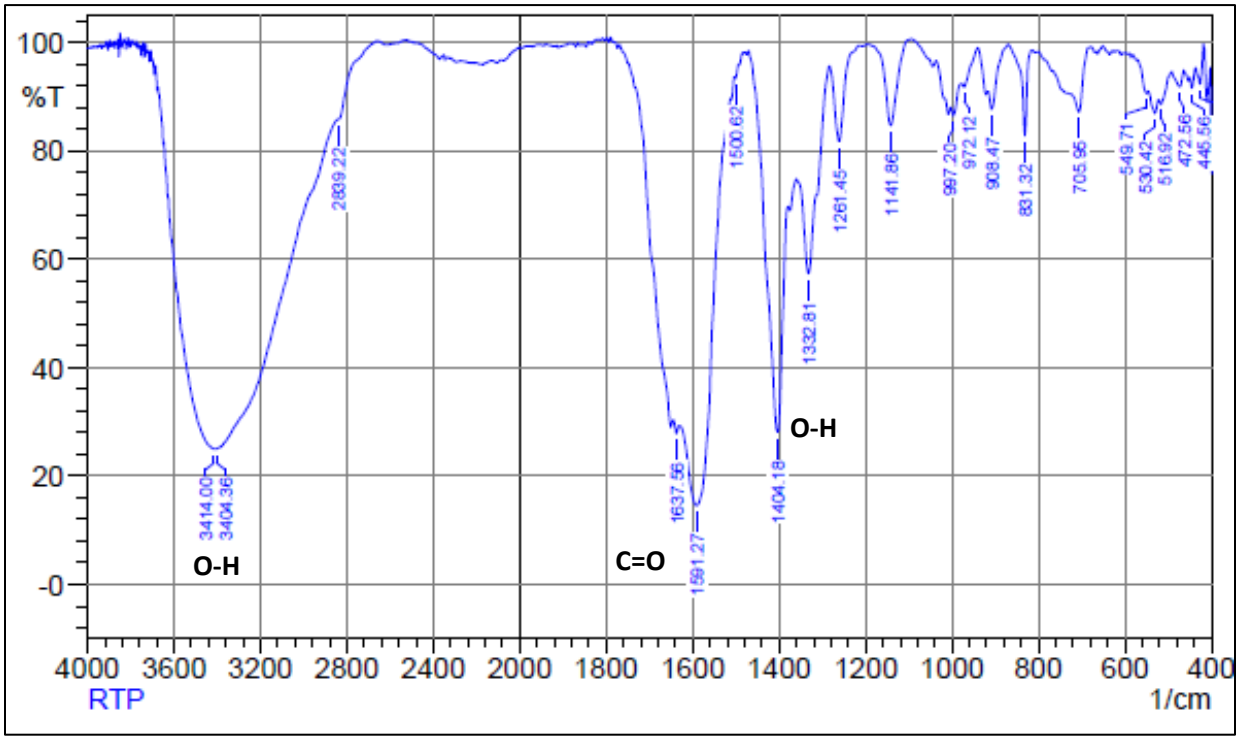

Filtrate IR

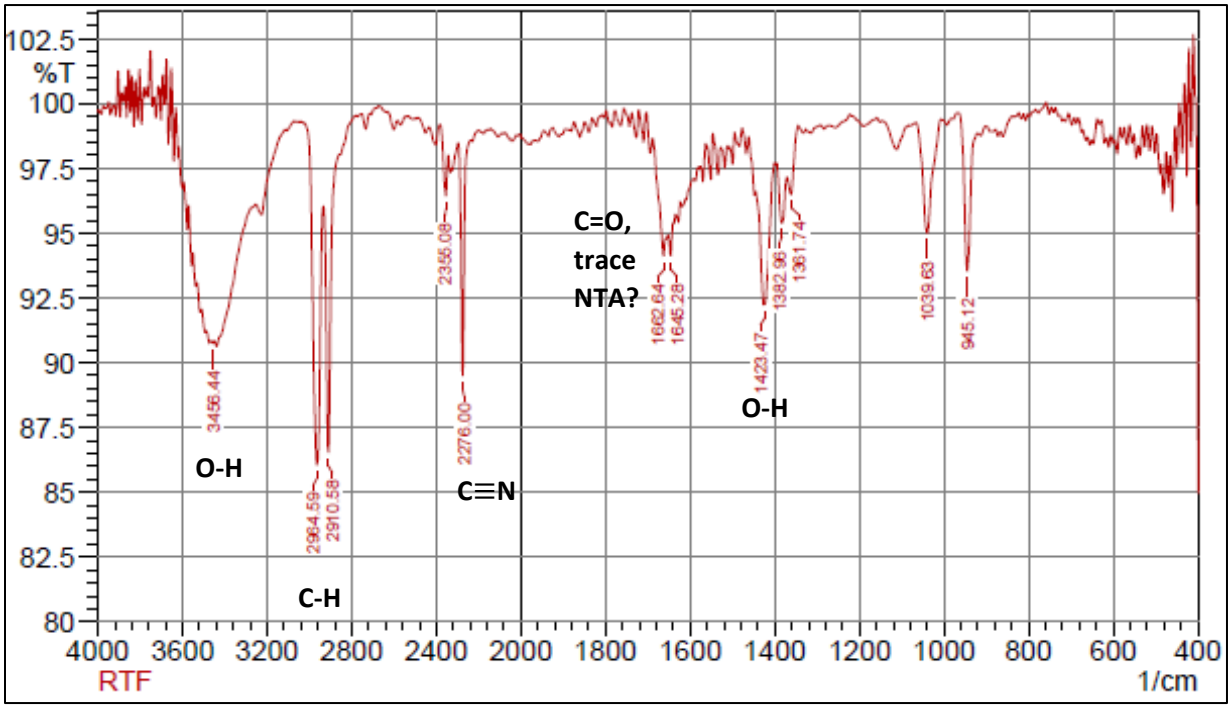
102.5
%T
100
97.5
95
92.5
90
87.5
85
82.5
80
4000 3600 3200 2800 2400 2000 1800 1600 1400 1200 1000 800 600 400
RTF
1/cm
3456.44
2964.59
2910.58
2355.08
2276.00
1662.64
1645.28
1423.47
1382.96
1361.74
1039.63
945.12
O-H
C-H
C≡N
C=O,
trace
NTA?
O-H

Trial 4:

Precipitate IR

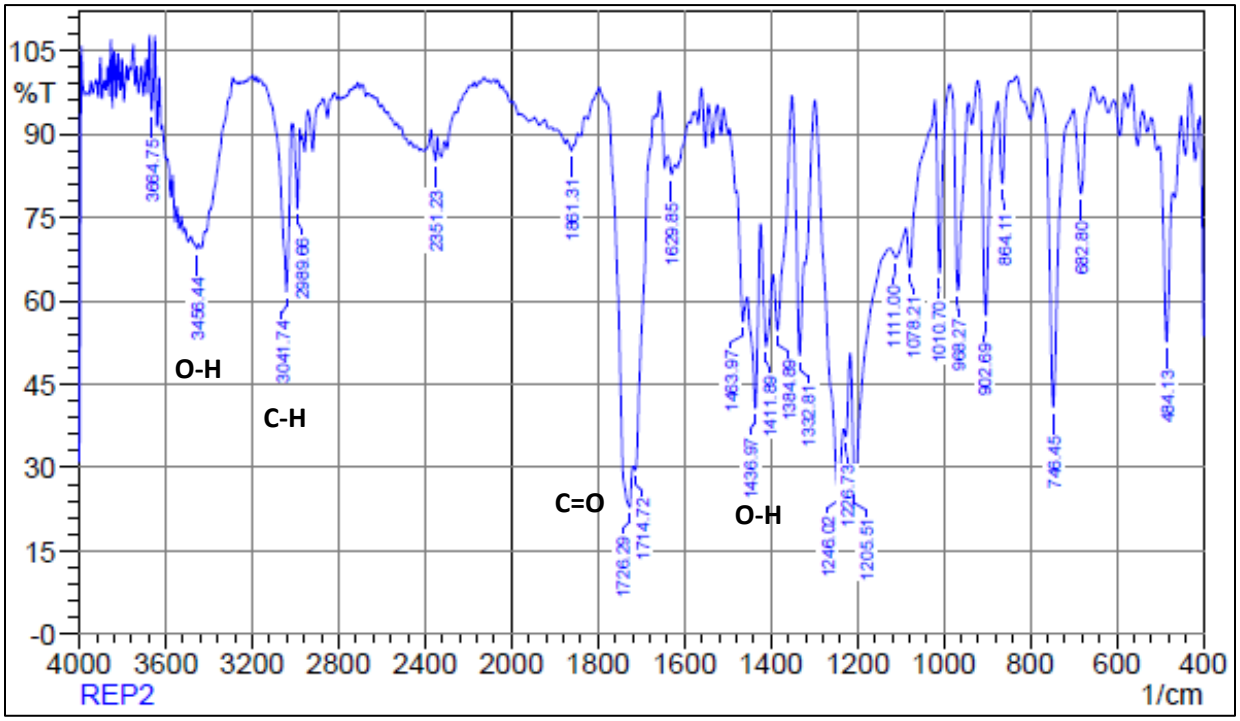

Filtrate IR

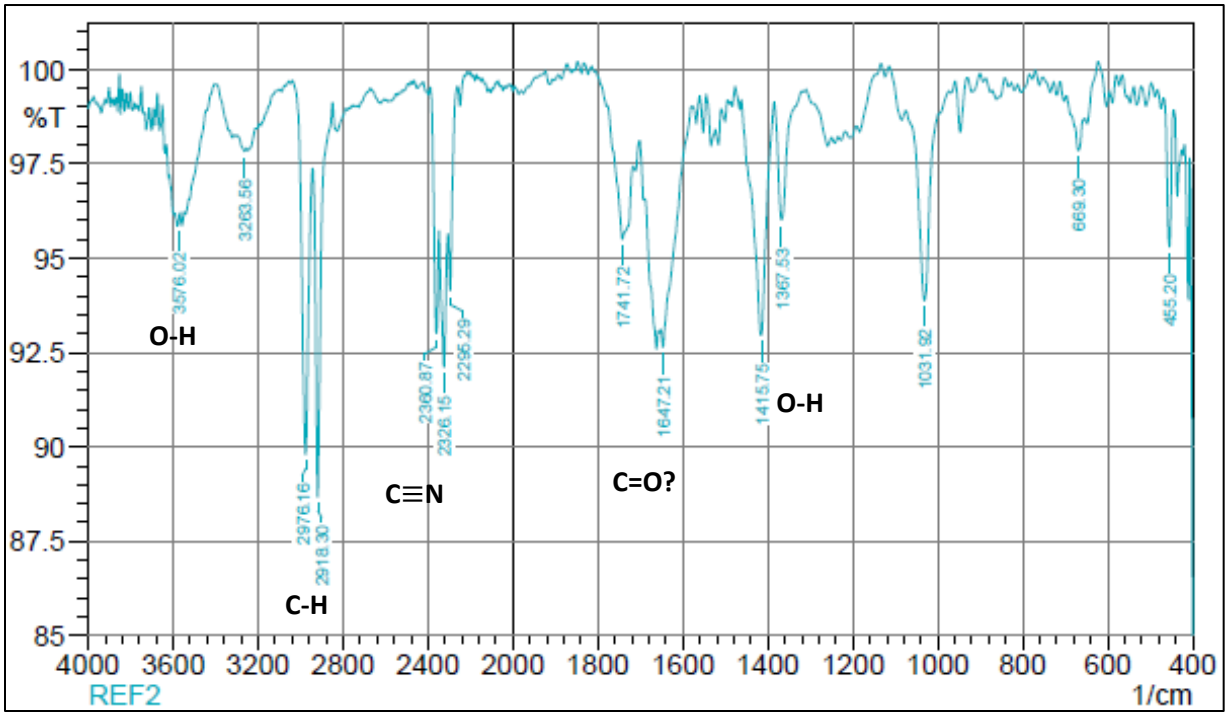
100
%T
97.5
95
92.5
90
87.5
85
4000 3600 3200 2800 2400 2000 1800 1600 1400 1200 1000 800 600 400
REF2
1/cm
3576.02
3263.56
2976.16
2918.30
2360.87
2326.15
2296.29
1741.72
1647.21
1415.75
1367.53
1031.92
669.30
455.20
O-H
C-H
C≡N
C=O?
O-H

Filtrate Positive Ion ESI

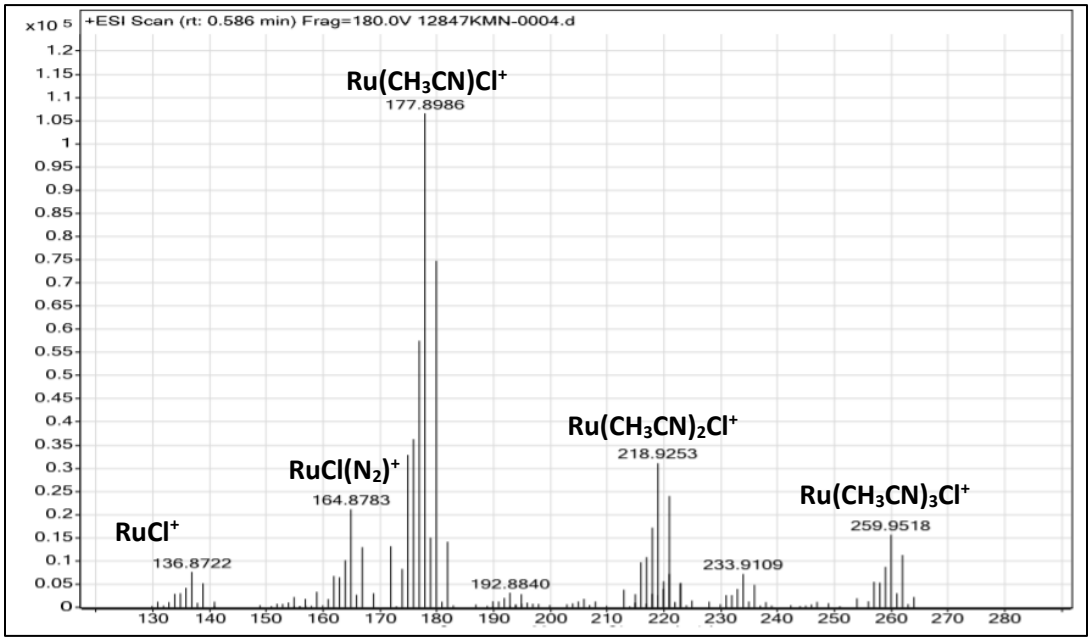

Filtrate Negative Ion ESI

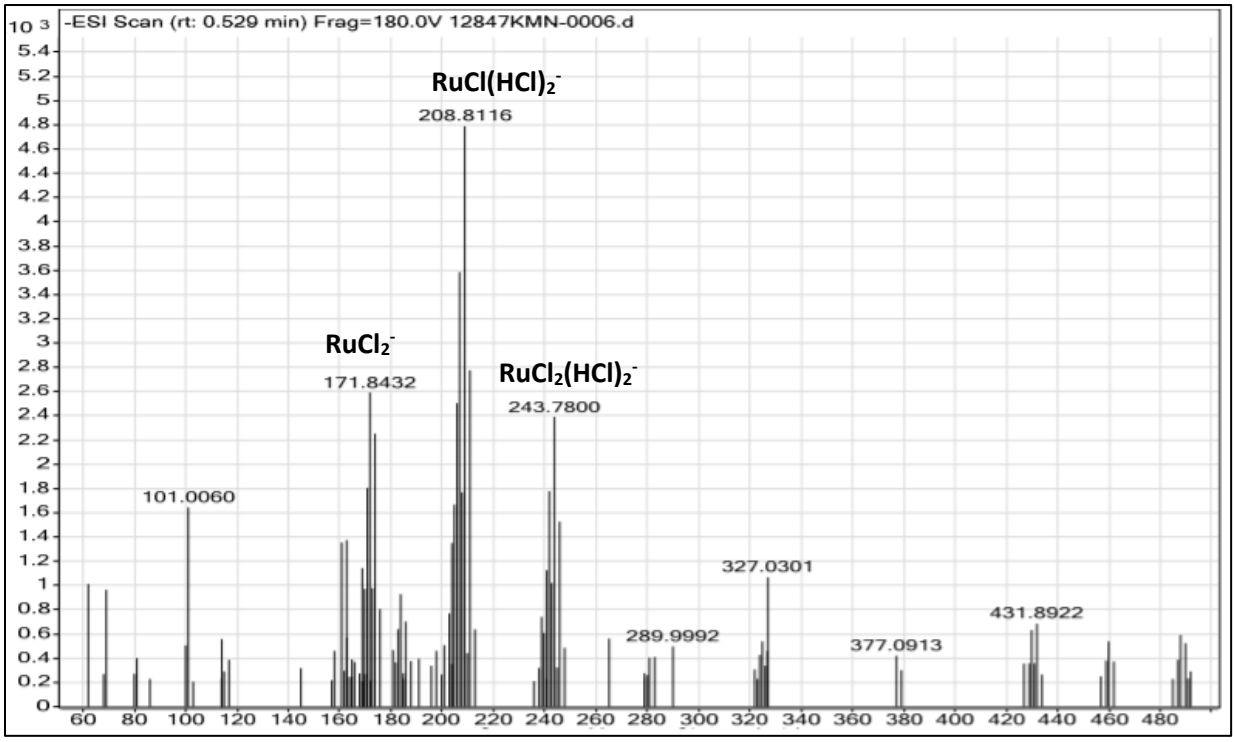

Trial 5:

Precipitate IR

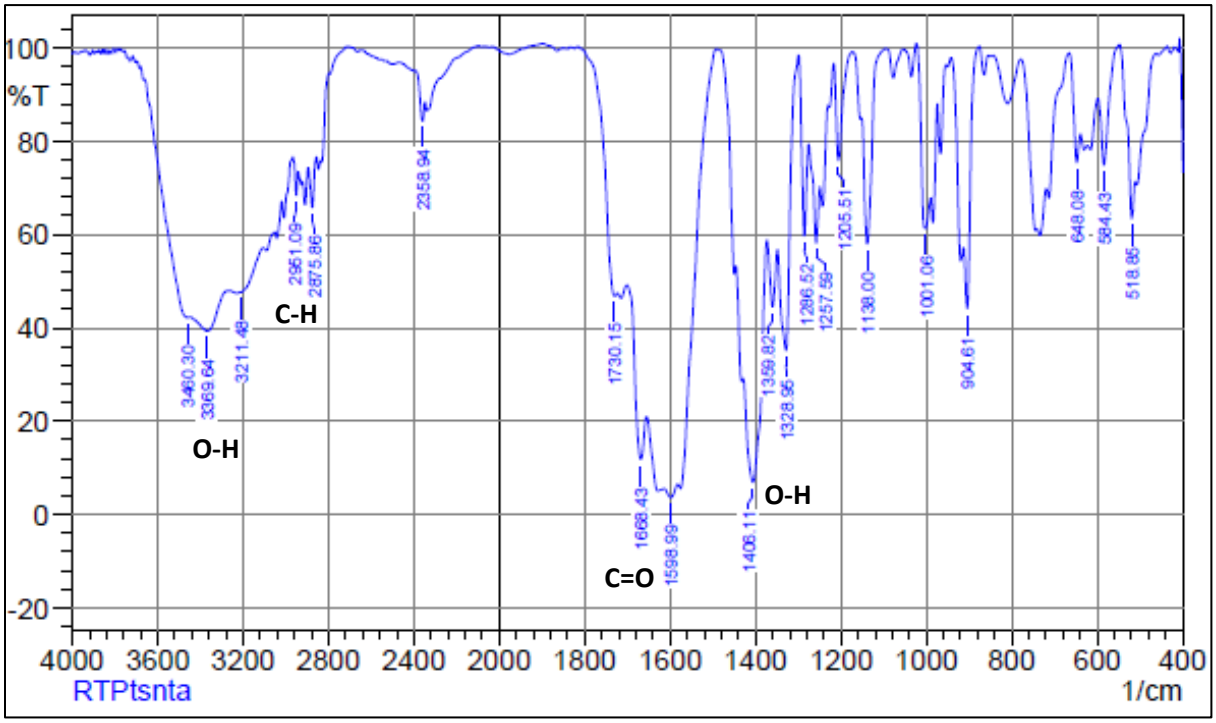

Filtrate IR

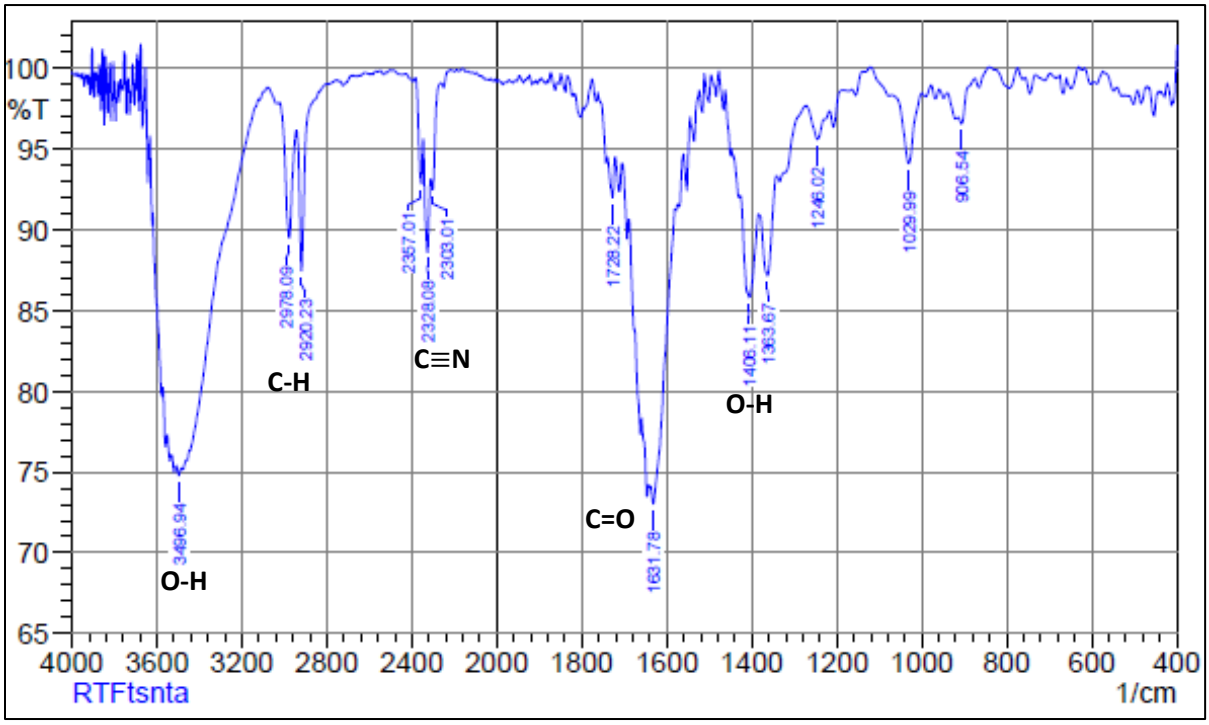
100
%T
95
90
85
80
75
70
65
4000
3600
3200
2800
2400
2000
1800
1600
1400
1200
1000
800
600
400
1/cm
RTFtsnta
3466.94
2978.09
2920.23
2357.01
2328.08
2303.01
1728.22
1631.78
1406.11
1363.67
1246.02
1029.99
906.54
O-H
C-H
C≡N
C=O
O-H

Trial 6:

Precipitate IR Spectrum

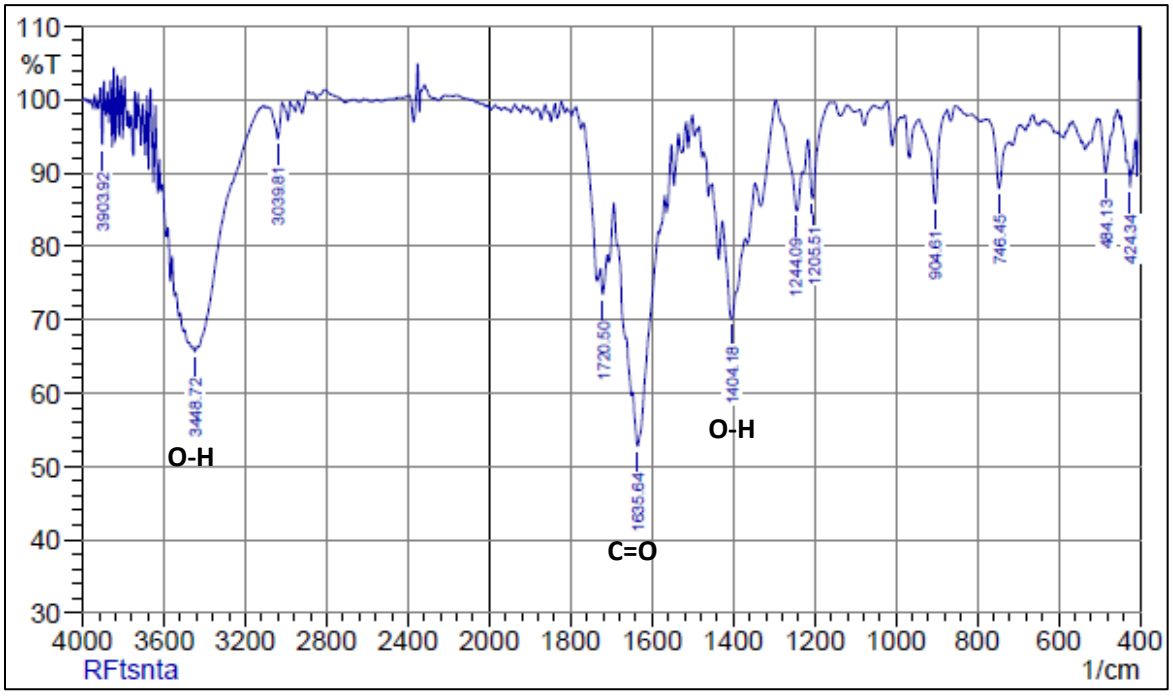

Filtrate IR Spectrum

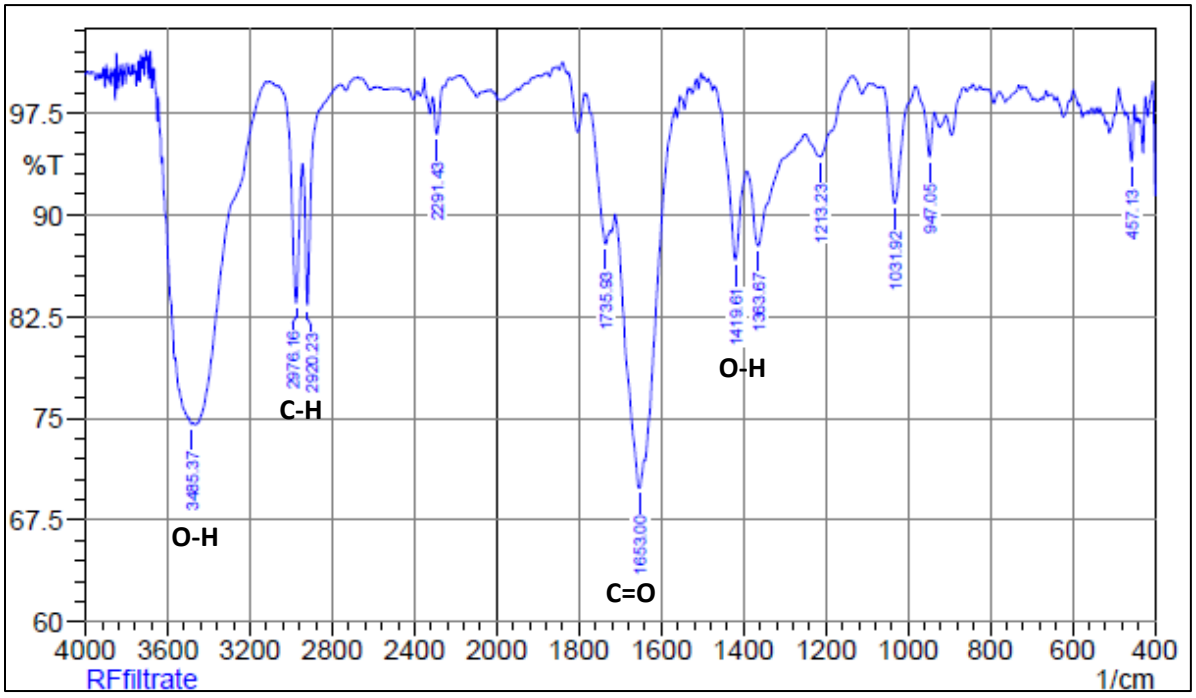

Filtrate Positive Ion ESI

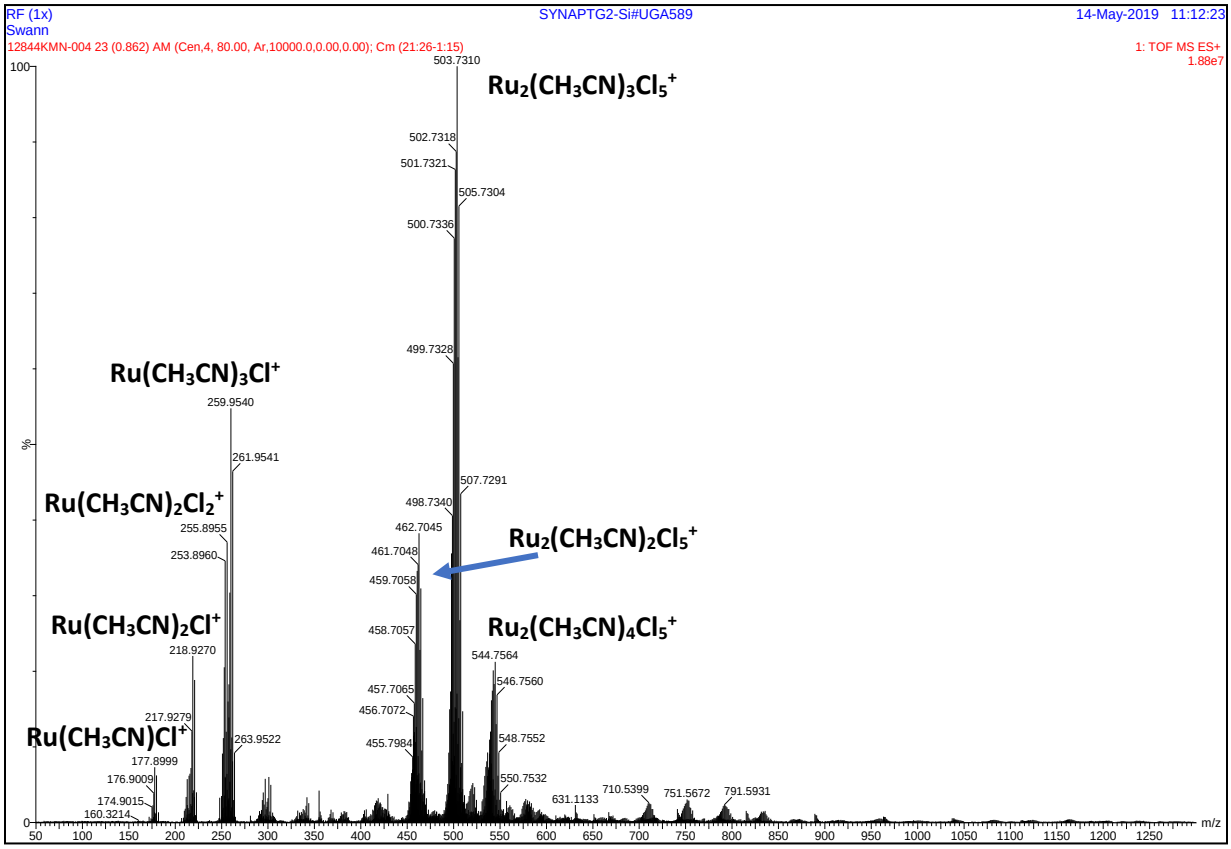

Trial 7:

Crude Product IR

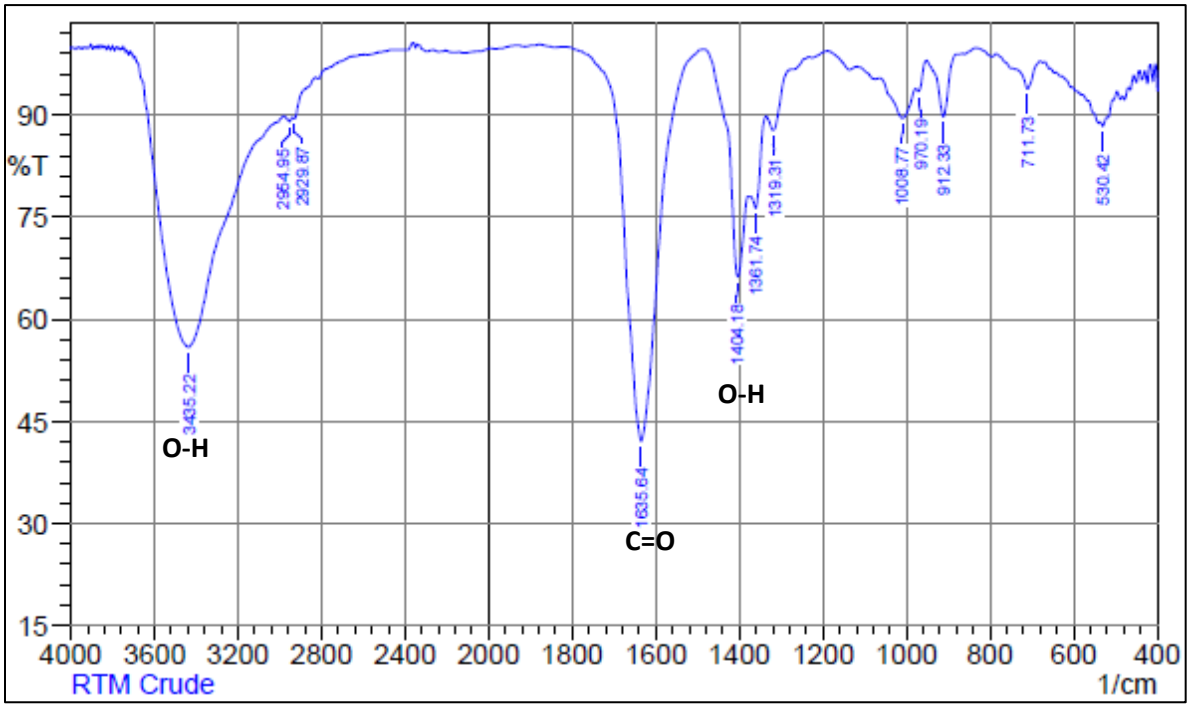

Crude Product Positive Ion ESI

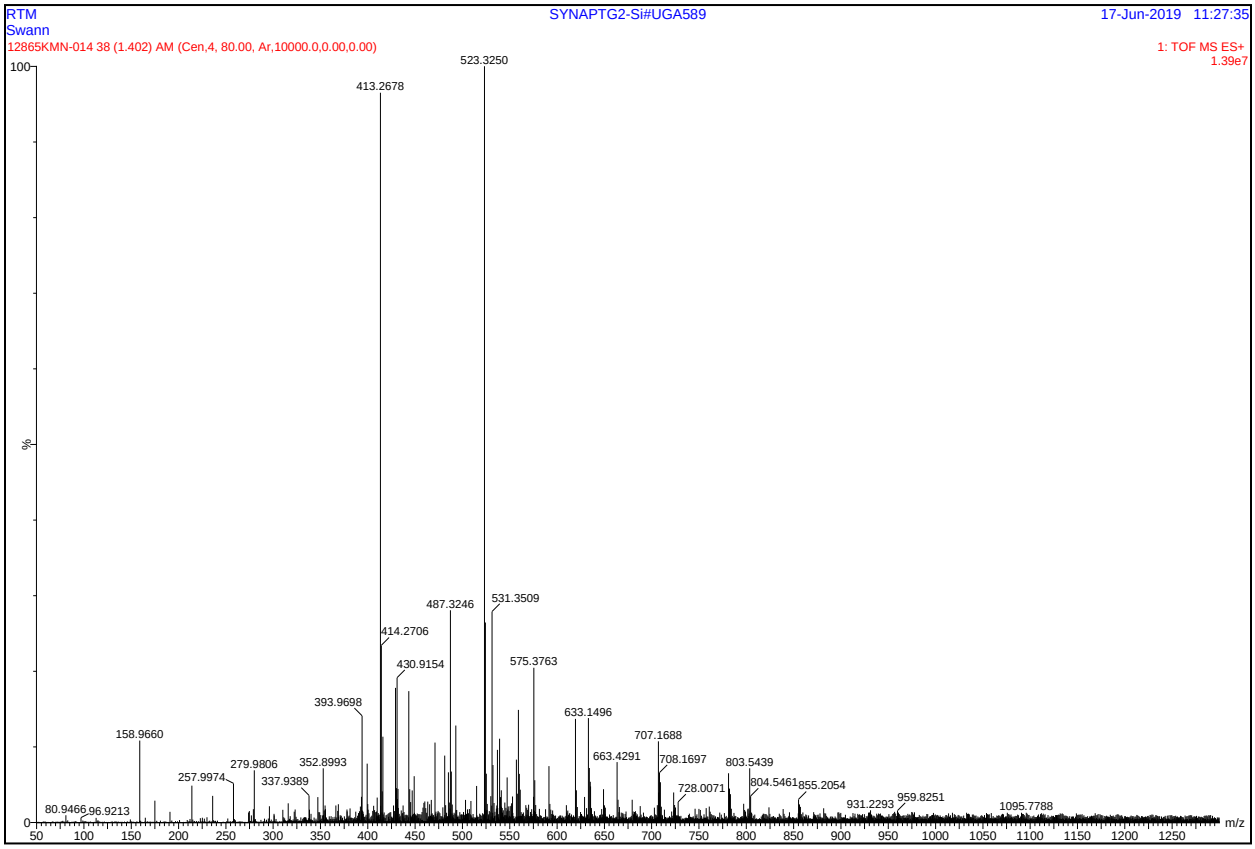

Trial 8:

Precipitate IR

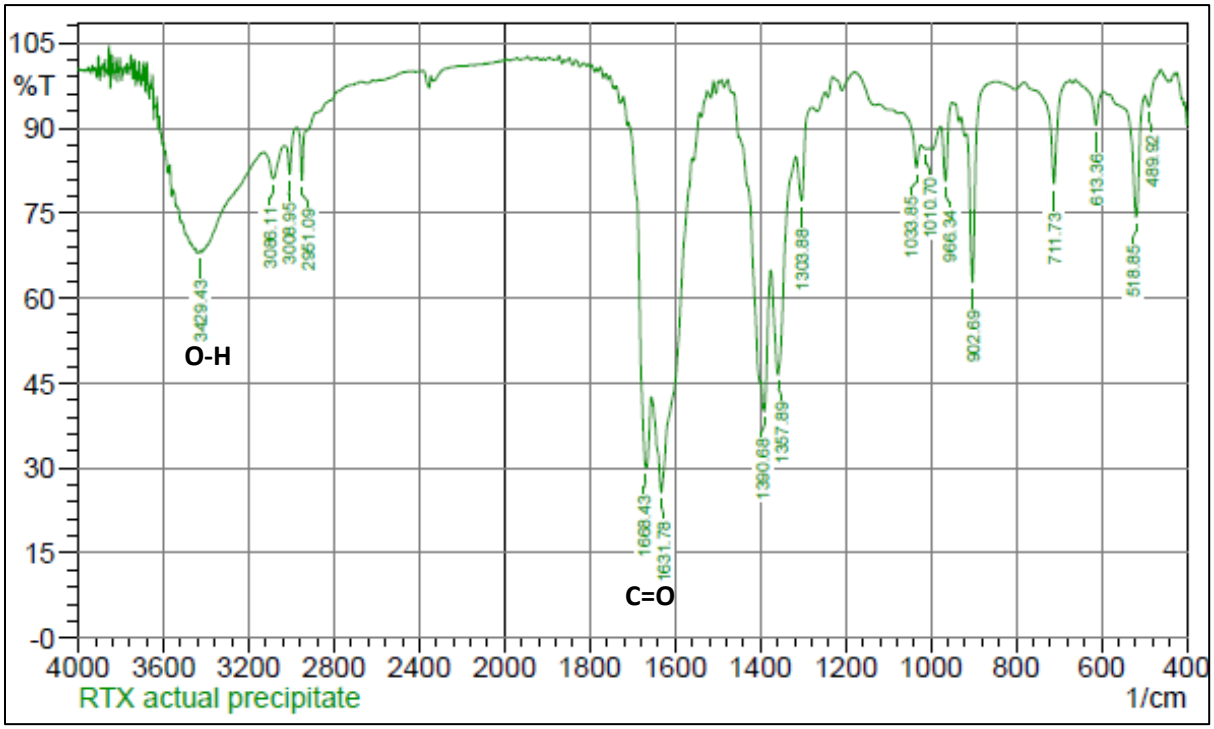

Filtrate IR

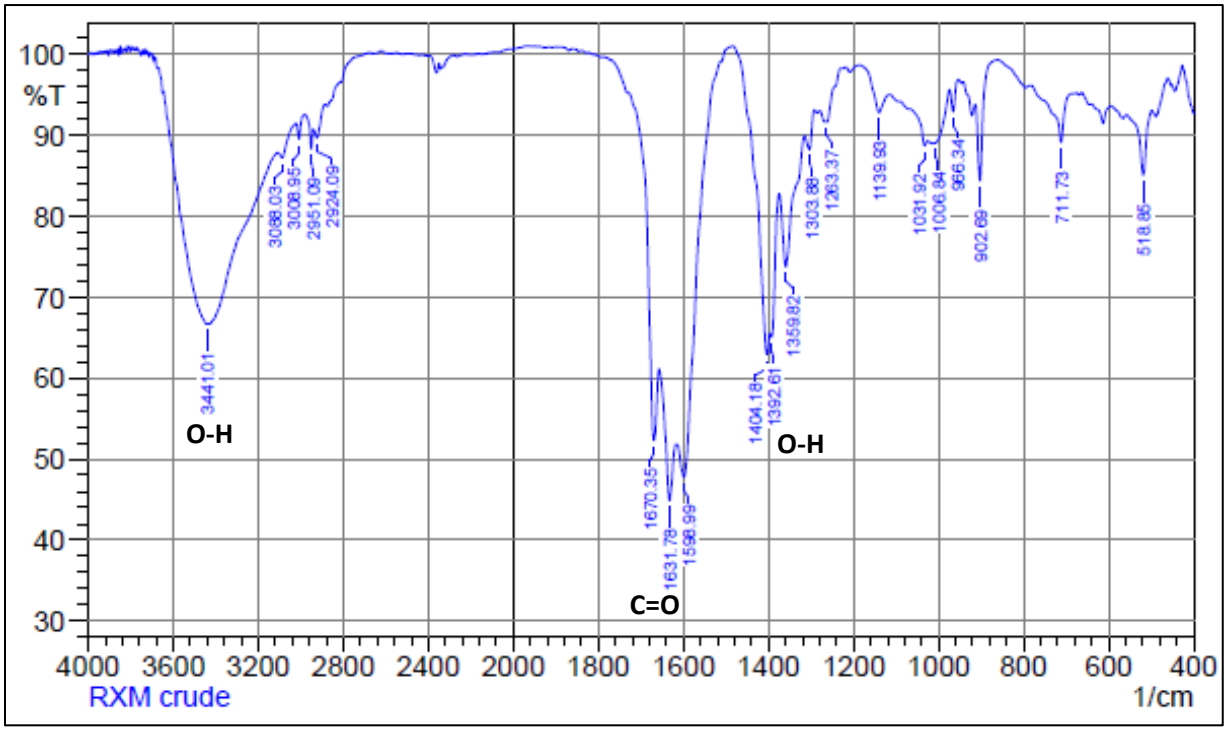
100
%T
90
80
70
60
50
40
30
4000 3600 3200 2800 2400 2000 1800 1600 1400 1200 1000 800 600 400
1/cm
RXM crude
3441.01
O-H
3088.03
3008.95
2951.09
2924.09
1670.35
1631.78
1598.99
C=O
1404.18
1392.61
1359.82
1303.88
1263.37
O-H
1139.93
1031.92
1006.84
966.34
902.89
711.73
518.85

Crude Product Positive Ion ESI

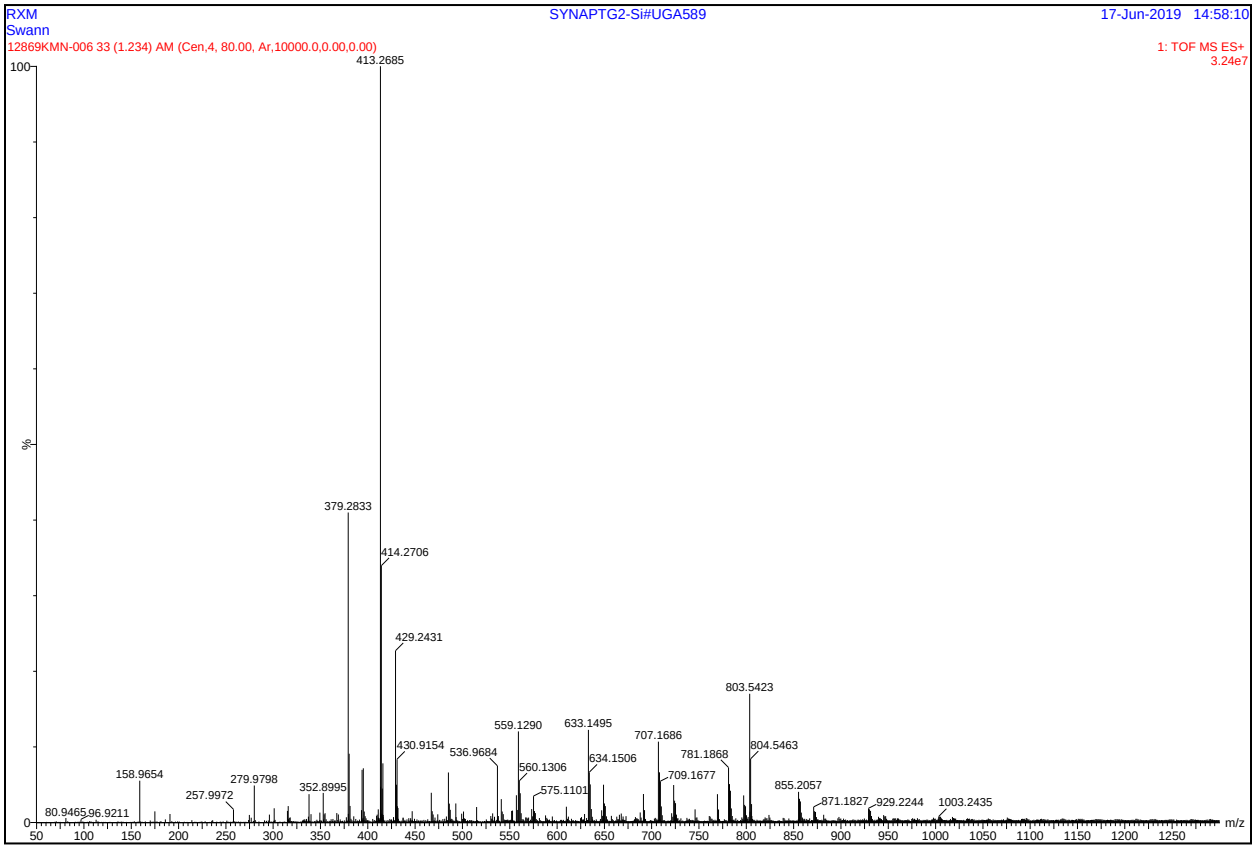

Trial 9:

Crude Product IR

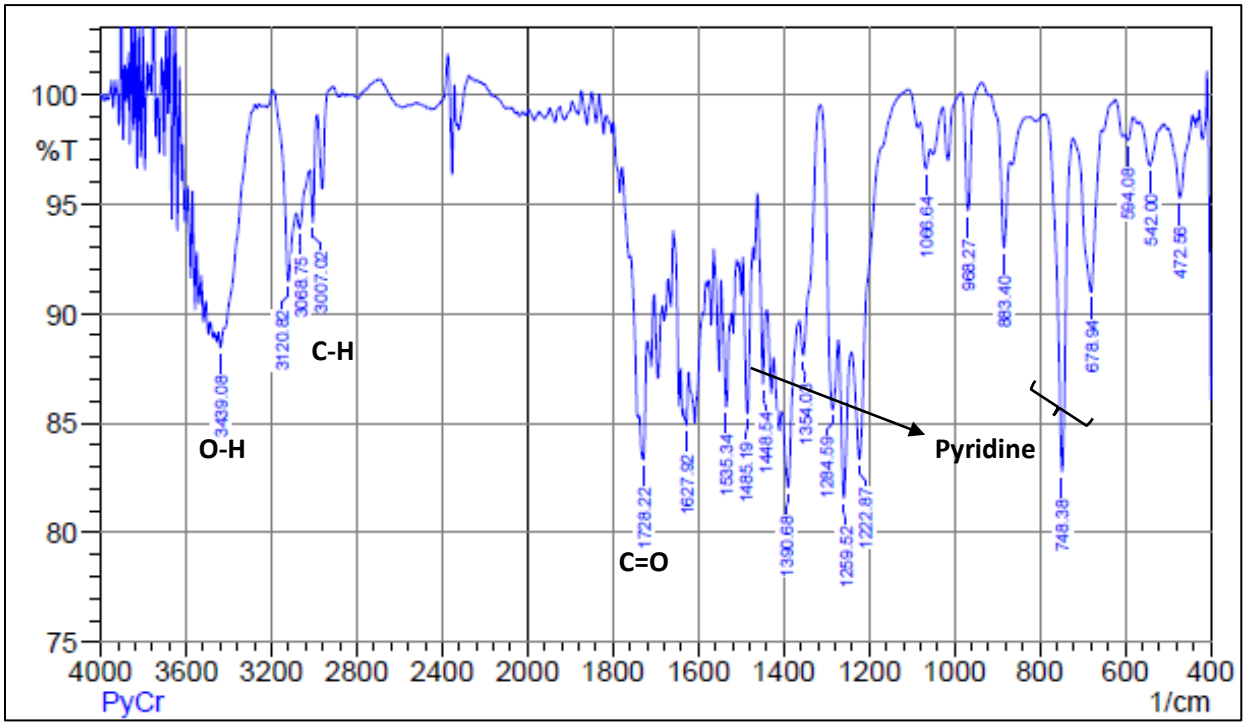

Positive Ion ESI

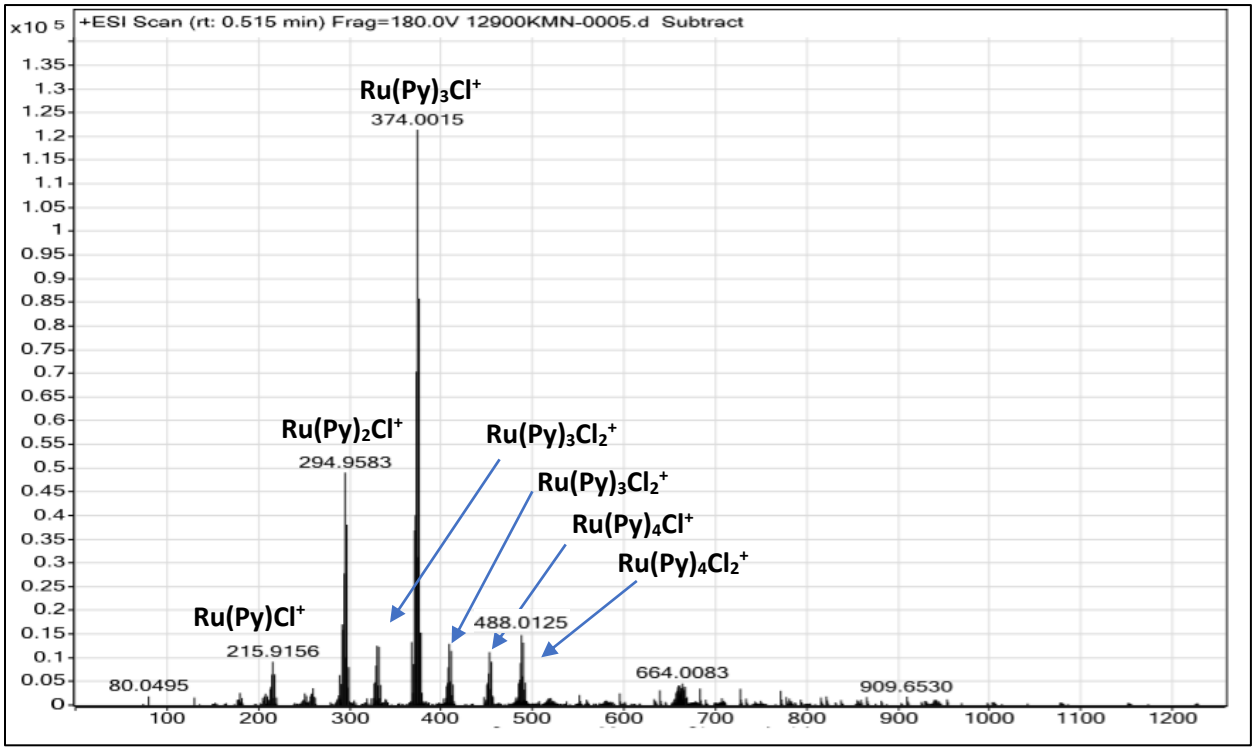

Trial 10:

Crude Product IR

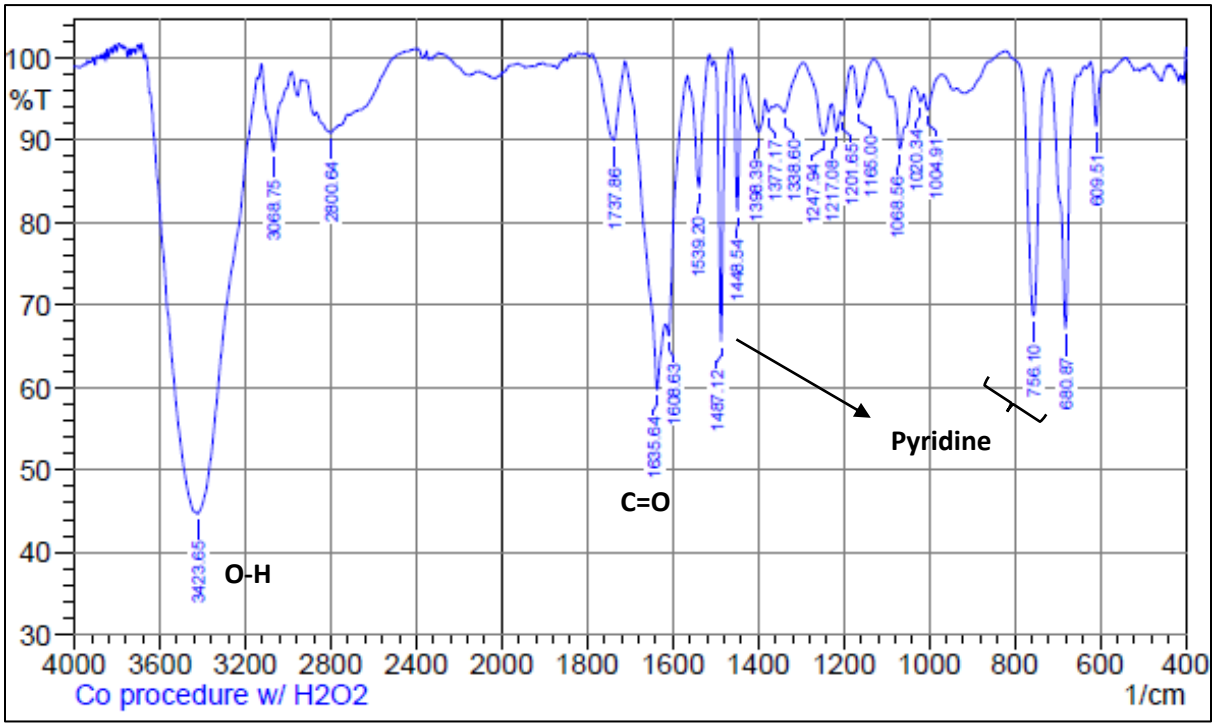

$K_2RuCl_5*H_2O$:

Product Negative Ion ESI

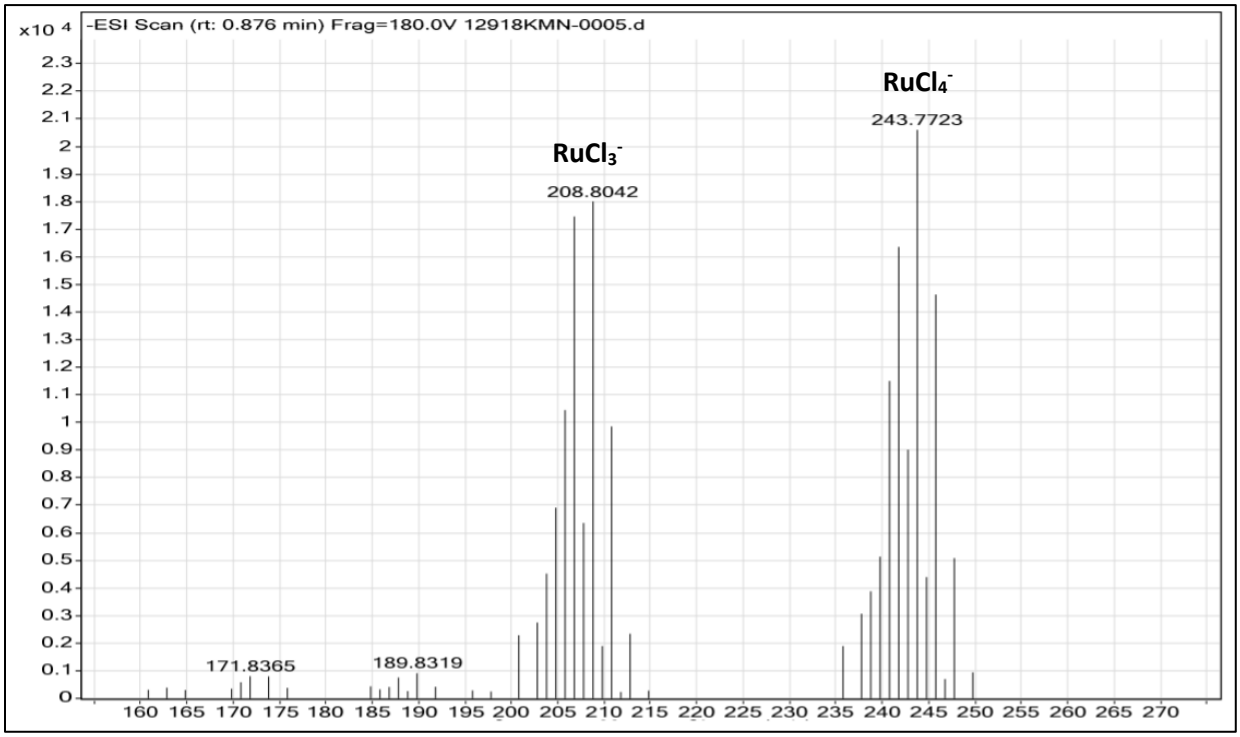

$K_2NTARuCl_5*H_2O$:

Product UV-Vis

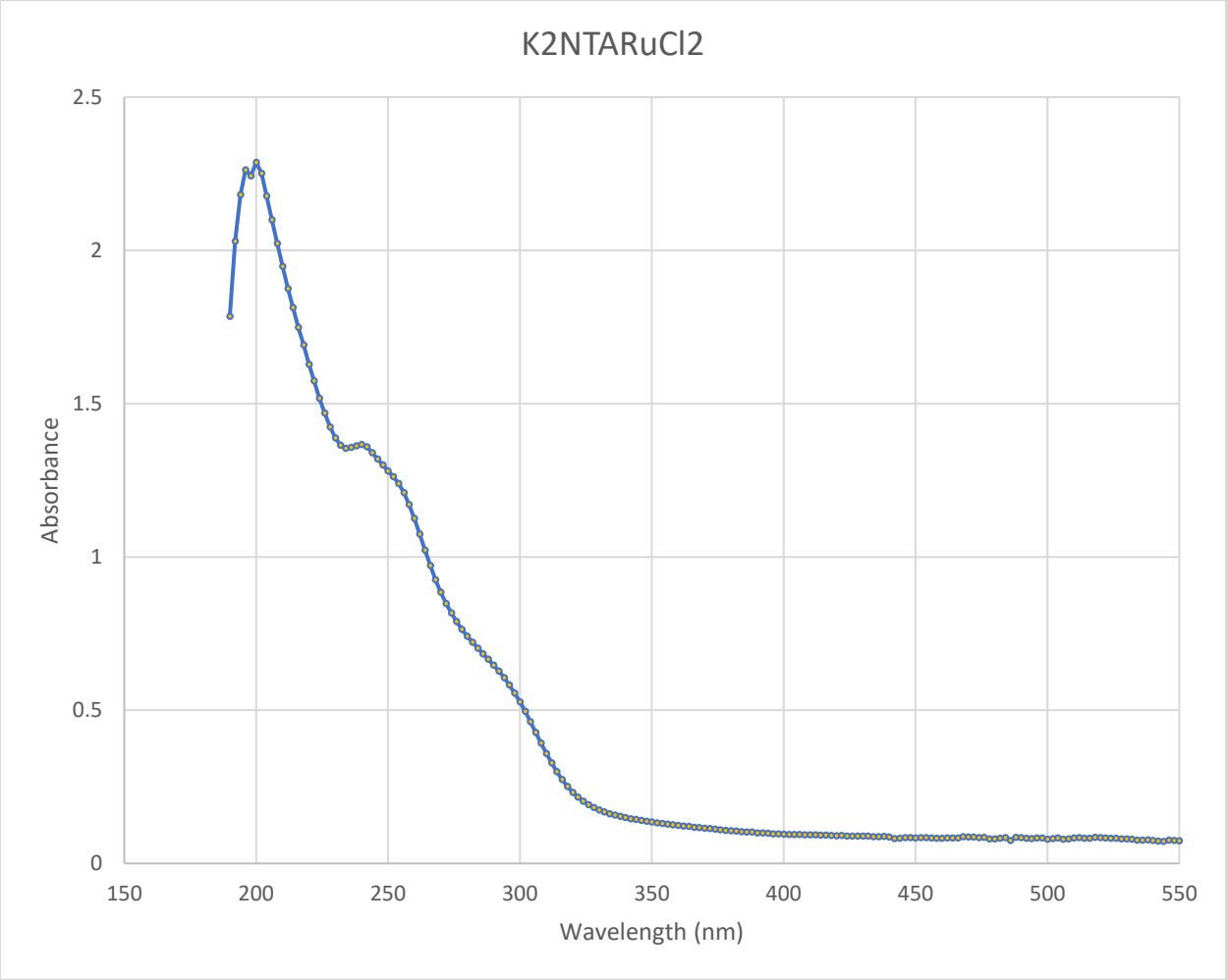

Product IR

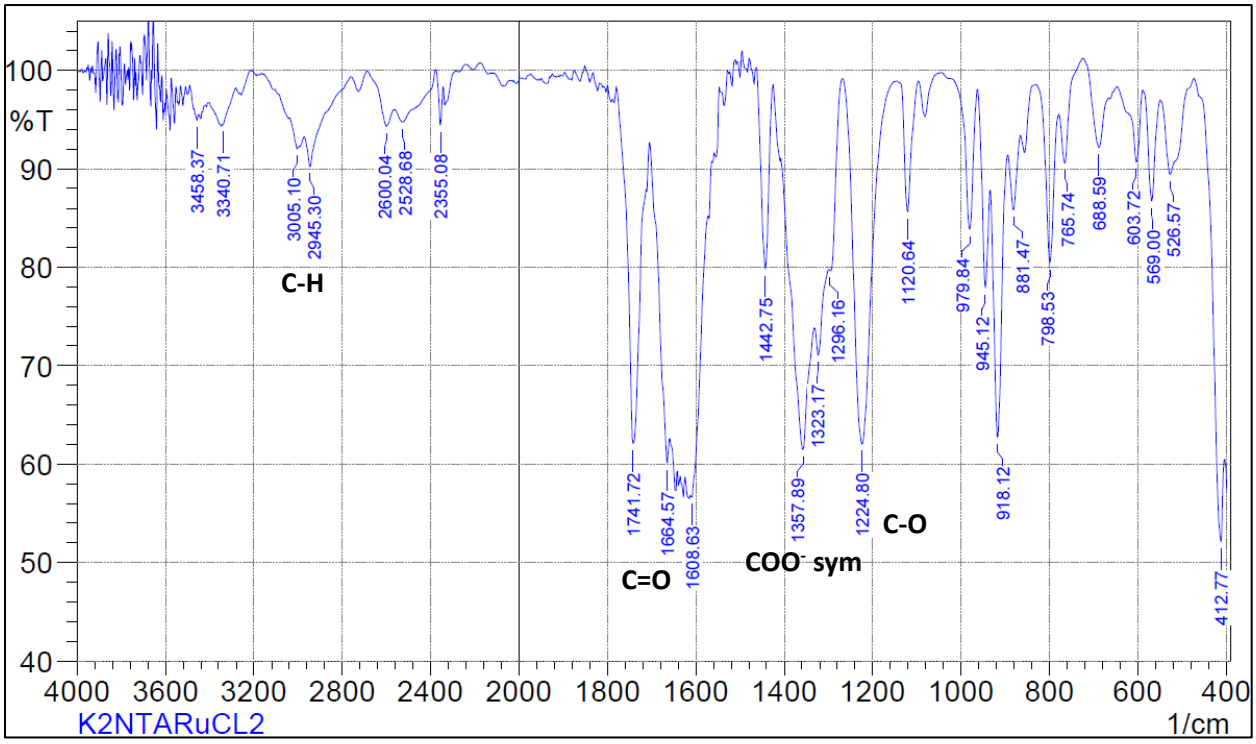
100
%T
90
80
70
60
50
40
4000 3600 3200 2800 2400 2000 1800 1600 1400 1200 1000 800 600 400
1/cm
K2NTARuCL2
3458.37
3340.71
3005.10
2945.30
2600.04
2528.68
2355.08
1741.72
1664.57
1608.63
1442.75
1357.89
1323.17
1296.16
1224.80
1120.64
979.84
945.12
918.12
881.47
798.53
765.74
688.59
603.72
569.00
526.57
412.77
C-H
C=O
COO- sym
C-O

Positive Ion ESI

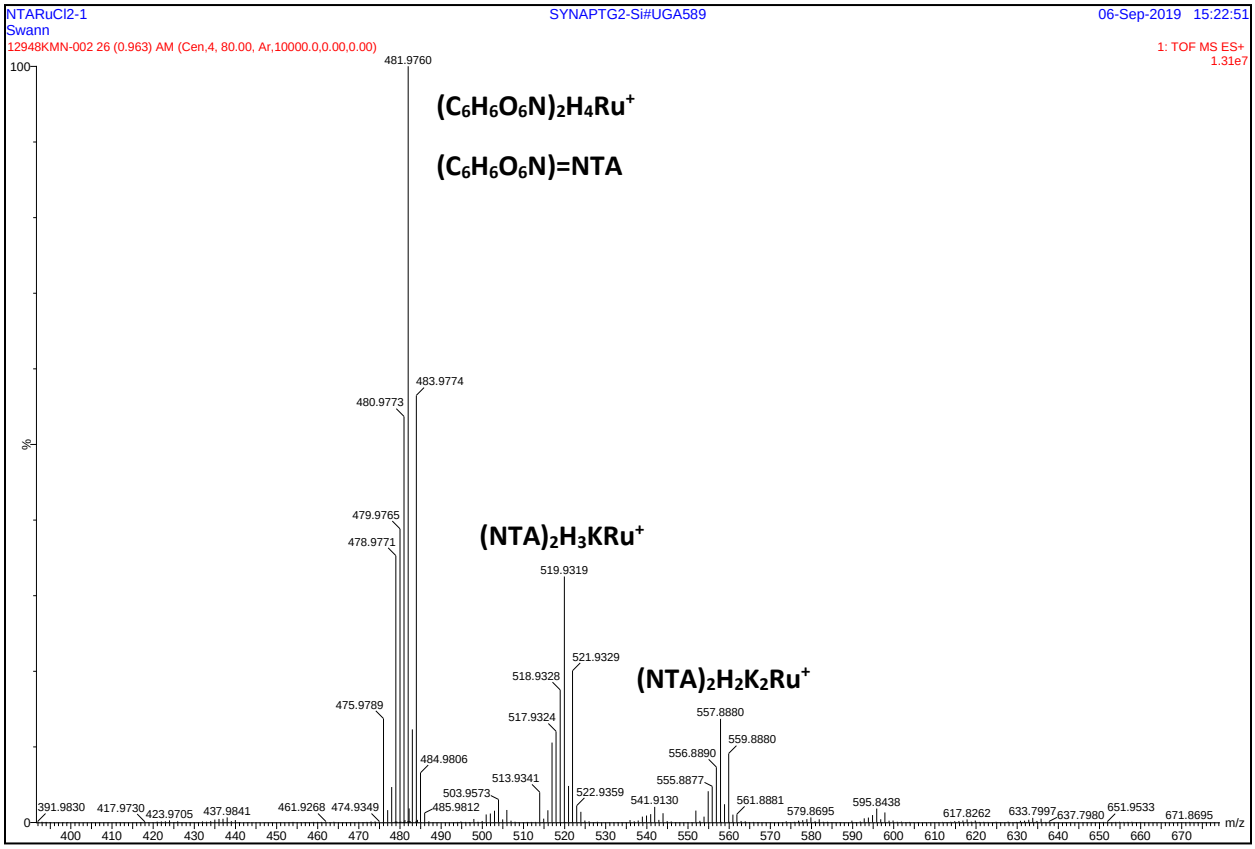

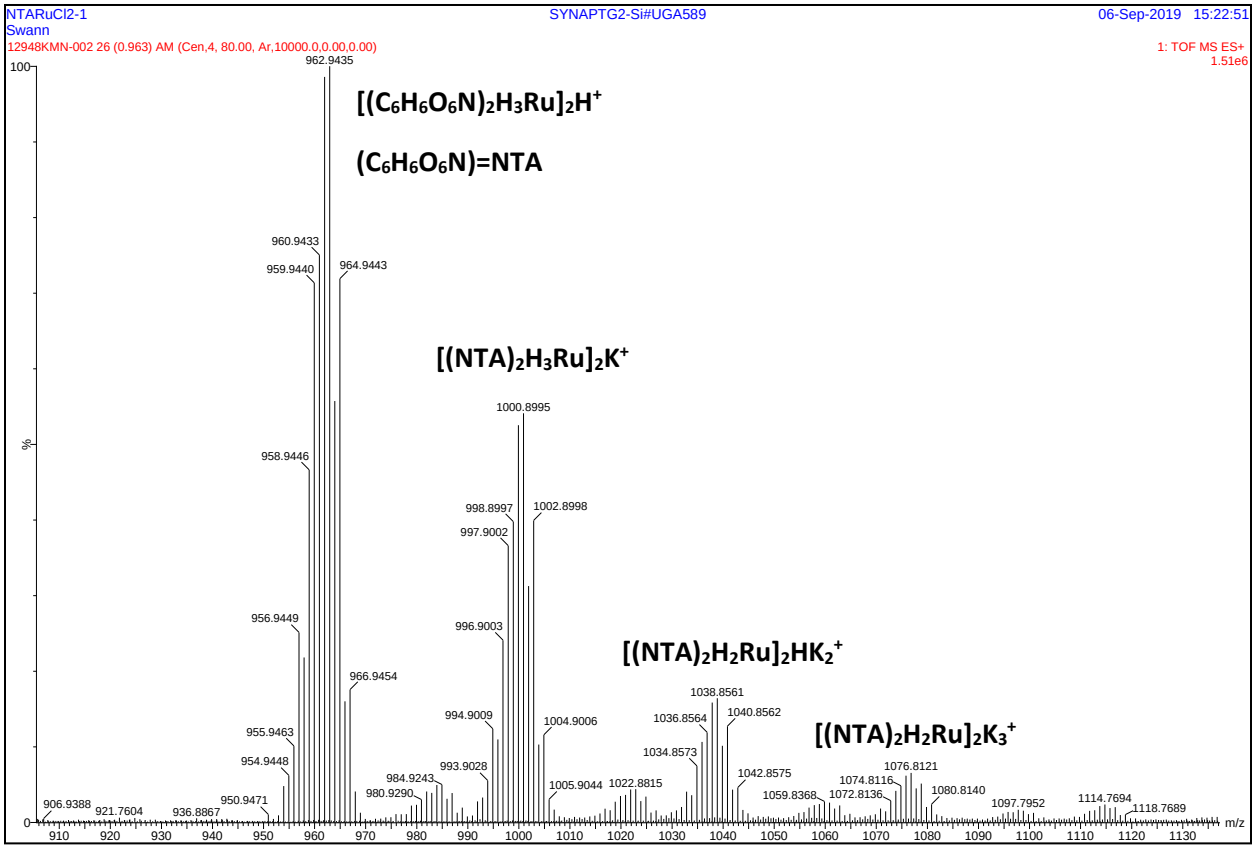
NTARuCl2-1
Swann
SYNAPTG2-Si#UGA589
06-Sep-2019 15:22:51
12948KMN-002 26 (0.963) AM (Cen,4, 80.00, Ar,10000.0,0.00,0.00)
1: TOF MS ES+
1.51e6
[(C6H6O6N)2H3Ru]2H+
(C6H6O6N)=NTA
[(NTA)2H3Ru]2K+
[(NTA)2H2Ru]2HK2+
[(NTA)2H2Ru]2K3+
962.9435
960.9433
959.9440
964.9443
1000.8995
958.9446
998.8997
1002.8998
997.9002
956.9449
996.9003
966.9454
1038.8561
1040.8562
1036.8564
994.9009
1004.9006
955.9463
1034.8573
954.9448
993.9028
1042.8575
1076.8121
1074.8116
984.9243
1005.9044
1022.8815
980.9290
1059.8368
1072.8136
1080.8140
950.9471
1097.7952
1114.7694
906.9388
921.7604
936.8867
1118.7689
%
m/z

Negative Ion ESI